Light Scattering and Evolution of Protoplanetary Disks and Planetary Rings

by

Henry B. Throop

B.A., Grinnell College, 1994

M.S., University of Colorado, 1996

A thesis submitted to the

Faculty of the Graduate School of the

University of Colorado in partial fulfillment

of the requirements for the degree of

Doctor of Philosophy

Department of Astrophysical and Planetary Sciences

2000

This thesis entitled:
Light Scattering and Evolution of
Protoplanetary Disks and Planetary Rings
written by Henry B. Throop
has been approved for the Department of Astrophysical and Planetary Sciences

---

Larry W. Esposito

John Bally

Date _____

The final copy of this thesis has been examined by the signatories, and we find that both the content and the form meet acceptable presentation standards of scholarly work in the above mentioned discipline.

Throop, Henry B. (Ph.D., Astrophysical and Planetary Sciences)

Light Scattering and Evolution of

Protoplanetary Disks and Planetary Rings

Thesis directed by Professor Larry W. Esposito

This thesis examines observations and modeling of young circumstellar disks in the Orion nebula. Three separate arguments suggest that the disks are dominated by large particles, and we are witnessing earliest stages of planetary formation.

I) I used a Monte Carlo nine-parameter 3D disk model to fit Hubble Space Telescope observations in eleven bands from 0.2 – 1.9 μm. The best-fit models are consistent with extinction caused by large particles, $r > \lambda$ in the outer disk edge. II) Interferometric observations at 1.3 mm reveal no measurable flux from the disks, implying that the optical depth is low and thus particles have grown to $r > 1$ mm. III) Numerical models of particle growth within a photoevaporative environment indicate that grain growth happens rapidly and predicts particle sizes similar to those constrained observationally. The model includes a) grain growth in a turbulent disk, b) ice loss by photosputtering, and c) gas and dust loss by entrainment of small particles in a photoevaporative flow. The disks are photoevaporated on timescales of 10^{4-6} yr by O stars in the Trapezium region.

The numerical model indicates that formation of Jovian planets within the Orion region and other OB associations may be difficult; however, formation of terrestrial planets is not affected. I reproduce the observed sharp edge termination in the Orion disks. The existence of Jovian planets within our solar system suggests that our disk is not sharply terminated, and the Edgeworth-Kuiper belt may extend significantly beyond that presently detected.

I apply a similar numerical model to evolution of Saturn's G ring, based on spec-

troscopic observations at the 1995-96 ring plane crossing, coupled with a light scattering model for realistic, processed small particles. Best-fit solutions indicate that the ring was formed by catastrophic disruption of a satellite $10^7 - 10^8$ years ago and is sustained in steady-state by an unseen population of km-sized parent bodies.

Acknowledgements

There are many people who are responsible for making my time in Boulder rewarding. I'd like to give thanks:

To Larry Esposito, who has supported me for the last five years at the University of Colorado. He has given me an incredible amount of discipline and has never shied from giving my research the well-needed skeptical, critical eye. It is to his credit that he had faith in me through my initial fumblings, and then continued his support even as I strayed far from my initial research field. Larry's physical insight and ability to unwrap and solve meaningful problems in an organized way is continually inspiring and he has made more difference on my thought process than anyone else.

To the spectacular John Bally, who I managed to corner several times in my first years here, and who I have been fortunate to work with for much of the time since then. His energy and enthusiasm is contagious, and the excitement I've had over the past several years is largely due to him. Lunches with John are those incredible experiences where everyone ends up convinced there's not a problem in astronomy that can't be solved with a few pieces of glass and a good set of filters.

To members of the Colorado Rings Group, for frequent discussions from which this work has greatly benefited;

To the other numerous members of the outstanding faculty and research community in Boulder who have taken an interest in my work, and to several faculty members here – Fran Bagenal, Nick Schneider, and Katy Garmany in particular – for making a

difference in my time here;

To my various professors & teachers – Kathy Eastwood at Northern Arizona University, Bob Cadmus at Grinnell College, and Pat Canan and Barb Gladstone at Corvallis High School: any physical intuition in this dissertation is due to Pat; any readability due to Barb; and the fact that I have entered the field of astronomy at all, to Kathy & Bob;

To my present and former officemates: Mary Urquhart, Brad Dalton, Amanda Sickafoose, Shawn Brooks, Lisa Braun, and especially Robin Canup and Mark Bullock – the former for guiding me through my first years and teaching me most of what I know about numerical modeling, and the latter for teaching me everything else;

To my *de facto* officemates for the past few months, without which we would have no source of mutual entertainment and ridicule during this thesis-writing experience: Stefanie Lawson, Ka Chun Yu, and Niescja Turner;

To my friends in Boulder for making my 'other' life always interesting and filled with good people and good food;

To Niescja Turner, who – from our very first days in Colorado – has been a much-needed and ever-present friend, and with whom my graduate experience has been immeasurably more exciting and rewarding – okagasama de;

And of course to my family and in particular my parents, who've generally been pretty happy with whatever I've chosen to do at the moment.

Contents

Chapter

Tables

Table

Figures

Figure

Chapter 1

Introduction

Space between rings –
Smoke, Saturn's, 18 carat, a telephone's
Christine Lavin, Future Fossils

In this dissertation, I focus on two contrasting but complementary systems: young, photoevaporating circumstellar disks, and old, steady-state dusty planetary rings. Although significant differences exist between the two systems, broadly similar methods can be used to model the structure and evolution of each.

The largest portion of this dissertation involves observations and evolutionary modeling of young circumstellar disks. I present three lines of evidence that some disks observed in the Orion nebula are already undergoing the earliest stages of planetary formation. Furthermore, it appears that the majority of stars form in externally-irradiated regions like Orion, so the model results presented here may have significant implications for planetary formation probabilities throughout the galaxy.

1.1 Disks in the Universe

From the rotation of planets around the sun, to the slow motion of stars around a galaxy, disks are common in the universe over wide ranges of scale. Table 1.1 lists several basic, dimensionless quantities associated with a range of disk phenomena in an astronomical context. In each case, a central gravitational force drives the motions of small bodies orbiting around a large central mass. From the table, the dominant regimes and physical processes can be identified.

All the disks share some similarities, although it is obvious that some are more closely related than others. For instance, the galactic disk is dynamically similar to most of the other systems only superficially: stars contribute such a negligible volume to a galaxy and the orbital timescale is so long that during an entire galactic lifetime, perhaps only one or two stars will directly collide. Rather, collective gravitational effects dominate dynamics in the massive galactic disks.

Meanwhile, rings around solar system planets and debris disks around older stars share many properties: being dynamically evolved and collisionally active, particles in these disks frequently collide, but the products of collisions are balanced by other processes such that a steady state is maintained over a large number of orbits. The remaining systems – the Edgeworth-Kuiper Belt (EKB), the main-belt asteroids, and protoplanetary disks around young stars – represent an amalgam of properties of the other systems.

The various light sources, although they do not change the dynamics of each disk, constrain the way each can be observed, and thus the properties that can be determined about each system.

In this dissertation, I create models for the evolution of protoplanetary disks and planetary rings, based on my analysis of recent observations over a wide range of wavelengths and techniques. The models created for each system differ significantly, as might be expected from the table. The connection, however, is broadly similar in spirit and approach.

1.2 Protoplanetary disks

Early proposals that the Earth was but one of many planetary systems surrounding nearby stars were met with skepticism, outrage, and sometimes capital punishment (*e.g.*, the scientific martyrdom of Giordano Bruno in 1600 AD.) Although there remains no direct evidence for nearby Earth-like planets, peer reviewers in the scientific world

Table 1.1: Disk scaling regimes

Galaxy[1]	Proto-planetary disk	Debris disk	Rings,[2] dust	Rings,[3] parent bodies	EKB	Main-belt asteroids	
10^{-13}	10^{+2}	10^{-3}	10^{-6}	10^{-8}	10^{-8}	10^{-11}	Optical depth
10^{+1}	10^{+1}	10^{+7}	10^{+11}	10^{+10}	10^{+7}	10^{+9}	Total orbits
10^{-12}	10^{+4}	10^{+4}	10^{+5}	10^{+2}	10^{+3}	10^{+2}	Tot. colls/particle
10^{+2}	10^{-10}	10^{-12}	10^{-10}	10^{0}	10^{-1}	10^{-1}	$V_{\rm esc}/V_{\rm coll}$
10^{0}	10^{-1}	10^{-8}	10^{-23}	10^{-16}	10^{-6}	10^{-9}	$\rm M_{disk}$ / $\rm M_{cent}$
	√						Optically thick
√	√						Dynamically young
	√	√	√	√	√	√	Collisionally active
√				√	√	√	Grav. interactions
√	√						Massive disk
Intrinsic	External diffuse; Central	Central	External	External	Central	Central	Light source

[1] Considering stellar component only
[2] Small-particle component of typical dusty ring
[3] Large-particle component of typical dusty ring
Numbers indicate present-day values

have become somewhat more open to discussions of the idea.

It is now generally accepted that our planets were created from flotsam out of the gas and dust that collapsed to form the Sun. Disks in various states of collapse have recently been discovered surrounding many nearby young solar-type stars, suggesting that these disks are protoplanetary in nature. There is no observational evidence for any planetary formation in these disks. However, given recent discoveries of giant planets surrounding nearby stars, it is not unreasonable to assume that the protoplanetary disks may in fact eventually form planetary systems.

The first compelling evidence for disks around young stars was based on detections of solid H_2O absorption and CO emission near HL Tau in the Taurus dark cloud (Cohen 1983, 1975). Subsequent analysis by Beckwith *et al.* (1990) firmly established several more stars or systems as having disks based on their IR and mm molecular and **thermal emission** (Figure 1.2). Higher resolution imaging, however, has failed to further uncover HL Tau system from behind its deep enshrouding clouds; an HST non-detection of the central star by Stapelfeldt *et al.* (1995) placed a line-of-sight limit $A_V > 22$ for that disk, and nearby nebulosity suggested that it was surrounded on all sides by thick clouds of gas and dust. The neighboring GG Tau disk system, however, has been directly imaged using the **reflected light** (Figure 1.1) of its central star, which effectively probes morphology in the inner regions of the disk. In the outer regions, particles are more difficult to detect because of both the lower flux, and the lower particle number density. In reflected light cases like this, the typical flux level drops as $R^{-3.5} - R^{-4}$ (*e.g.* Kalas & Jewitt 1995; Grady *et al.* 2000), and properties of the outer edges are often unconstrained, if the edge is even detectable above the background. With a central source the scattering phase angle (source – particle – observer) is well-known, and some particle attributes can be determined based on their scattering properties. For most of the known Taurus disks, even this level of analysis is difficult, because they have been detected only from their molecular or thermal emission signatures.

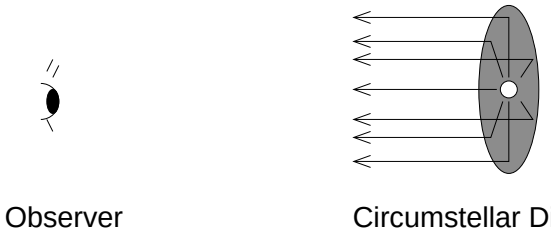

Figure 1.1: Circumstellar disk seen with reflected star light. Brightness at the outer edge drops rapidly, but phase functions can be determined uniquely across the disk. Debris disks like β Pictoris and some young Taurus disks are usually seen with reflected light. Not to scale.

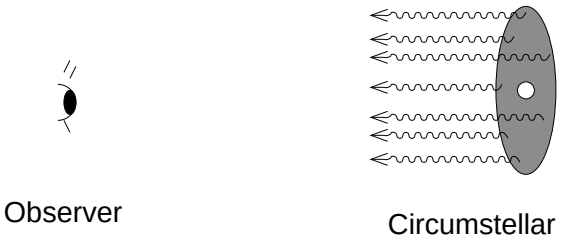

Figure 1.2: Disk, thermal emission. Heat from gravitational collapse or the central star is re-radiated as continuum or line emission from dust or gas. The Taurus disks were originally discovered from their thermal emission.

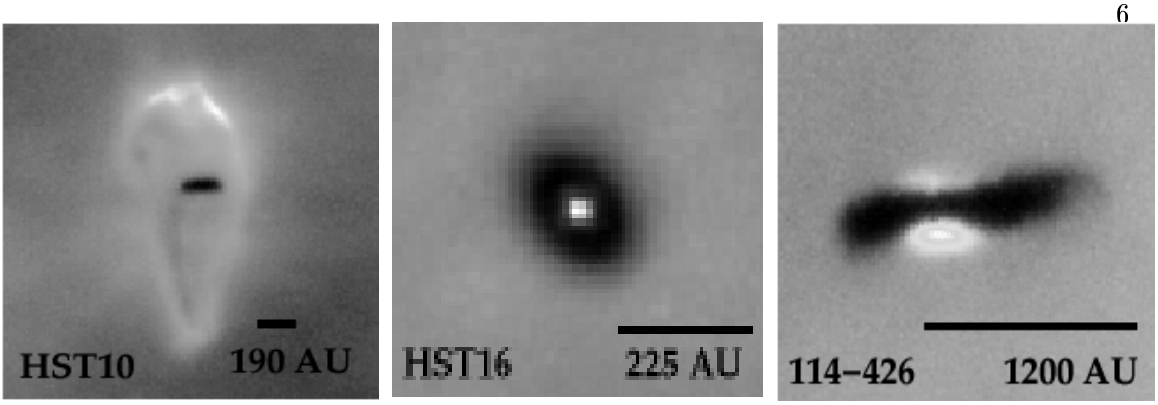

Figure 1.3: Three representative disks in Orion, seen in transmitted light. HST10 is seen surrounded by a photoevaporative envelope and ionization front; HST16 is face-on with its central star visible; and the star of 114-426 ('SW Disk') is seen indirectly through reflection.

Using HST, O'Dell *et al.* (1993) discovered an entirely new set of young circumstellar disks in the Orion nebula. These disks had been previously suggested by Churchwell *et al.* (1987) based on detection of compact ionized sources in Orion, but the O'Dell *et al.* observations definitively and graphically showed disks surrounding young stars (Figure 1.3). In contrast with those in Taurus, the Orion disks were seen in **transmitted light** (Figure 1.4). The Orion nebula's HII region serves as a broad backlight which can be used to probe their internal structures, silhouette-style. Because the light source is spatially uniform – unlike the R^{-2} flux in the Taurus cases – the furthest, faintest edges are still visible, and lit just as brightly as the inner regions. Although the central stars are visible in many cases, their light is mostly negligible compared with that from the HII region – in particular because the further distance of Orion makes high resolution imaging challenging. Because the nebula is diffuse, no information about the particle phase functions can be determined from the observations. To date, a total of 47 dark disks have been discovered in Orion with an ongoing set of HST surveys. This set forms the largest set of *any* family of disk yet discovered.

The Orion backlighting is a result of flux from the Orion nebula's most prominent feature: the so-called Trapezium cluster of five bright O stars within the nebula's central

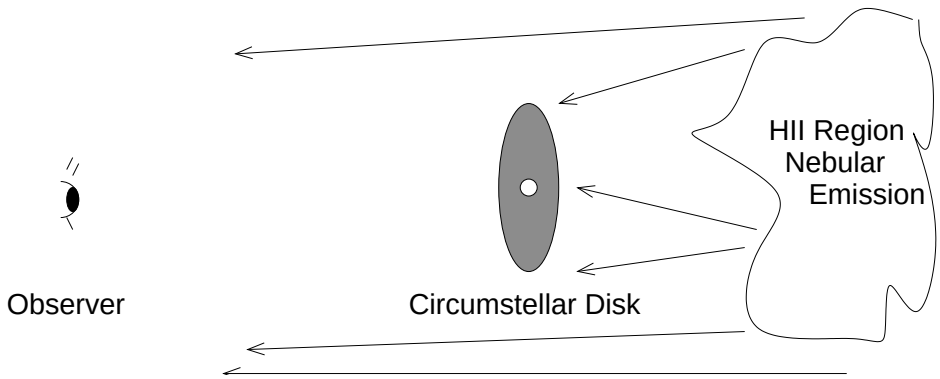

Figure 1.4: Circumstellar disk seen in transmitted light. Illumination from the background HII region is nearly uniform across the disk, allowing the faint edges to be seen. Light from the central star is negligible, and the phase functions are washed out.

0.01 pc (2000 AU) core. The O stars – dominated by $10^5 L_\odot$ O6p star θ^1 Ori C – ionize H_2 and produce the HII region which makes the nebula visible.

But in addition to illuminating the region for the benefit of observers, the Trapezium has a second, more destructive effect on the Orion disks. UV radiation from θ^1 Ori C has been shown to rapidly 'photoevaporate' and remove gas and dust from the disks on 10^5 yr timescales (Johnstone *et al.* 1998). The evidence for this process occurring is clear; the majority of the disks discovered are surrounded by some sort of ionized region associated with photoevaporation (*e.g.*, Figure 1.3a), and presumably many more disks have already been completely destroyed. Although some disks may be far enough away from θ^1 Ori C to temporarily avoid photoevaporation, evolution of the majority of disks is strongly affected.

Total mass of the Orion nebula is $\sim 10^5 M_\odot$ and its luminosity is $\sim 10^5 L_\odot$, making it a medium-sized subgroup within the 12 Myr old Orion OB association, making it the largest HII region in the local neighborhood. Throughout its 10^7 yr lifetime, Orion has probably produced $\sim 20,000$ low-mass and several dozen high-mass stars. Cooler, calmer star formation environments like Taurus are more numerous but smaller ($10^4 M_\odot$). Where do most stars form? This is an important question that must be answered when looking at how applicable different disk models are to 'typical' systems.

Elmegreen (1985, and references therein) fits the mass of molecular cloud star formation regions in the local neighborhood as power law,

$$n(M_c) \sim M_c^{-1.5 \pm 0.1} \ . \tag{1.1}$$

Integrating, and assuming the present-day local neighborhood is representative, one finds that roughly *ten times as many stars form in Orion-mass regions as Taurus-mass clouds.* Therefore, although they are frequent, close, and easy to study, most stars simply do not form in low-mass clouds. To understand the environments in which most

low-mass stars – and presumably most protoplanetary disks – form, we must look at regions like Orion, where photoevaporation competes with planetary formation to either create or destroy young planets.

Dozens of models of the evolution from a collapsed disk to a planetary system have been published in the literature. The usual processes include grains colliding, sticking and growing, leading to eventual gravitational interaction between larger bodies, and finally gravitational sweep-up and capture of nebular gas. However, *none* of these models have considered the evolution of disks in externally-illuminated, photoevaporating environments – that is, 100% of the models apply exclusively to 10% of the real-world examples of young disks! It is a major goal of this dissertation to rectify this situation, in particular by using the observations of the Orion disks as a constraint to evolutionary models.

1.3 Planetary Rings

Since 1979, the number of known ring systems in the solar system has grown from one, to between 4 (detected) and 6 (predicted). The most well-characterized system remains that around Saturn, whose rings have been observed by several spacecraft and extensively from the Earth. Saturn's densest, optically thick A and B rings contain gravitational wakes and some spiral and 'braid' structures; the more tenuous D, E, and G rings appear faint and featureless. In contrast to the protoplanetary disks, the rings are dynamically evolved and generally observed to be in steady-state – that is, the bulk properties do not change appreciably on an orbital timescale. The rings are maintained in steady state by balanced interactions between a small number of simple processes.

Observations (Figure 1.5) of the Saturnian ring system from spacecraft and the Earth have included imaging, spectroscopy, stellar occultations, polarimetry, photometry, and *in situ* measurements of dust particles and magnetic and plasma field properties. From these surveys, a broad picture of the rings in their current state can be assembled.

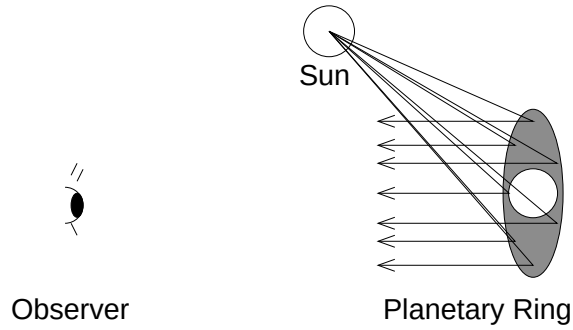

Figure 1.5: Light scattering with reflected solar radiation, planetary rings. Because the positions are known, the scattering phase angles are well-defined and thus some particle properties can be determined from the ring's phase curve.

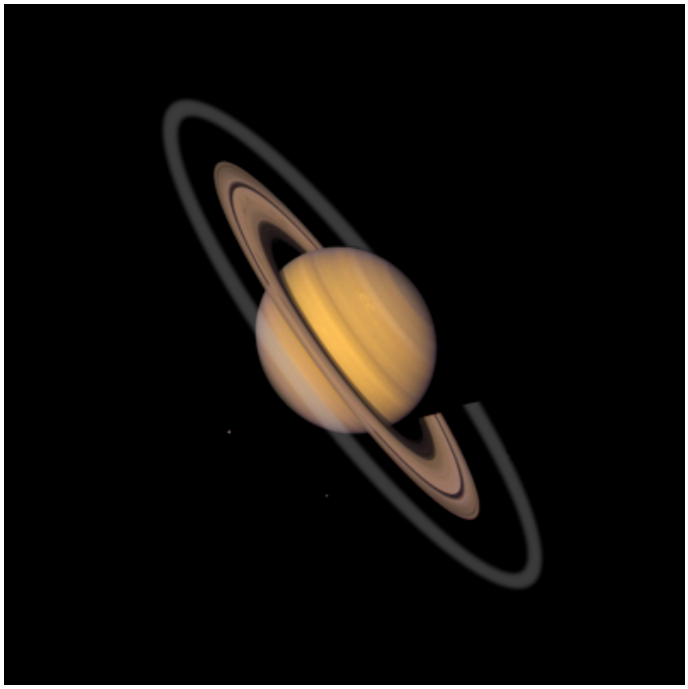

Figure 1.6: Saturn's ring system, as imaged by Voyager in reflected light. The faint G ring has been added for clarity.

More powerfully, evolutionary models can then be used to describe the rings in their past and future states.

1.4 Fundamental Questions

In this dissertation, I create models for the evolution of protoplanetary disks and planetary rings, based on my analysis of recent observations over a wide range of wavelengths and techniques. Although specifics of the models differ, the approach and spirit are similar. Fundamental questions to be answered include the following:

- What physical properties can be directly observed from the data?
- What physical properties – which cannot be measured – can be inferred from a physical model based on the data?
- What are the fundamental processes that govern interactions between the system and its environment?
- What initial conditions create a system like that we see today?
- How common are these systems?
- What will the future of these systems look like?

More specifically:

- What is the nature of particles in Orion's young circumstellar disks?
- Under what circumstances can planets form in these disks?
- What are particle properties in Saturn's faint rings?
- How did this rings form and what is their eventual fate?

1.5 Structure of Thesis

In Chapter 2, I discuss observations that have been made of dark disks in the Orion nebula, including HST imaging from UV to near-IR, and 1.3 mm interferometric thermal and line observations. I develop a 3D disk model that is used to determine fundamental parameters of the disks such as their dimensions, mass, and grain sizes.

The work presented in Chapter 3 uses a numerical evolutionary model of the Orion disks to predict their past and future states based on models of disk photoevaporation and grain growth. The same model places some constraints on our own solar system's formation and evolution.

Chapter 4 applies a similar light scattering a disk evolution model to Saturn's G ring. The light scattering model is more complex and the observations better constrained than most of the Orion observations, and I place comparably tight limits on the present particle population of the ring. In the evolutionary model, loss and production processes are balanced; unlike the Orion disks, the G ring is nearly steady-state.

Finally, in Chapter 5, I summarize the results, compare the constraints placed from observation and modeling, describe several key observations that would build on this research. I conclude with a number of predictions, many of which could be evaluated observationally.

Chapter 2

Observations of Protoplanetary Disks

I can hear the sizzle of newborn stars, and know anything of meaning,
of the fierce magic emerging here. I am witness to flexible eternity,
the evolving past, and I know we will live forever,
as dust or breath in the face of stars,
in the shifting pattern of winds.

Joy Harjo, Secrets from the Center of the World

2.1 Introduction

Humanity has been observing the solar system for millenia, but it has been only in the last 250 years that our view of the solar system has expanded beyond the sun and the central planets. Planets such as Uranus, Neptune and Pluto have been added to the solar system's inventory, as have countless icy bodies beyond 40 AU. Detecting these latter objects has been the struggle for identifying tiny, moving patches of photons awash in a sea of background stars. Beyond this distance very little is known. Although circumstantial evidence has suggested that the the space between Pluto and our closest neighbor star is filled with trillions of small bodies, we have yet to detect more than a teaspoonful of the closest ones. No spacecraft have ever imaged bodies at this distance or detected even as much as a single speck of dust in the environment.

Several tens of thousands of times further away, new planets have been detected surrounding other stars – the first direct proof for the existence of other planetary systems beyond our own.[1] Although not directly imaged, detection of these planets has proved to be both a major technical breakthrough and a philosophical paradigm

[1] Several reports of substantially closer systems have been published, but not confirmed by follow-up observations (Zweibel 1998; Showstack 1999).

shift. Our knowledge of these systems is limited, but the number of major planets discovered outside our own solar system now greatly exceeds the number within.

At the immense distance to local star-forming regions – several million times further than Pluto – detection of solar systems like our own would seem unlikely, given the difficulty of understanding even the basic parameters of our own system. But ironically enough, possible solar systems in formation have been detected and directly imaged floating amongst the clouds of the Orion nebula. Unlike our own system, the size and basic parameters at the very outer edges can be directly observed, as can the properties of the smallest dust particles in these systems. Furthermore, our view is not limited to a single example like our own system: in fact, there are literally dozens of these 'protoplanetary disks' scattered throughout the tiny portion of Orion that has been searched to date. Just like the individuality of dust grains themselves, each disk is different: in size, shape, location, age, and environment. By studying the suite of disks presented by Orion, we can learn about the diversity of planetary systems and their formation environments. In fact, we do not yet even know if planets really *do* form in Orion – the word 'protoplanetary' should be used with care, and perhaps a more linguistically accurate would be proto-potentio-planetary disks. The Orion disks are all younger than our own isolated world. Will they turn out to be different than ours – or similar? We don't know. But a good way to start is by looking.

2.2 Visible-wavelength Optical Observations

At the distance of Orion ($d = 450$ pc, Warren & Hesser 1977), imaging with high spatial resolution is substantially more difficult than of closer systems such as Taurus ($d = 170$ pc). As a result, the Hubble Space Telescope (HST) has been the primary platform for Orion disk observations, and it was with Hubble's original Wide Field / Planetary Camera (WF/PC) that the disks were originally discovered by O'Dell *et al.* (1993). Eighteen compact sources – dubbed HST1-HST18 – were discovered in their

Table 2.1: Dark disk observations (subset)

Filter	Central Wavelength	Band	Scale†	Exposure Time	HST10 182-413	HST16 183-405	SW Disk 114-426
			FOC / GO 5085,5469 (O'Dell & Wong 1996; Bally *et al.* 1998a)				
F190M	190 nm	cont	0.014"	55.75 s		√ UU	
F231M	233 nm	cont	0.014"	55.75 s		√ U	
F253M	255 nm	cont	0.014"	60 s		√ UU	
			WFPC2 / GO 5469 (Bally *et al.* 1998a)				
F502N	502 nm	OIII	0.045"	180 s	√	√	
F547M	547 nm	cont	0.045"	30 s	√	√	
F631N	631 nm	OI	0.045"	180 s	√ E	√	
F656N	656 nm	Hα	0.045"	60 s	√	√	
F658N	658 nm	NII	0.045"	180 s	√	√	
F673N	673 nm	SII	0.045"	180 s			√
F502N	502 nm	OIII	0.1"	100 s			√
F547M	547 nm	cont	0.1"	30 s			√
F631N	631 nm	OI	0.1"	100 s			√
F656N	656 nm	Hα	0.1"	60 s			√
F658N	658 nm	NII	0.1"	180 s			√
F673N	673 nm	SII	0.1"	100 s			√
			WFPC2 / GO 6603 (Bally *et al.* 2000)				
F547M	547 nm	cont	0.045"	120 s	√ D	√ D	
F606W	606 nm	cont	0.023"/0.05"	600 s			√ P
F631N	631 nm	OI	0.023"	1600 s	√ E	√	
F656N	656 nm	Hα	0.023"	1600 s	√	√	√
F814W	814 nm	cont	0.023"	1600 s			√
			NICMOS / ERO (Chen *et al.* 1998)				
F187N	1.87 μm	Paα	0.038"	384 s	√		
F212N	2.12 μm	H_2	0.038"	576 s	√		
F215N	2.15 μm	cont	0.038"	576 s	√		
			NICMOS / GO 7367 (McCaughrean *et al.* 1998)				
F110W	1.1 μm	cont	0.042"	384 s			√ S,U
F160W	1.6 μm	cont	0.042"	384 s			√ S,U
F187N	1.87 μm	Paα	0.042"	288 s			√ U
			OVRO (Bally *et al.* 1998b)				
	1.3 mm	^{13}CO(2 − 1)	1.8"	h	√ N	√ N	√ N
	1.3 mm	C^{18}O(2 − 1)	1.8"	h	√ N	√ N	√ N
	1.3 mm	cont	1.8"	h	√ N	√ N	√ N
			IRAM (Lada 1998)				
	1.3 mm	cont	1"	h	√ N	√ N	
	1.3 mm	cont	1"	h	√ N	√ N	

† 0.014" = 6.3 AU; 0.023" = 10 AU; 0.042" = 19 AU; 0.045" = 20 AU; 0.1" = 45 AU; 1" = 450 AU; 1.8" = 810 AU

U Slightly underexposed
UU Severely underexposed; not used
P Using 4-position linear polarizer; not used
E Disk seen in emission; not used
D Duplicate observation; not used
S Excessive stellar contamination; not used
N Non-detection (*i.e.*, lower limit)

survey, including five silhouette disks. Seven visible-wavelength filters (Table 2.1) were used at a resolution of 0.1" across the 2.6' field of view. The narrow filters ('N', $\Delta\lambda \sim 20$ Å) saw the disks in silhouette from various lines of emission in the HII region, while the wide filters ('W,' $\Delta\lambda \sim 500$ Å) primarily observed continuum emission and reflected or direct starlight. Most of the disks were seen in silhouette against the bright HII background; however, the HST10 disk was seen to emit at OI (Bally *et al.* 1998a), apparently formed as a product of OH dissociation (Stoerzer & Hollenbach 1998b). All the visible HST observations were taken at a gain of 7 e^1/DN (data number), with readnoise $\sim$ 5 DN.

These initial searches were based on earlier hints of condensed objects found in the nebula by VLA observations of Churchwell *et al.* (1987). This prescient interpreted three dozen of the most compact thermal radio sources as photo-evaporating circumstellar – and possibly protoplanetary – disks.

Followup HST observations by the combined programs of McCaughrean & O'Dell (1996) and Bally *et al.* (1998a) used the newly-installed WFPC2 instrument to survey a far wider region of the nebula ($\approx 8' \times 10'$), much of this at the high resolution of the PC (0.045"). This program detected a total of seven dark disks – and hints of several dozen more – among the 145 compact sources imaged. Filters were similar to those used in the initial survey. Bally *et al.* (1998a) also imaged several regions with the Faint Object Camera (FOC) in the UV; these observations were somewhat underexposed, but did unambiguously detect several silhouette disks.

To extend the wavelength range, McCaughrean *et al.* (1998) used the Near Infrared Camera and Multi-Object Spectrometer (NICMOS) to study the largest of the known Orion disks, 114-426. Images were taken through a variety of wide near-IR filters and polarizers; unfortunately, short exposures caused most of these images to be underexposed, and in the wide filters diffracted star light contaminated much of the disk. New NICMOS observations of this disk must wait until the instrument is brought back

from thermal hibernation.

Bally *et al.* (1999) used the PC in dithering mode to effectively double the spatial resolution to 0.023", slightly oversampling HST's point spread function (PSF) in the visible. Their program imaged the major known dark disks through four bright filters, and the 114-426 disk through the four-position polarizer F606WPOL.

Hayward & McCaughrean (1997, also unpublished) used the SpectroCam-10 mid-IR imager at 8.8-17.9 μm to image several of the disks from the 5 m Hale telescope on Mt. Palomar. These disks have yet to be analyzed in detail. Because of the spatial resolution and PSF stability required, little additional imaging of the Orion disks has been done from the ground. New and upcoming systems – especially in the near-IR, such as SOFIA and Keck/AO – may be expected to contribute significantly to future understanding of the disks.

Several non-detections of the disks in millimeter wavelengths will be discussed in Section 2.6.

2.3 Previous Analysis

Only limited analysis of the Orion dark disks images has been done. The region is incredibly rich with outflows, Herbig-Haro objects, bow shocks, young stars, and general mayhem – and the lack of analysis of any one feature may have much to do with the sheer quantity of already fascinating data to analyze. A study by McCaughrean & O'Dell (1996) remains the most recent serious analysis of the dark disk observations. Since this work was published, new observations have extended the wavelength range and spatial resolution.

McCaughrean & O'Dell (1996) (hereafter MO96) examined six of the disks in the images, taken with the [OIII] and Hα filters. Throughout most of the disks, the optical thickness is high; for instance, the invisibility of the central star through several edge-on disks led them to conclude that the edge-on optical depths $\tau_\nu > 10$. In such

circumstances, there is no detectable flux by which to measure extinction. MO96 took one-dimensional, radial slices across six of the disks, and fit the observed profiles to profiles expected from a variety of exponential and power-law disk models $\Sigma(R)$. They found that the disks were *not* well fit by sharp-edged models, and much better fits were found with smoothly truncated outer edges – *i.e.*, in the optically-thin outer edges, some disk structure was definitely resolvable.

The disk images differ somewhat from true 'maps,' in the sense that spatial smearing by the HST PSF distorts the visibility of small-scale features. For large-scale objects this is not a problem; however, the dark disks are quite small, often only several pixels across. At 0.5 μm, the 0.045" PC pixel size is comparable to the 0.053" FWHM PSF. The TinyTim package (J. Krist) can be used to simulate the PSF recorded on each of the HST detectors under a variety of conditions. In an ideal situation these PSF's could then be used to uniquely deconvolve the data images to resolve the disks' fine spatial structure. However, tests by MO96 indicated that deconvolutions were highly non-unique, and sensitive to the deconvolution parameters chosen. They suggested this was due to the near-zero DN at the disk centers in the deconvolved images. Nevertheless, using forward convolution techniques, they were still able to recover features at the sub-PSF level.

Based on their mass distributions and the non-detection of the central star, MO96 estimated lower-limit gas+dust disk masses in the range $10^{-7} - 10^{-4} M_{\odot}$. As they emphasized, these are strict lower limits, because the optical depths may be significantly higher than the observations can constrain. Furthermore, their study explicitly assumed small ($r = 200$ nm), ISM-like particles with a particularly high opacity-per-mass coefficient, perhaps further contributing to their disk masses.

In the MO96 study, only the brightest images were used, typically taken with the [OIII] and Hα filters. In nearly all the Orion disk observations, however, images have been taken through a much broader range of filters. Ostensibly since the disks are

'dark,' it does not matter through what filter they are imaged – the filters were chosen more in the interest of studying ionization regions, shock fronts, and outflows, than the silhouettes. However, the same observations may in fact also be used to study the silhouettes in different wavelengths, and constrain the particle sizes at the outer disk edges. A short digression on the optical properties of small particles is in order.

2.3.1 Light scattering by small particles

A dimensionless particle size parameter is commonly defined as

$$x \equiv \frac{2\pi a}{\lambda}, \tag{2.1}$$

where particles interact with light over a scattering cross-section $C_{\rm sca}$, defined as

$$C_{\rm sca}(x) \equiv \pi r^2 Q_{\rm sca}(x). \tag{2.2}$$

Light is extincted – *i.e.*, removed from a beam – with efficiency $Q_{\rm ext}$, where

$$Q_{\rm ext} \equiv Q_{\rm abs} + Q_{\rm sca} \tag{2.3}$$

and $Q_{\rm abs}$ and $Q_{\rm sca}$ are the efficiencies for absorption and scattering. An optical thickness can then be defined over a column density size distribution $N(r)$ as

$$\tau_\nu \equiv \int_0^\infty \pi r^2 Q_{\rm ext} N(r)\, dr \quad . \tag{2.4}$$

For spherical particles, Q can be calculated using Mie theory (*e.g.* Bohren & Huffman 1983), and one finds that the extinction efficiency decreases rapidly for $x < 1$ ($Q_{\rm ext} \sim x^4$, Figure 2.1), while it remains roughly constant for $x > 1$ ($Q_{\rm ext} \sim 2$, to account for both diffraction and true extinction of light striking the particle's physical cross-section). Therefore, by studying the extinction properties of an ensemble of scatterers, one can often determine some properties of the scatterers themselves – for

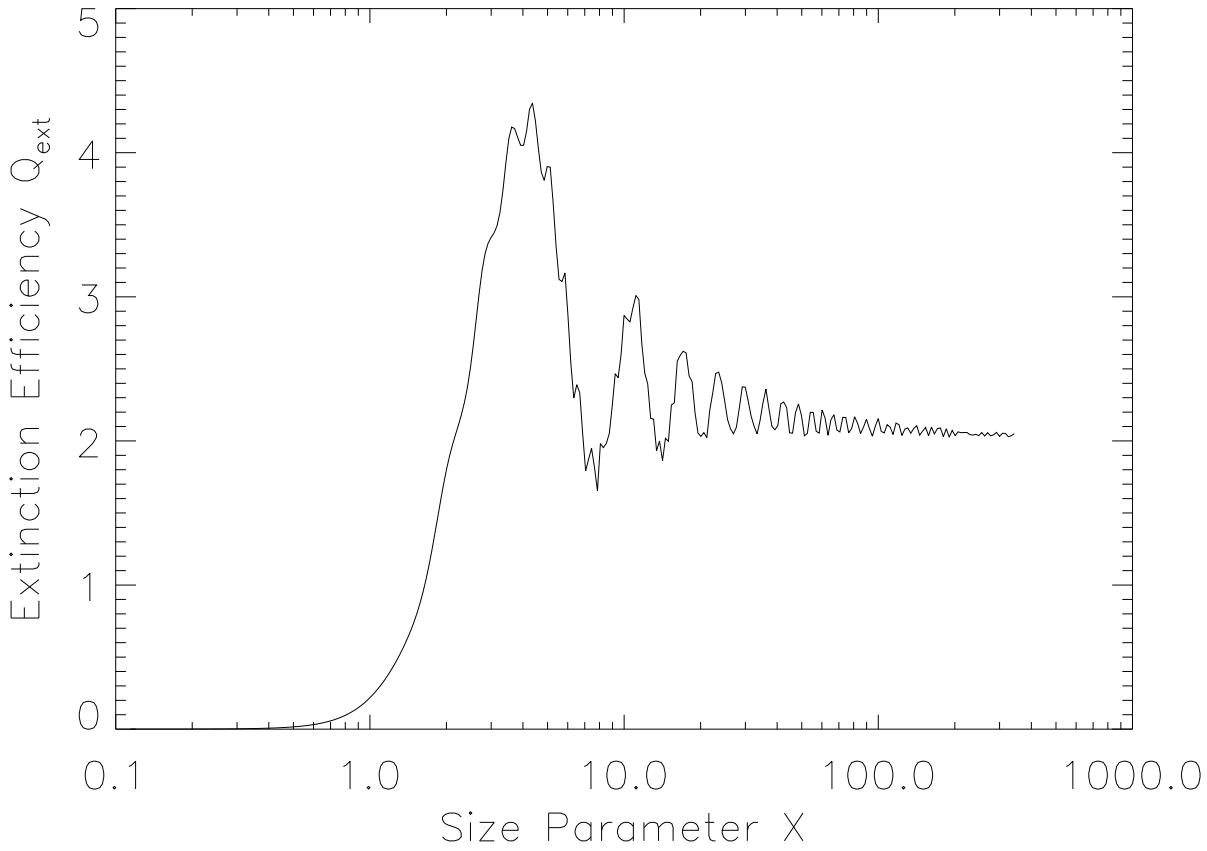

Figure 2.1: Extinction efficiency as a function of particle size. The smallest particles interact less strongly with light. Calculated with Mie scattering.

instance, whether they are small, or large. The wavelength dependence of $Q_{\rm ext}$ should be familiar to anyone who has recently seen a sunset or a moon rise – particularly beautiful over the most heavily polluted areas.

In an astrophysical context, star light is reddened by interstellar dust, and the properties of the dust can be determined by (for instance) the ratio of total to selective extinction, $R_{\rm v} = A_{\rm v}/E(B-V)$, where $A_{\rm v}$ is the visible-light extinction in magnitudes, and $E(B-V)$ is the difference in extinction between broad blue and visible filters. Dust properties in different regions can be quantified; for instance, typical ISM dust is characterized by $R_v \sim 3$ (Savage & Mathis 1979), while dust in the Orion nebula is measured to be $R \sim 5$ (Breger *et al.* 1981). Larger R can be naturally explained with larger particle sizes, and it is has been suggested that Orion's anomalously high R could be due to dust coagulation within the nebula (*e.g.* Cardelli *et al.* 1989).

For the dark disks, I make similar extinction measurements. Instead of star light being scattered by a diffuse interstellar background, however, nebular emission from the Orion HII region passes through and is extincted by particles in a disk. By measuring wavelength-dependent extinction in the outer disk edges, the dust properties may be directly probed.

2.4 Radial Profiles

I have generated radial brightness profiles from the visible and near-IR observations described in Table 2.1. The work by MO96 used one-dimensional radial slices through the data to describe the radial profiles of their six disks. This method, while simple, ignores the majority of the data points. To increase the S/N, I have instead measured 2D radial profiles, which increases by $f \sim 10$ the number of data points used. The process for generating the 2D profiles is relatively straightforward:

1. Calculate symmetric contours of equal brightness from the highest-quality images.

2. Bin the data by contour level.

3. Plot the median intensity along each contour.

In step 1, the brightest images (typically OIII, NII, and Hα) are used to define the contour levels. In step 2, these same contours are applied to measure all the images, under the assumption that the morphology of each disk is generally similar across λ, and varies only in intensity. Comparisons between the bright images support this assumption. Finally, in step 3, I take the median values – rather than the mean – in order to remove any strong effect of the central star, in particular for the SW disk. Examination of the data indicates that the star's flux has been successfully filtered.

Even in the optically thick portions of the disks, the measured DN values are significantly above zero. This is for at least two reasons: a) nebular emission emanates from in front of as well as behind the disks, and b) the HST PSF spreads flux from the bright background and central star onto the dark foreground. Quantifying the effects of the latter is easy but the former is difficult. Therefore, I have made the *a priori* assumption that the disks are optically thick near the center and optically thin far away, and normalized the profiles appropriately. In this way, the profiles for different wavelengths can be quantitatively compared.

Radial profiles for several disks are shown in Figures 2.8–2.10. I have focused on three disks: HST10 (aka 182-413, after the last digits of its RA and Dec), HST16 (183-405), and SW (114-426) (Figures 2.2–2.6). These three were chosen to be a representative, high-quality subset of the 47 known disks. HST16 is one of several large face-on disks; HST10 is the best resolved and largest of the many disks that appear to be photoevaporating, and edge-on SW is the largest of any of the Orion disks.

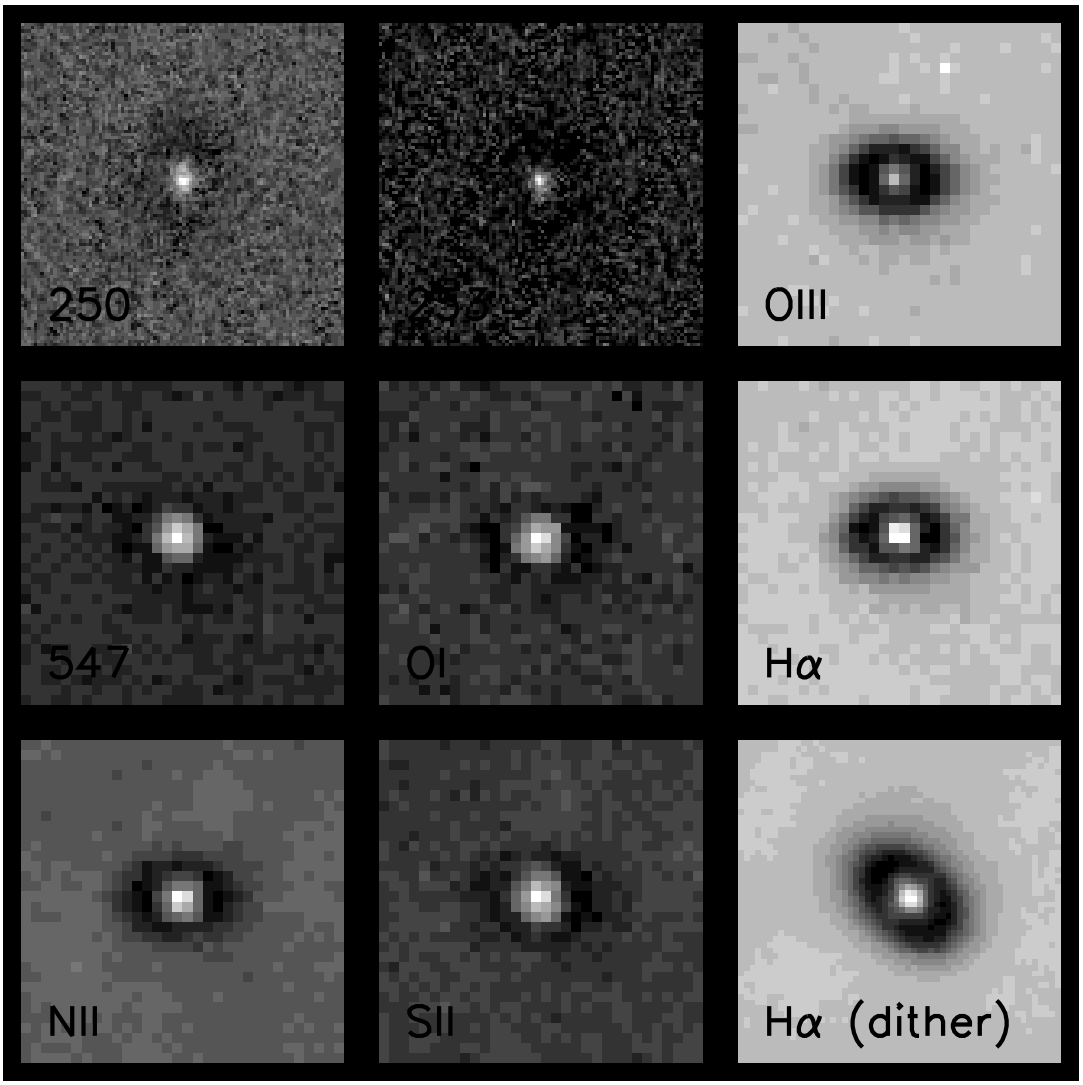

Figure 2.2: Silhouette images, HST16

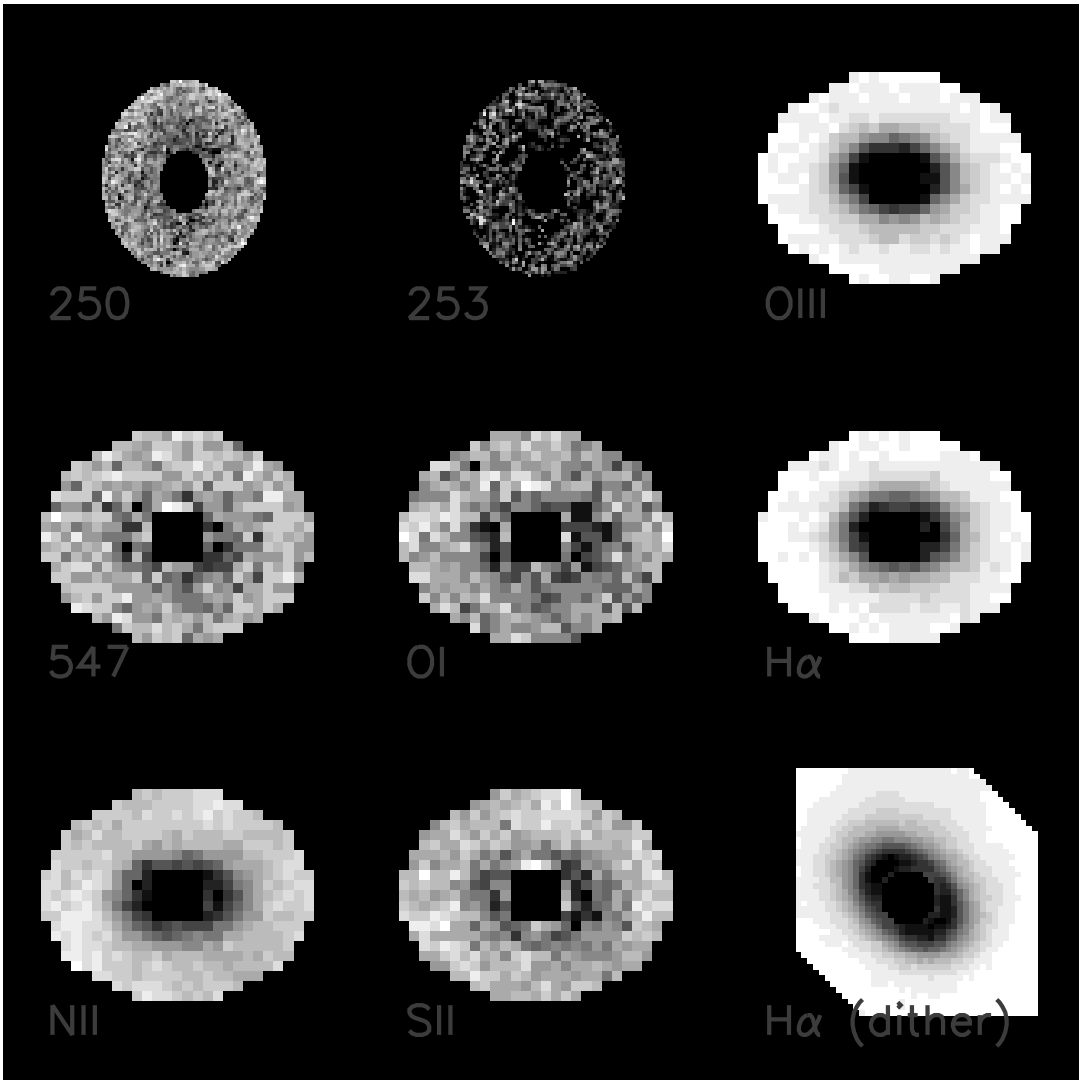

Figure 2.3: Masked silhouette images, HST16 (Section 2.5.3)

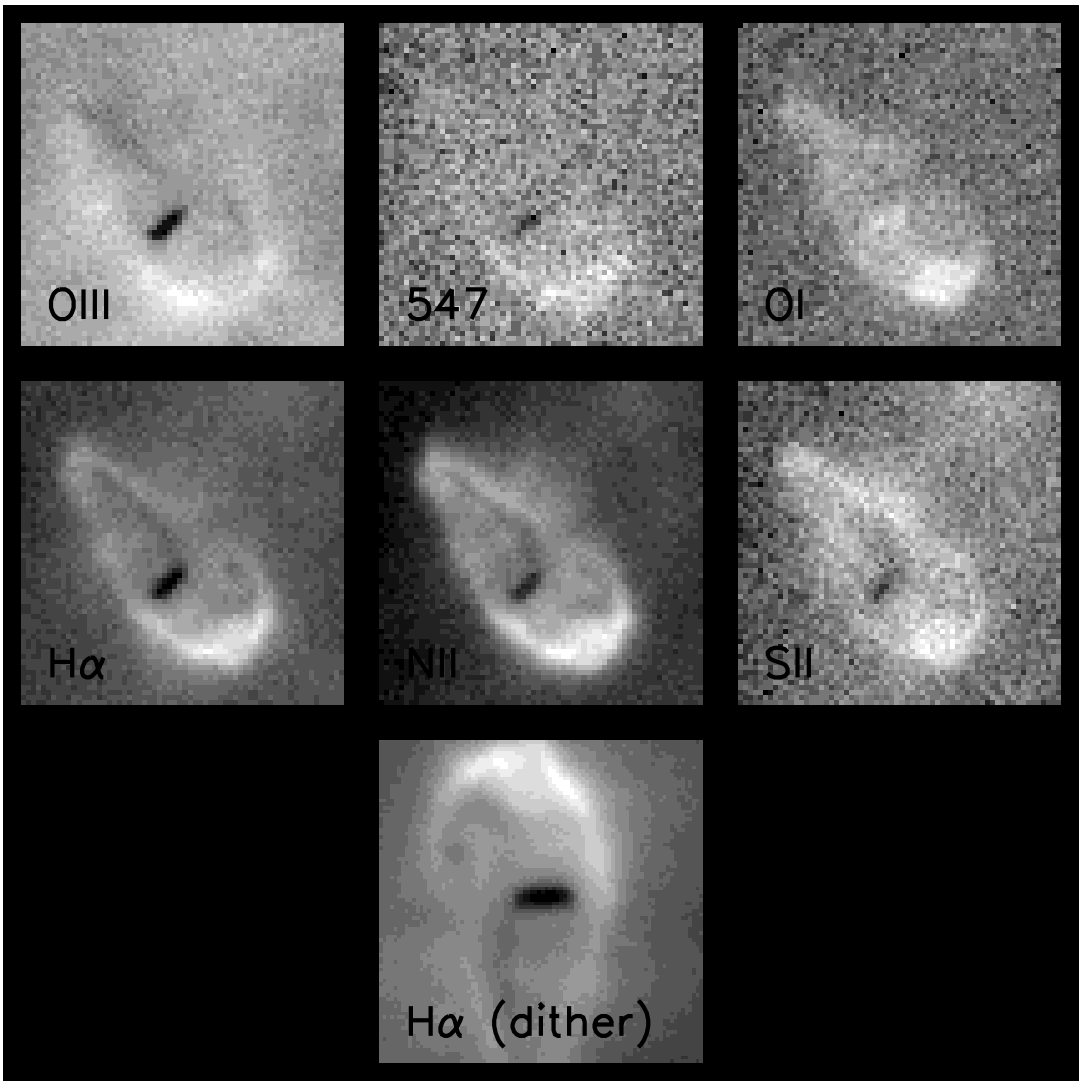

Figure 2.4: Silhouette images, HST10

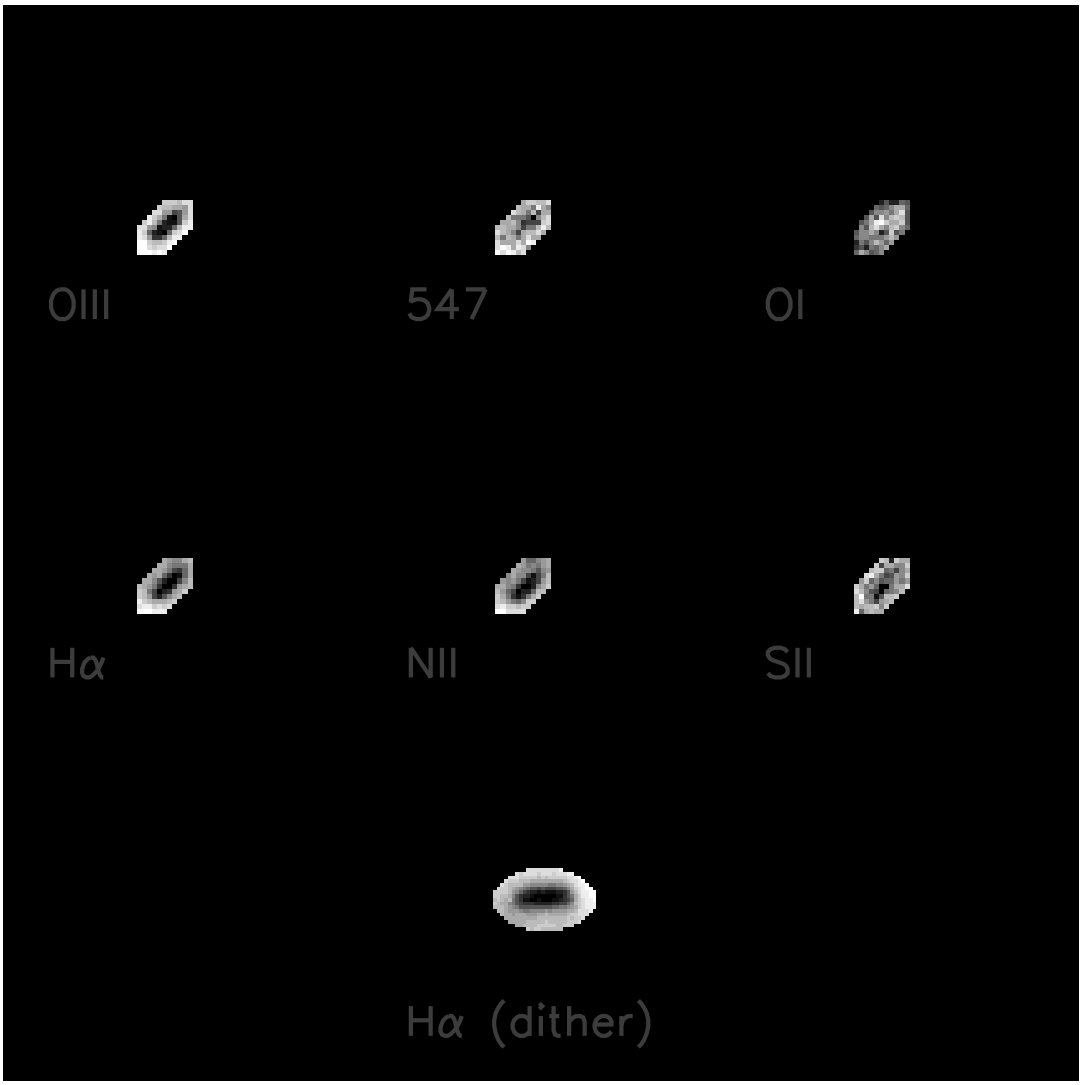

Figure 2.5: Masked silhouette images, HST10

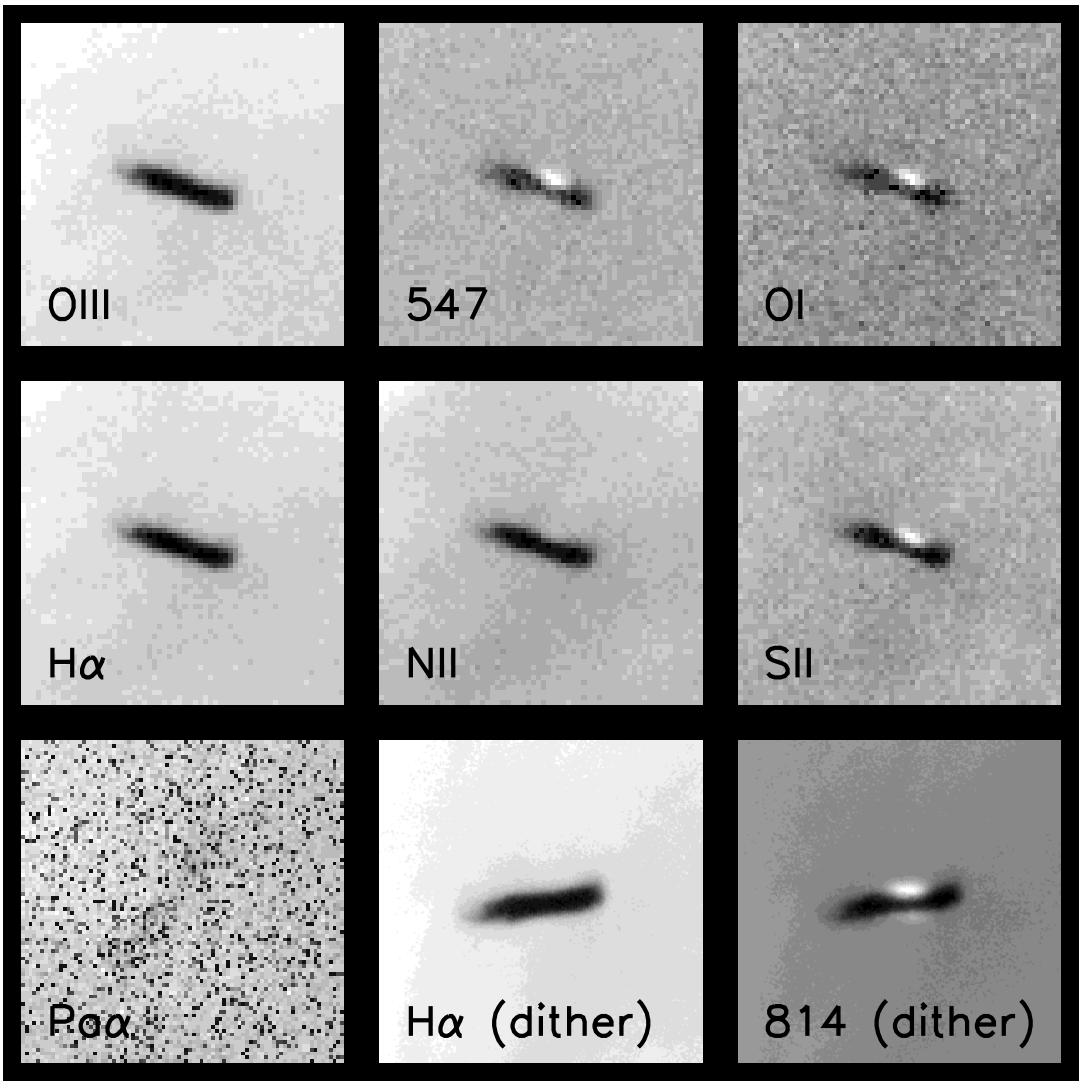

Figure 2.6: Silhouette images, SW disk

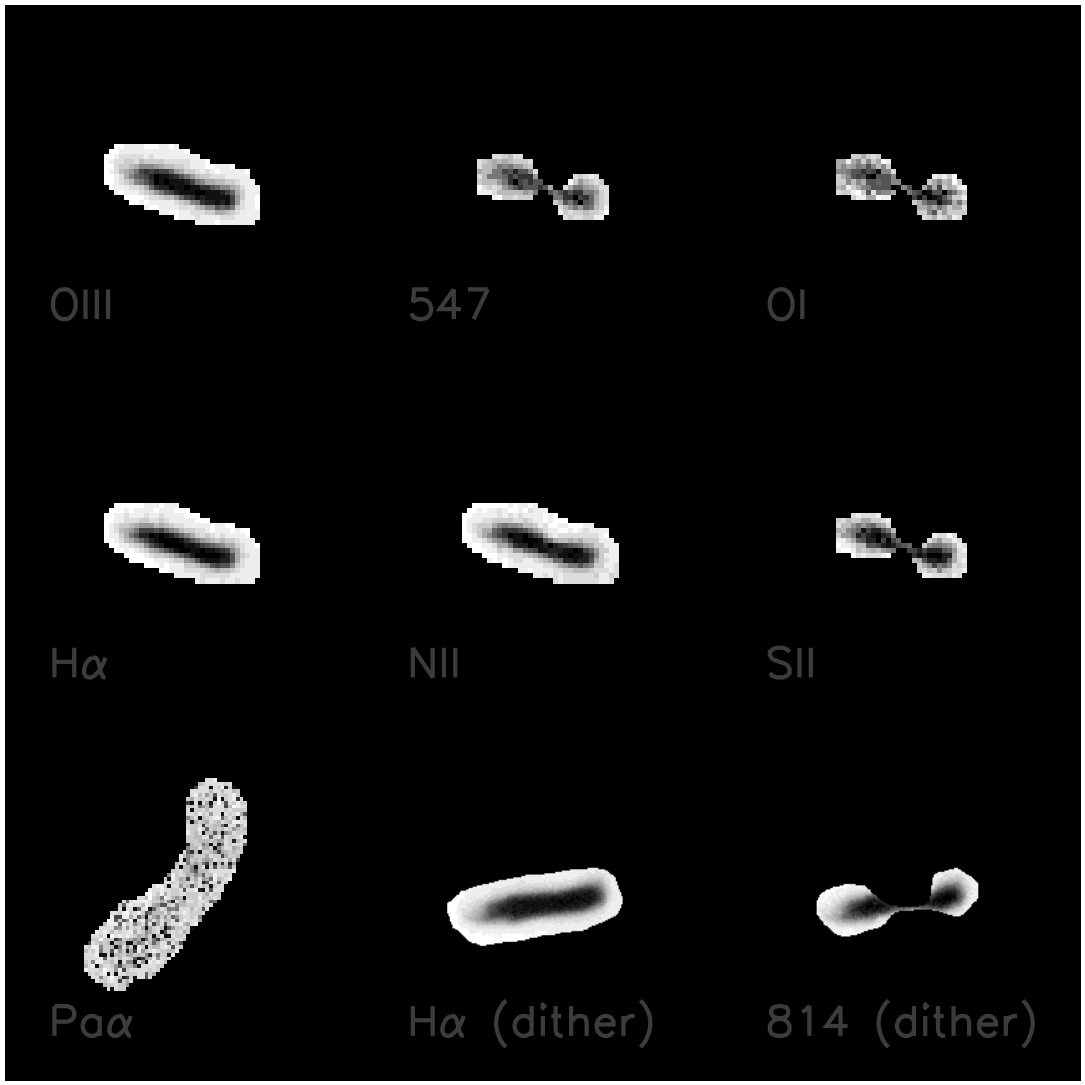

Figure 2.7: Masked silhouette images, SW disk

What is immediately obvious is that the disk profiles do not look dramatically different across the wavelength range. More interestingly, *there is no significant systematic trend in the disk profiles with wavelength.* The SW disk hints at a trend: the measurement at the shortest wavelength (502 nm, OIII) is consistently the largest disk, and the measurement at the longest wavelength (1.87 μm, Paα) is consistently the smallest disk; the sizes vary by $\sim 10\%$. McCaughrean *et al.* (1998) also noted this effect; using 1D profiles, they measured the Paα disk to be $\sim 20\%$ smaller than the visible images. They then proposed that the disk was populated with small particles at its outer edge, which accounted for the apparent change in size.

To assess whether the measured difference is statistically significant, the sources of error must be considered. Sources of error can be either systematic or random. Systematic errors that could cause deviations in the profiles include stellar contamination, disk asymmetries, and spatial variations in the background and foreground flux. Random errors are dominated by Poisson shot noise, which is straightforward to consider.

The Paα SW disk image is among the most underexposed of the image set used here; the median DN value is 17, compared with DN $\sim 80-100$ for the brightest images of the same disk. Examining the image, it appears plausible that shot noise, on order ΔDM ~ 4, could significantly affect the radial profiles.

To investigate this effect, I created seven model images of the SW Paα disk. Each image was identical to the data image in general noise characteristics; the actual DN values of the model images were drawn from the edges of the data images. A rotated, flat disk was projected onto the model images at a similar brightness level to the data ($\mathrm{DN_{disk+HII}/DN_{HII}} \sim 0.7$), and then convolved with the appropriate PSF. Each model image was identical in parameters and varied only with the random placement of shot noise. Finally, each of the model images was used to generate a radial profile in the same fashion as the data disks. As the results in Figure 2.11 show, there is wide scatter in the radial profiles, and this scatter is comparable to that in the data profiles. Therefore,

within purely statistical errors, it cannot be concluded that there is any size difference difference between the SW disk images.

Systematic errors such as azimuthal variations in the disk and background could also affect the profiles. The SW disk can easily be seen to be non-axisymmetric in several of the images. For instance, the central star (visible indirectly by the reflection nebula) appears to be displaced from the disk's apparent center in the continuum image, and a large patch of low optical depth can be seen off one end of the disk in the dithered Hα image (both Figure 2.6). The latter feature – visible in particular in the best-exposed images – appears to contribute to the apparent large size of the OIII SW disk. Measurements of the HST10 disk, being at the center of a photoevaporation region with complex structure, may also be affected by background asymmetries. Evidence of this structure contributing to errors in the HST10 measurements can be seen in the radial profiles (Figure 2.9).

Because the statistical errors are easily quantifiable, I have applied them to each of the disks in each of the wavelengths, using the same technique. The disk HWHM sizes and errorbars are plotted in Figures 2.12-2.14. For none of the disks is there a visible trend between size and wavelength – that is, *the disks appear to be entirely achromatic.*

The most obvious interpretation of these results is dramatic: we are directly observing extinction by large grains in the disks. These particles are unlike Orion ISM particles or any other dust grains ever observed in an astrophysical context. Rather than $R \sim 5$ typical of the Orion region, the disks show $R \gtrsim 50$. The work of McCaughrean & O'Dell (1996) indicated that the disks were *not* sharply truncated, and the outer edges were optically thin. Therefore, the effect shown here does not appear to be a byproduct of sharp, 'top hat'-style edges bounding a disk of small particles.

It is clear that the long-wavelength images allow far greater leverage than the visible images do. Near-IR images of HST10 and HST16 do exist. Unfortunately,

neither of these observations are usable: the pixel scale of the HST10 image is simply too coarse, and background flux in the HST16 image is overwhelmed by that from the IR-bright central star. Being much smaller disks than SW to start, spatial resolution is degraded by another factor of 3 in the near-IR.

The *data* analysis presented here is not sufficient to constrain the disk characteristics – disk size, mass, vertical profile, and so forth – beyond those already known from other studies such as McCaughrean & O'Dell (1996). Detailed determinations of the disk properties requires a more sophisticated analysis; for instance, a 3D physical model, or higher-resolution imaging at longer wavelengths.

2.5 Monte Carlo Parameter Modeling

Data inversion – the process of turning a set of measurements into a set of physical properties – is a classic and often challenging problem. In this section, I will examine the inversion problem as applied to the Orion disks. The measurements in hand are the HST silhouette disk observations, and we wish to best determine physically useful properties of the disks: for instance, their size, shape, composition, and mass.

The connection between the data and the physical parameters is sometimes simple, and sometimes complex. In this case, key physical processes that need to be understood to make the connection between the two include a) the physical structure of the disk; b) the light scattering of particles in the disks by the nebula; c) optical properties of the telescope and detector; and d) subsequent processing of the resulting images. In many circumstances, the connection between measurements and physical properties can be made uniquely, in both the forward and backward directions. Unfortunately, due in part to challenges described in the previous section, the inverse problem can not be easily solved – that is, because of non-uniqueness of deconvolving an image that has been convolved by a PSF, the properties of the Orion disks cannot be directly 'measured' from the data.

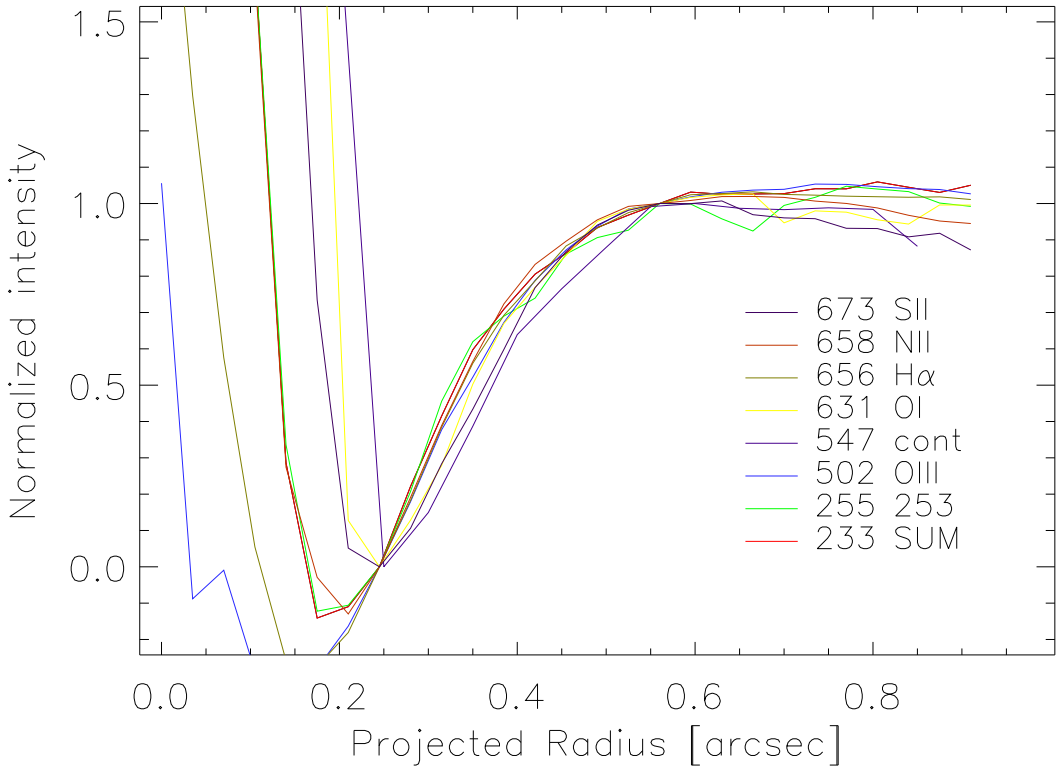

Figure 2.8: Radial profiles, HST16. The x-axis indicates distance projected by a tilted disk, and is very nearly along contours of equal brightness. The y-axis plots the brightness level, normalized near the inner and outer disk edges. On this disk, the brightness near the inner edge is due to the central star, which appears brightest through the widest filters.

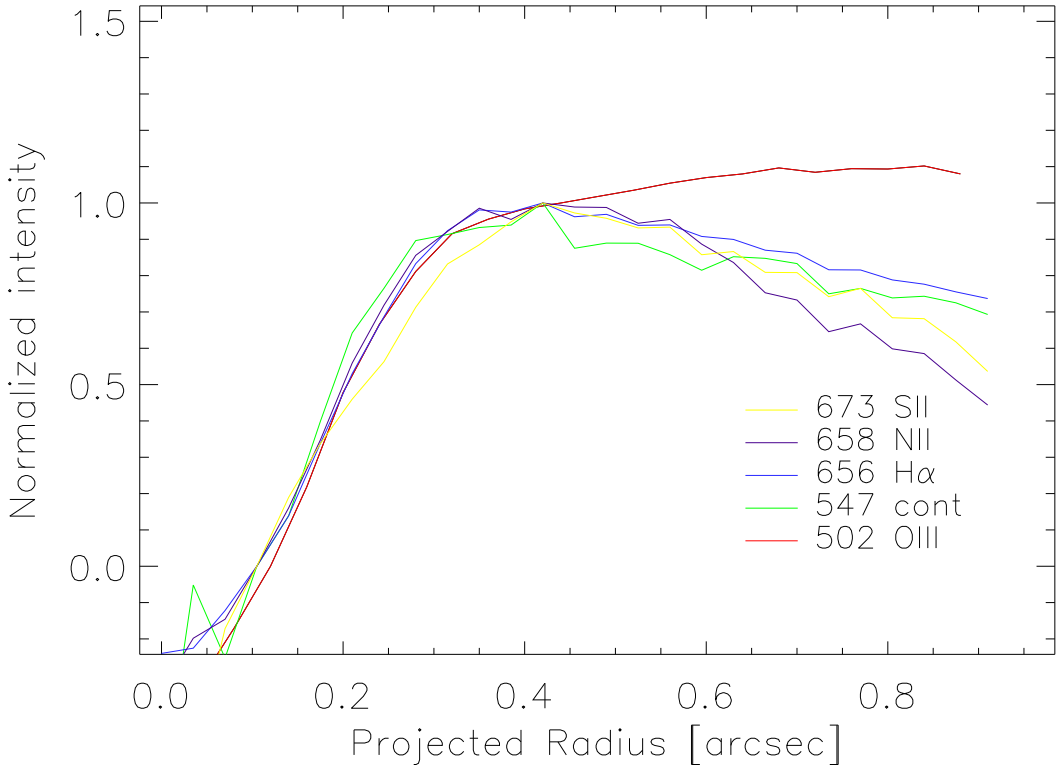

Figure 2.9: Radial profiles, HST10 disk.

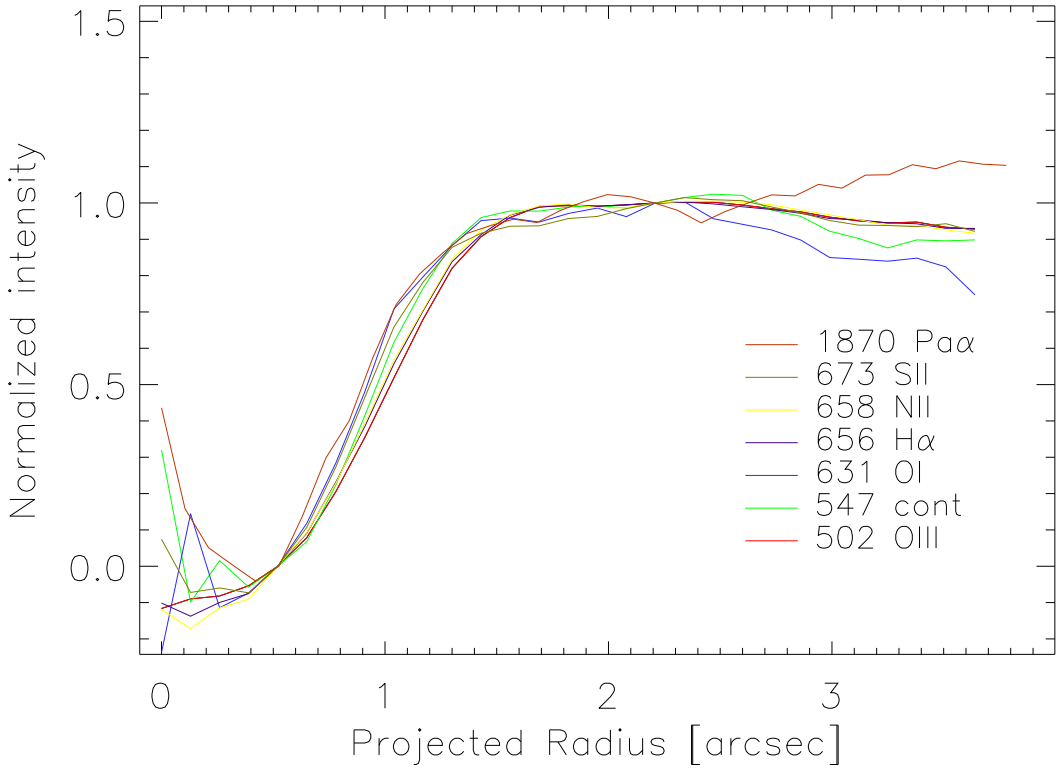

Figure 2.10: Radial profiles, SW disk.

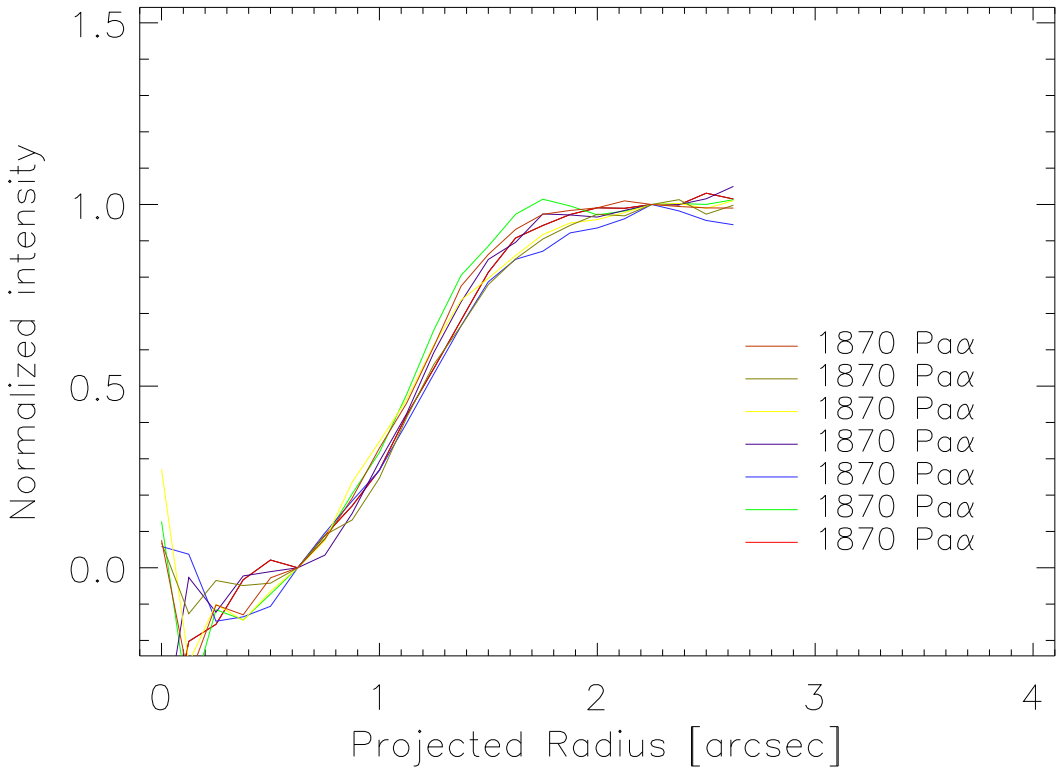

Figure 2.11: SW disk, Paα, error estimates. Seven model images were created with similar Poisson noise statistics and disk brightness as the observed Paα image. The model images were all created with identical parameters. Because of the image's low S/N, although the disk *appears* slightly smaller in Paα than OIII (Figure 2.10), this result is indistinguishable from noise. As with the data figure, the disk also appears brighter at the center, but this is purely an effect of Poisson noise coupled with a smaller number of pixels in the central annuli.

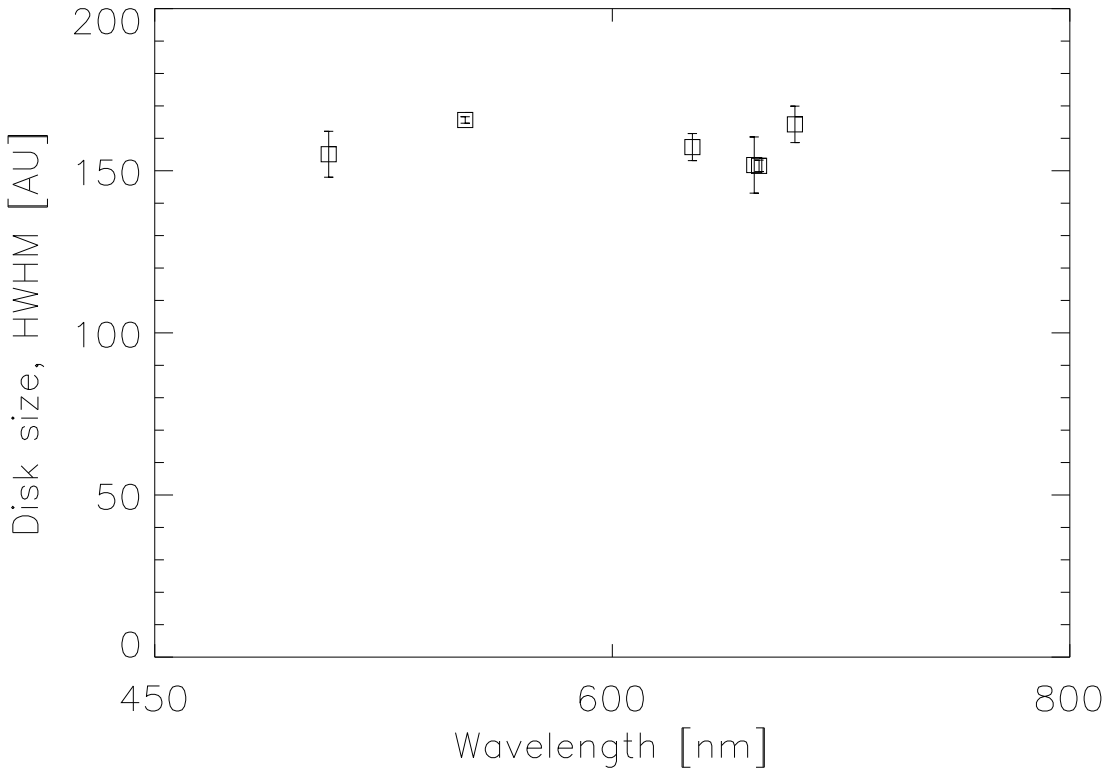

Figure 2.12: Disk sizes, HST16. The error bars for each wavelength are generated in a fashion similar to that for Figure 2.11

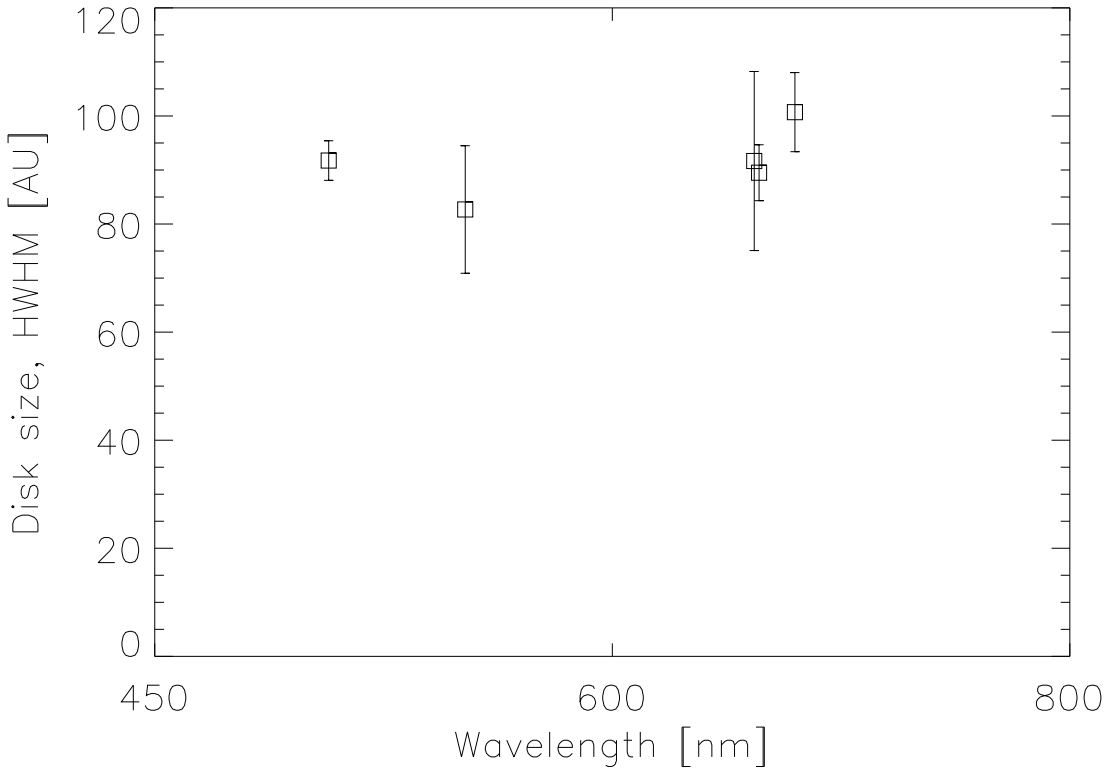

Figure 2.13: Disk sizes, HST10.

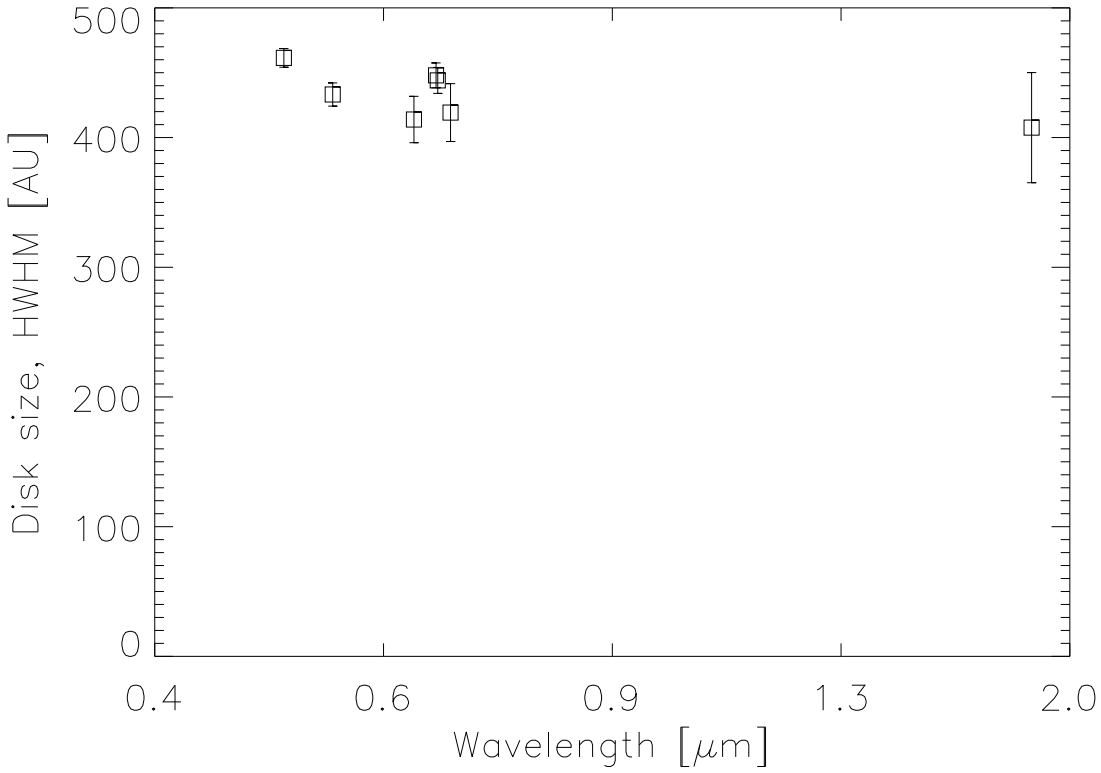

Figure 2.14: Disk sizes, SW disk.

However, the forward problem is often more easily solved. Given – in this case – a distribution of dust being scattered and imaged by a well-characterized system, we can accurately predict the result using basic physics. This situation suggests an approach: rather than invert the data to determine the disk properties, we generate a model disk from a set of assumed parameters, process this model forward through steps a)-d) above, and test if the model matches the data. If it does, we have found a satisfactory model; if not, either the parameters or the assumptions must be changed.

The study of MO96 took exactly this approach. They wished to determine the disk surface density profiles $\Sigma(R)$. Although they were unable to directly measure the profiles, they constrained the profiles by generating several model disks, projecting these onto a 2D surface, and convolving them with the HST PSF. Their disks were specified by three parameters: a) the outer radius R of an opaque disk, b) the functional style of the outer disk density $\Sigma(R)$ (exponential, power law, or Gaussian), and c) the exponent for the outer edges. They found several disks that qualitatively fit the data well, listed in Table 2.2.

However, this study was deficient[1] in several ways – that is, they chose fewer parameters than required to properly characterize a disk. Specifically, their model a) assumed a 2D (flat) disk, although inspection of several of the disks indicates that they are edge-on and poorly approximated by such a model; b) assumed no wavelength- or size-dependence of particle scattering properties; and c) assumed the brightest images of each disk to be representative, and did not use the broad range of filters through which images had been taken.

[1] Any finite-parameter study will be deficient; the issue is only a matter of degree. A healthy number of deficiencies exist in the present model as well, and the usual challenge is to hide them as quietly as possible.

Table 2.2: Best disk fits, McCaughrean & O'Dell (1996). Includes only those disks studied by both McCaughrean & O'Dell (1996) (six disks) and the present work (three disks).

Disk	Filter	Inner Radius	Inclination	Disk Surface Density	Disk Mass	
HST16	OIII	0 AU	45°	$\Sigma \sim R^{-4.5}$; $\tau(R = 108 \text{ AU}) = 1$	$> 2.6 \times 10^{-5} M_{\odot}$	†
HST16	OIII	85 AU	45°	$\Sigma \sim \exp[-R/(25 \text{ AU})]$	$> 2.6 \times 10^{-5} M_{\odot}$	
SW	OIII	70 AU (vertical)	$\gtrsim$ 80°	Gaussian	$> 2.2 \times 10^{-4}\ M_{\odot}$ †	

† Corrected mass, as per McCaughrean *et al.* (1998).

2.5.1 Disk Modeling Method

I determine the disk properties using a forward convolution of the disk model, which is determined by a small number of parameters. My model removes the three identified deficiencies of the MO96 model. The general approach is similar; however, my model considers significantly more parameters, more data, and a more complete analysis to determine the goodness-of-fit.

This method (flowchart, Figure 2.15) breaks the model into four distinct stages: a) generation of a 3D disk model; b) scattering light through the disk and creating a 2D silhouette; c) convolution into a DN-scaled image, and d) comparison between the data and the model. I will now examine each of these steps.

3D disk parameters

The disk is modeled to be a three-dimensional cylinder of inner radius R_1, outer radius R_2, half-height h, with particle size distribution $n(r)$. Within the cylinder, the particle density is taken to be

$$\begin{aligned} n(R) &\sim R_1^{-k_r} && R < R_1 \\ &\sim R^{-k_r} && R_1 < R < R_2 \\ &= 0 && R > R_2 \end{aligned} \tag{2.5}$$

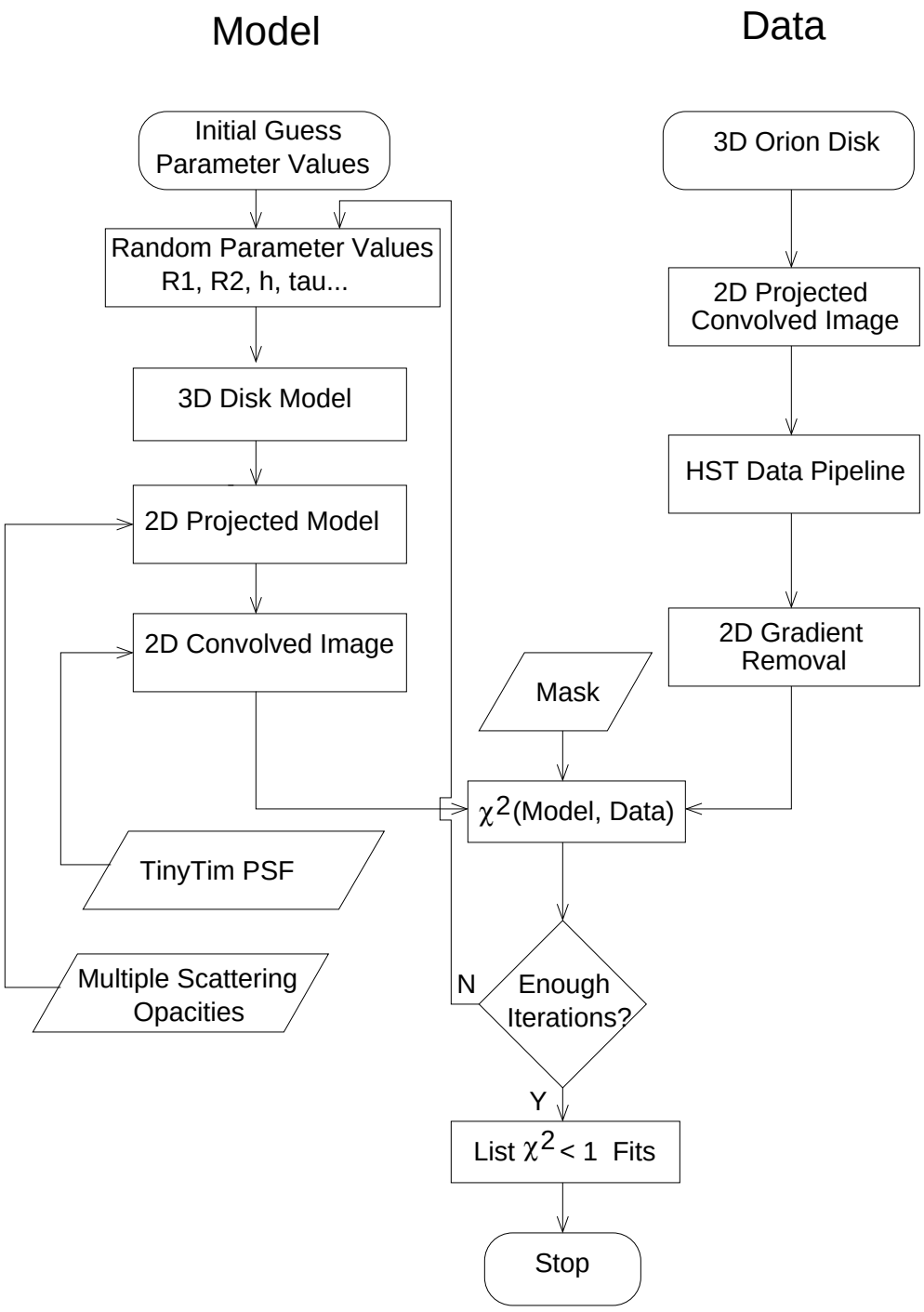

Figure 2.15: Flowchart, BASIL model

Table 2.3: 3D model disk parameters: initial guesses

Name	Parameter	HST16	HST10	SW	Variable?
Inner radius	R_1	$0 - 135$ AU	$0 - 90$ AU	$0 - 540$ AU	$\surd$
Outer radius	R_2	$135 - 270$ AU	$45 - 135$ AU	$320 - 540$ AU	$\surd$
Half-height	h	$20 - 90$ AU	$4.5 - 45$ AU	$4.5 - 135$ AU	$\surd$
Mass exponent	k_r	$0 - 7$	$0 - 7$	$0 - 7$	$\surd$
Edge-on optical depth	$\tau_{\max}$	$5 - 500$	$5 - 5000$	$5 - 5000$	$\surd$
Inclination	θ	$40 - 60°$	$60 - 90°$	$60 - 90°$	$\surd$
Foreground emission	E	$0 - 1$	$0 - 1$	$0 - 1$	$\surd$
Particle albedo	a	0, 0.3, 0.9	0, 0.3, 0.9	0, 0.3, 0.9	$\surd$
Particle size exponent	q	$1 - 5$	$1 - 5$	$1 - 7$	$\surd$
Particle size range	r_0	0.01 μm $-$ 1 cm	0.01 μm $-$ 1 cm	0.01 μm $-$ 1 cm	
Particle asym. factor	$\langle g \rangle$	1	1	1	
Wavelength	λ	$232 - 673$ nm	$502 - 673$ nm	$502 - 1870$ nm	
Rotation angle	ϕ	263/0/138	45/0	163/232/9.4	
Central pixel location	x_0, y_0	± 2	± 2	± 2	
Mean emission angle	μ	1	1	1	
Distance	d	450 pc	450 pc	450 pc	

$$\begin{aligned} n(z) &\sim 1 - \left|\frac{z}{h}\right| && |z| < h \\ &= 0 && |z| > h \end{aligned} \tag{2.6}$$

$$\begin{aligned} n(r) &\sim r^{-q} && r_0 < r < r_1 \\ &= 0 && r < r_0 \quad \text{or} \quad r > r_1 \end{aligned} \tag{2.7}$$

$$\begin{aligned} n(R, z, r) &= c_1\, n(R)\, n(z)\, n(r) \qquad \text{such that} \\ \tau_{\max} &= c_1 \int_0^R \int_0^r n(R, z = 0, r)\ \pi r^2(r)\ dr\, dR \end{aligned} \tag{2.8}$$

Several additional parameters specify the disk's physical orientation, including the tilt angle θ, rotation angle ϕ, and sub-pixel detector position x_0, y_0. This parameter set (Table 2.3) is essentially a combination of parameters used in the MO96 Orion disk study, and the Burrows *et al.* (1996) study of the dark accretion disk within HH30 in Taurus. The major difference is the addition of a power law particle size distribution.

2.5.2 3D Disk Light Scattering Model

After the 3D disk is created, I simulate light from the background illumination source as it passes through the disk, through the ISM, and to the observer. The light scattering situation here is somewhat unique, because a) the illumination source is broad over solid angle, and thus scattering is not characterizable by a single phase angle, and b) the disk is optically thick and single scattering may be an oversimplification. Thus, the problem is significantly different from other physical situations such as β Pic-like debris disks or planetary rings. In both these cases, the light source position is well known and calculating the observed disk from the parameters is a straightforward matter of summing the phase function and scattering efficiency from each particle (*e.g.*, Chapter 4). In the dark disks, however, the scattering angles cover a broad range, and multiple scattering must be considered.

I address both issues by using the tabulated, multiple-scattering results of van de Hulst (1980). In this work, the author calculates the intensity resulting from a uniform background of radiation ($\Omega = 2\pi$ sr) passing through an optical depth τ of particles with albedo a and scattering asymmetry factor $\langle g \rangle$. Although the Orion light source is probably not entirely isotropic, it would be hard to justify a more complex model given the broad and unknown illumination source geometry. I quantize the albedo $a = [0, 0.2, 0.9]$, and for simplicity adopt $\langle g \rangle = 1$. Given these conditions, it is straightforward to use the tabulated results (Figure 2.16) to calculate the intensity $I(\tau_\nu)$ emerging from an illuminated column of optical depth τ_ν. I smoothly interpolate his results for values of τ_ν not explicitly given.

The study of Burrows *et al.* (1996) approached a similar multiple scattering problem in a different way, by using a Monte Carlo code to explicitly track the path of photons scattered through the internally illuminated HH 30 disk. For most of the disk, they found the multiple scattering correction to be minimal.

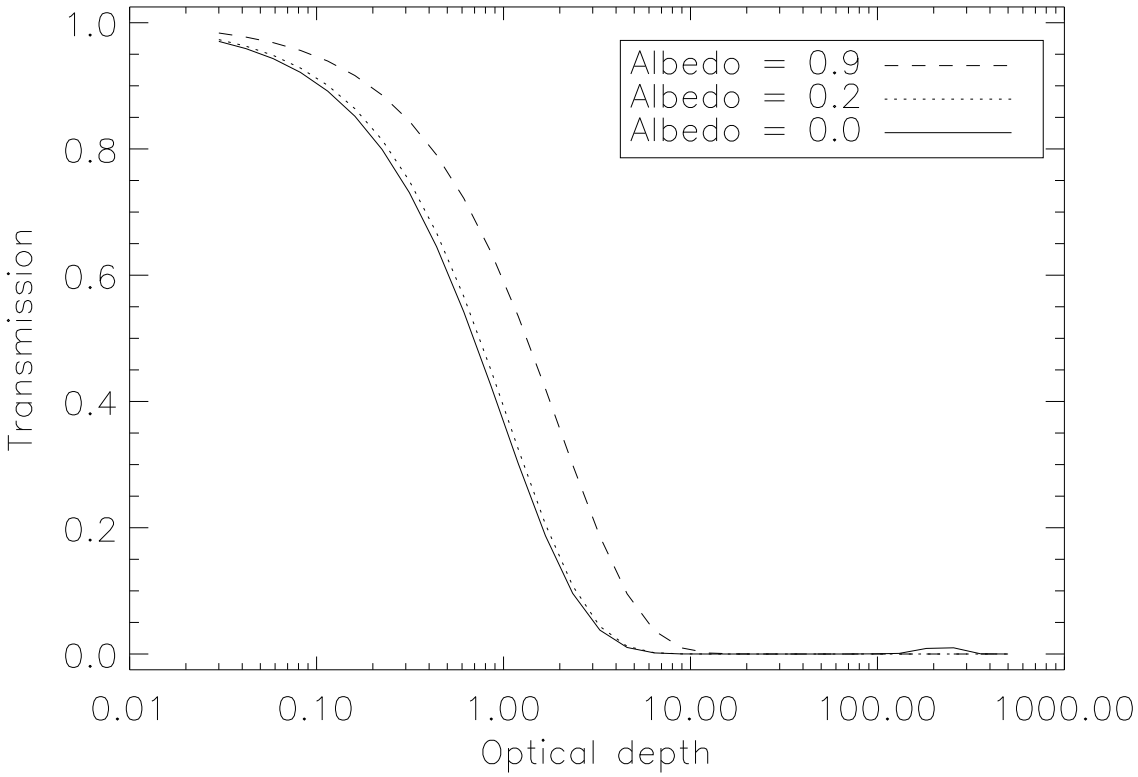

Figure 2.16: Multiple scattering results based on tabulated results of van de Hulst (1980). The light source is a diffuse field over 2π sr, illuminating a slab of particles of a given optical depth and albedo.

Nebular foreground emission is accounted for with the term E_ν, the ratio between foreground brightness and the total off-disk brightness. E_ν is taken to be uniform across the image.

Finally, after the map of intensities must be turned into an image. The disk is convolved with an appropriate TinyTim PSF for the HST filter and instrument. The model image is then scaled linearly so the mean background intensity matches that of the data. No noise is added to the model image.

The data images are the 'Rosetta stones' of this research, and it has been my philosophy to handle them with the minimal processing possible. Two minor transformations have been performed on the data: a) most images have had a local linear ($I = ax + by$) background subtracted, and b) the three FOC images have been summed. The former significantly improves the fit quality; the latter is necessary to derive any useful information from the severely underexposed images. In all other regards, the data are as supplied by the standard STScI data pipeline.

2.5.3 Comparison between data, model

A standard merit function can be used to determine both the best-fit models and quantitatively how good these models are. Although many metrics exist with various features, I have chosen the χ^2 test as it is well-known and easy to interpret.

I use a direct χ^2 comparison between the data and model at each wavelength, given a set of parameters $\mathcal{P}$. The same $\mathcal{P}$ can be applied at each wavelength, and a wavelength-weighted $\chi^2(\mathcal{P})$ calculated:

$$\chi^2_\nu(\mathcal{P}) \equiv \sum_{ij \text{ where } \mathrm{Mask}_{\nu ij} \neq 0} \frac{(\mathrm{Data}_{\nu ij}(\mathcal{P}) - \mathrm{Model}_{\nu ij})^2}{\sigma_\nu} \tag{2.9}$$

$$\chi^2(\mathcal{P}) \equiv \frac{1}{n_\nu} \sum_\nu \chi^2_\nu(\mathcal{P}) w_\nu \quad . \tag{2.10}$$

The standard deviations σ_ν for each image are measured directly from the image backgrounds and assumed to spatially uniform. The noise characteristics are observed to be roughly Poisson, although some non-Poisson components exist and variation is seen across the image. For simplicity I assume the weighting factors $w_\nu = 1$, although it might also be reasonable to weight the images by a measure of their relative quality, for example by σ_ν. The masks $\mathrm{Mask}_n u$ are used to select points to be included or excluded from the χ^2 fit; for instance, stellar continuum seen in the wide filter images is not expected to fit the model images, so these regions are excluded. The masked images are shown in Figures 2.3, 2.5, and 2.7.

The entire problem then reduces to finding a set of $\mathcal{P}$ such that $\chi^2(\mathcal{P})$ is sufficiently small. Given the infinite number of $\mathcal{P}$ and a finite amount of time, it is not possible to calculate (2.10) for *all* $\mathcal{P}$, but only for a small subset. MO96 chose the subset manually, and qualitatively judged the goodness-of-fit. Burrows *et al.* (1996) chose the subset by using an iterative root-finding method (the Levenberg-Marquardt algorithm, Press *et al.* (1992)) to locate good solutions using a χ^2 metric. My initial attempts with a similar method were unsuccessful because too many 'good' sets $\mathcal{P}$ were found that did not in fact fit well; that is, the algorithm converged too easily, and it appeared that the final results were strongly biased by the initial parameter guesses.

I instead chose to use a Monte Carlo method, which generates a large number (but finite, $N \sim 10^5$) of random $\mathcal{P}$ across the 9-dimensional parameter space. Given this large set of 'data,' islands of good fit can then be located, described, and cross-correlated. For a large-dimensional parameter space ($D \gtrsim 3$), this method was found to be more efficient than creating a D-dimensional grid and calculating χ^2 for every grid location. The Monte Carlo method has the general advantage of being non-biased and searching equally for solutions in every area of the parameter space. With any method, of course, the process may still be iterative; for instance, $\mathcal{P}$ can taken to be initially broad (values in Table 2.3) and narrowed significantly after an initial run.

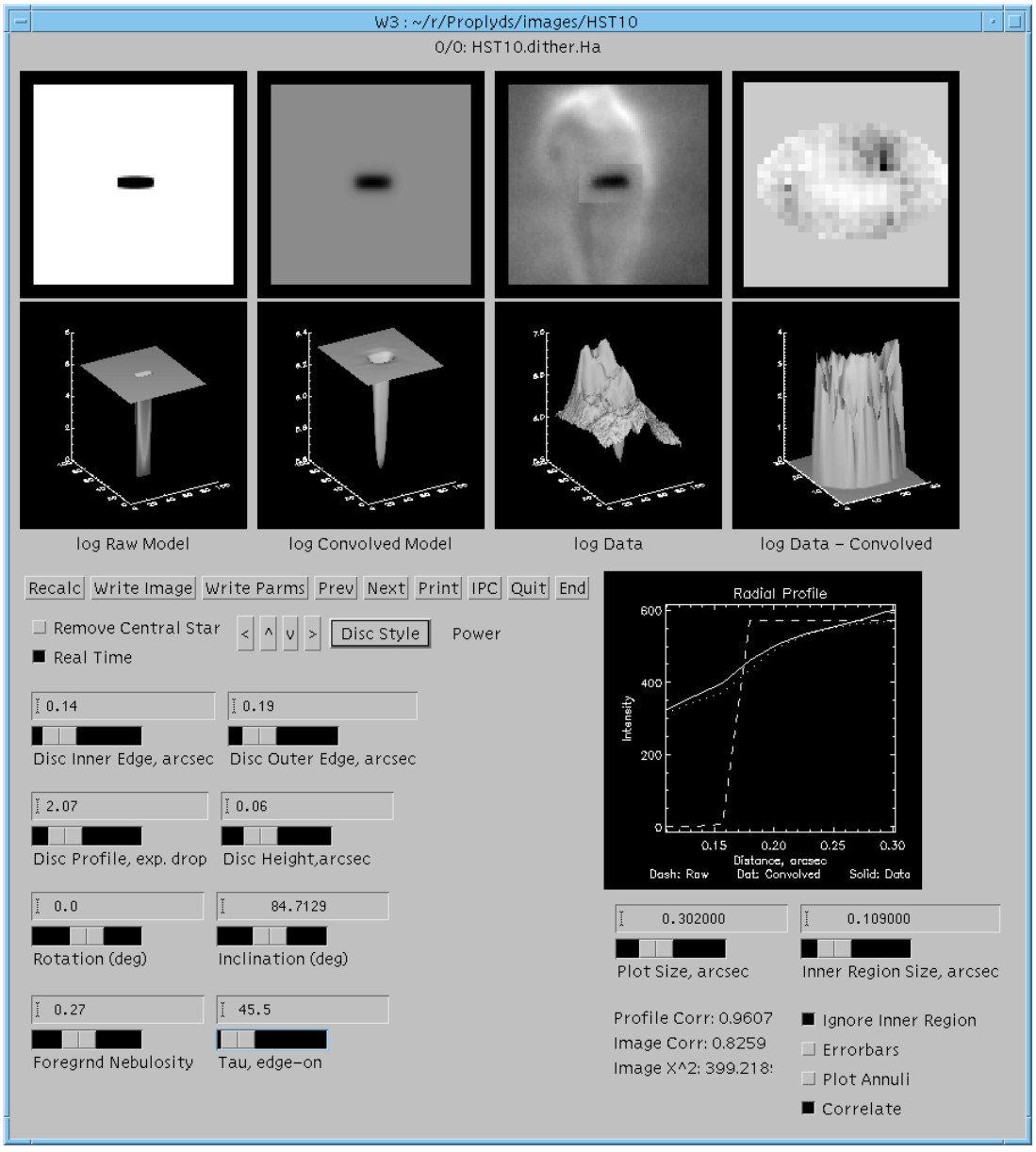

Figure 2.17: Part of the BASIL model, for one disk. Shown in the three horizontal windows are a raw projected disk model $\tau(x, y)$, a convolved model, the data, and the residuals. The disk is specified by 9 parameters, which can be fine-tuned by hand.

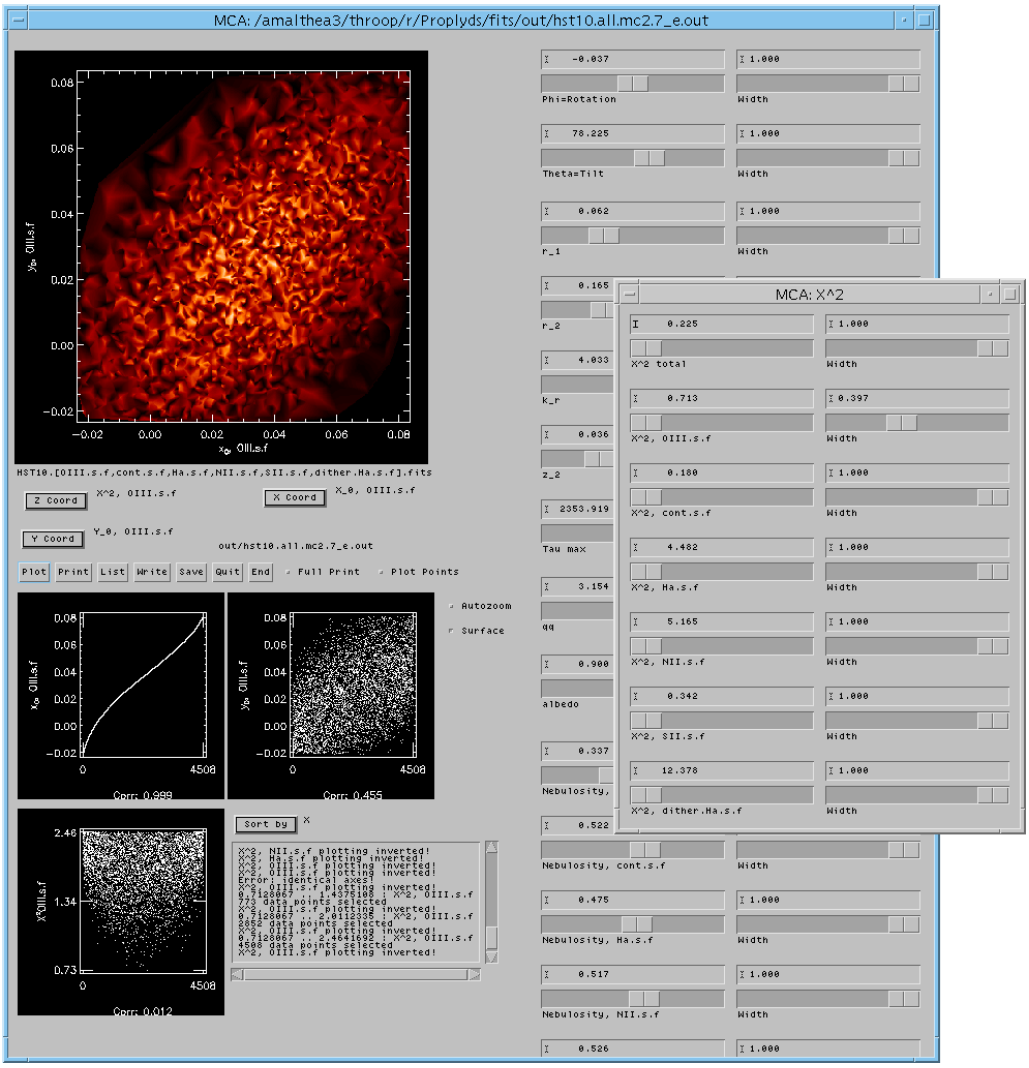

Figure 2.18: Results from Monte Carlo run, as visualized in the BASIL model. The 9-dimensional data cube is sliced and flattened along selected axes by set criteria. In this particular image, 4500 data points have been selected from the 130,000 iterations, and χ^2 is plotted in the large window as a function of x_0 and y_0. Brighter points indicate lower χ^2. The three smaller windows show cross-correlations between χ^2 and each $\mathcal{P}_i$.

For each run, the nine checked parameters in Table 2.3 are varied; the six remaining parameters are either measured or assumed. Parameter E_ν is varied for each wavelength, while the remaining parameters are fixed.

2.5.4 Monte Carlo Results

Model parameters can be found for each of the disks that consistently fit the data well. Images based on the best-fit parameters for each of the three disks are shown in Figures 2.19–2.20. Typical values for good fits are $\chi^2(\mathcal{P}) \lesssim 1$; however, there is a factor of several uncertainty in the quantitative goodness-of-fit values, due to spatial variation of σ_ν and instrumental effects causing non-Poisson noise characteristics. The fits are good in the sense that subsequent 'fine tuning' of the best fits by hand did not yield significantly lower residuals.

In most cases, the residuals are on the $3-6\%$ level, and are due to three components: a) spatial nonuniformities of the nebular emission; b) asymmetries inherent to the disks; and c) shot noise across the images. The first two terms dominate for the brightest, highest resolution data (Hα, OIII, NII, and most of the SW images), while the last term dominates for the lowest-quality images (continuum, FOC, and NICMOS). The residuals for the best-fit models show little or no systematic dependence on projected radius.

Regions of good fit can be characterized by examining the dependence of $\chi^2(\mathcal{P})$ on each parameter – or better, as a function of multiple parameters, because the disk model has many intertwined dependencies. Plots of key parameters for each disk are shown in Figures 2.22–2.25, and I will now individually examine the fits for each disk.

HST16

HST16 provides the highest quality data set I use, and models at most wavelengths fit extremely well. Data quality is poor for the FOC and F547M PC images, in both

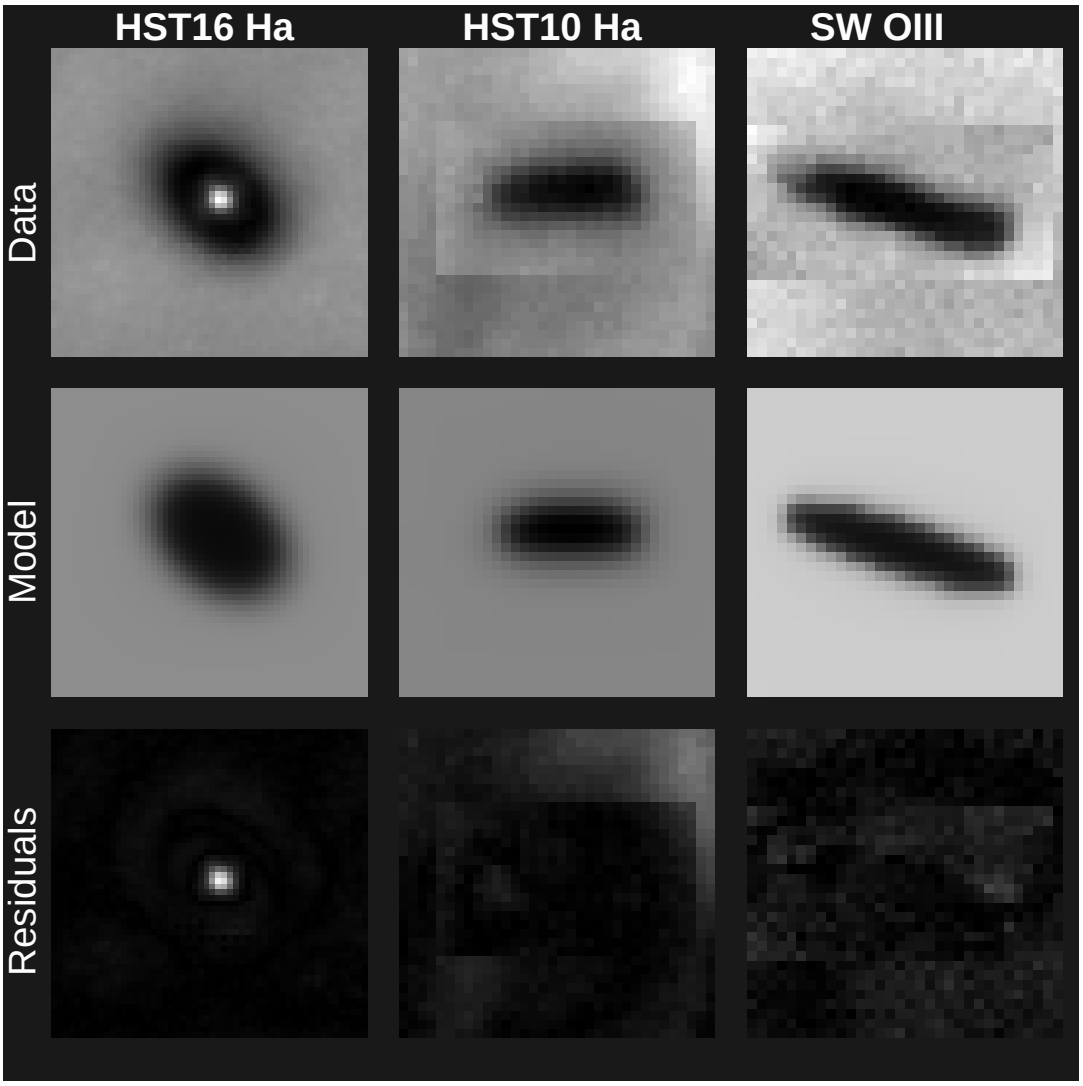

Figure 2.19: Best model fits. Local background flattening causes the box-shaped artifacts.

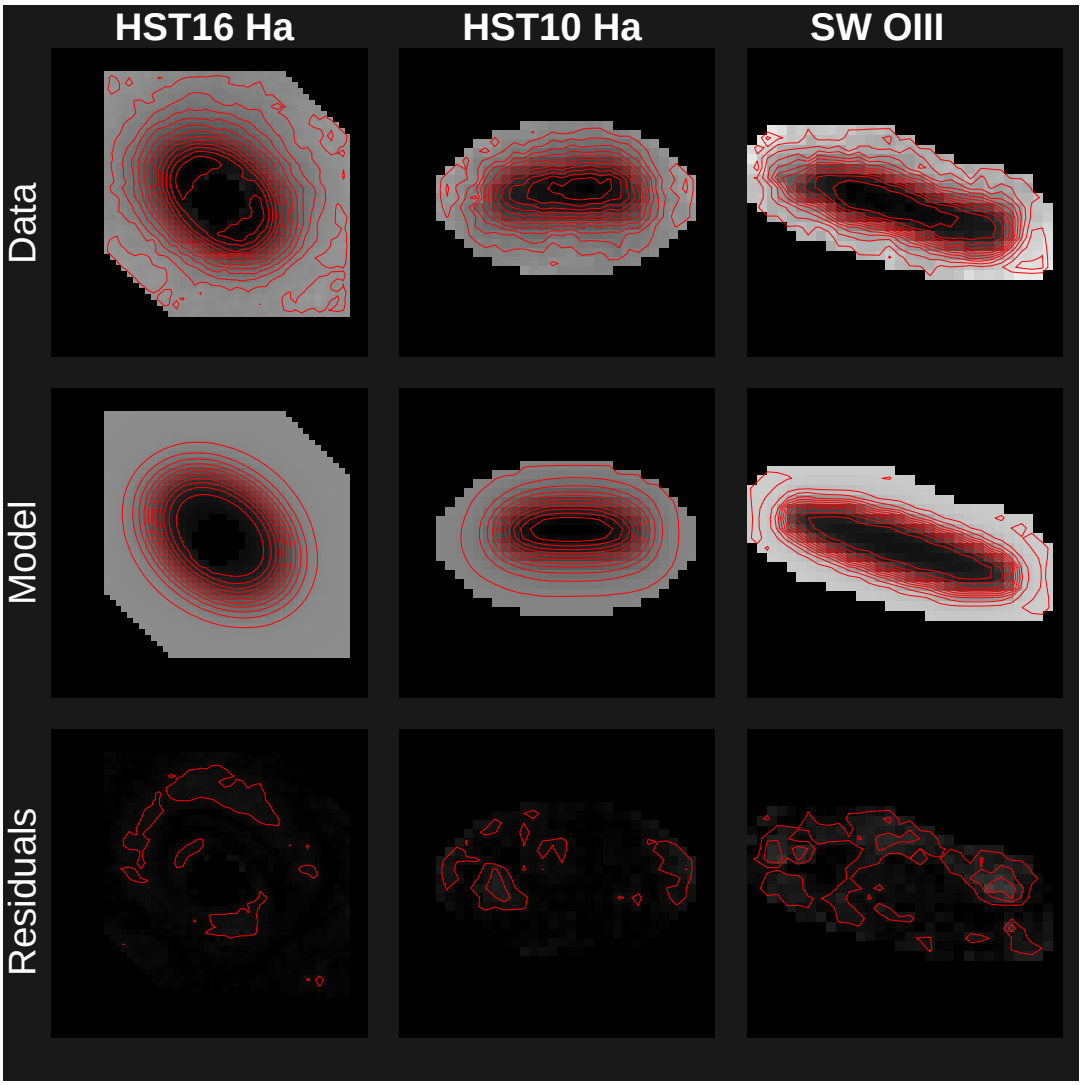

Figure 2.20: Best model fits, with contours.

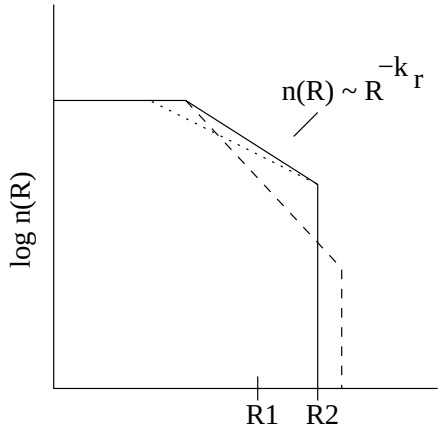

Figure 2.21: Cartoon of disk radial distribution parameters. Relative to the solid line, an increase in k_r can be countered (dashed line) with an increase in R_2 for the observed disk to remain a reasonably good fit. Similarly, a decrease in R_1 can be indistinguishable if it is matched with a decrease in k_r (dotted line).

cases due to weak nebular emission and strong stellar contamination. However, the fit is excellent for the dithered Hα image, and no systematic asymmetries or defects in the fit to the disk can be seen. The only significant residuals are from the slightly non-uniform background. The central star has been masked out well, with only a slight hint of the stellar contribution beyond the mask edges. Fits for the parameter values are shown in Figure 2.22, and an abbreviated summary of the fits in Table 2.4.

Figure 2.22a plots R_1 vs. R_2. There can be seen the somewhat surprising result that neither value is strongly constrained. The lack of constraint on R_1 is easy to understand, because the the face-on optical depth at R_1 ($\tau(R_1) \sim 10^2$) is simply too high to be uniquely measured from the data. The dependence of R_2 can be understood by examining Figure 2.22b, which shows a strong correlation between R_2 and k_r. Relatively large disks can be terminated disks with a steep k_r, while smaller disks with wide 'tails' and a shallow k_r can also fit the data (Figure 2.21). That is, the mass exponent and the outer cutoff cannot be simultaneously uniquely identified from the data. Although a HWHM *can* be uniquely identified (*e.g.*, Section 2.4), it must be stressed this is an *observational* parameter, rather than a *structural* one such as R_2.

Although $\tau(R_1)$ is high and cannot be measured directly, the position of R_1 has the effect of modifying the optical depth distribution throughout the disk, and in particular at the outer edge. This effect can be seen in Figure 2.22c, as a correlation between R_1 and k_τ. Disks with a small inner radius can have much wider, shallower outer edge 'tails' than disks with a large R_1 (c.f. Figure 2.21). The latter must be more sharply terminated.

The correlation between vertical height h and tilt angle θ (Figure 2.22d) is a simple effect of projecting a thick disk onto a plane. Once again, it should be mentioned that simple *observational* parameters such as a width:height ratio can be directly measured from the images; the *structural* parameters constrained here are less well determined but more physically meaningful.

Finally, Figure 2.22e shows the constraint on particle size distribution as correlated with edge-on optical depth $\tau_{\rm max}$. For essentially all disk parameters, the observations are consistent with light scattering by large particles, as suggested by the analysis in Section 2.4. However, for sufficiently high optical depth, the disks *could* also be composed of significantly smaller grains; that is, grains that cannot be distinguished from the ISM. This effect is due to the fact that optically thick regions become increasingly less sensitive to wavelength-dependent extinction effects, because the optical depth becomes increasingly difficult to measure. The difficulty is compounded by the fact that the Orion disk edges are nearly at the spatial resolution limit of HST, and PSF smearing makes unique inversions of the radial profile challenging, as evidenced by Figure 2.22b. Constraining the disk structural parameters more tightly than here requires observations at higher spatial resolution, longer silhouette wavelengths, or fundamentally different methods using different data. In Section 2.6 and Chapter 3, I will examine constraints that can be placed using two additional, orthogonal approaches – in this case, thermal emission and evolutionary modeling.

Plots for the dependences on albedo, foreground emission, and disk position are

not shown here. Albedo shows no noticeable trends with any parameter or with χ^2. This result is somewhat surprising, but examination of Figure 2.16 indicates that transmission is a strong function of albedo only for a narrow range of optical depths. The total flux transmitted through a typical model disk changes by only $0.1 - 1\%$ between $a = 0$ and $a = 0.9$ cases, because most of the disk pixels are dominated by either much higher or much lower optical depths.

Individual plots for foreground emission and disk position are not shown because they are trivial, show strong χ^2 best-fit ranges, and vary with no other parameters. Typical disk position measurements are good to 1/2-pixel or better.

Inferred disk masses based on best-fit parameters are also indicated in Table2.4. It should be kept in mind that these values are not well constrained for the same reason that MO96 were unable to determine the masses. In their case mass limits were based solely on the observed optical depths and were only lower-limits; here, the higher masses are due to inferred higher optical depths than can be actually measured, and of course depend strongly on the form of (2.9). I assumed $\kappa = 10$ cm^2 g^{-1} (for $q = 3$) and $R_{g/d} = 100$.

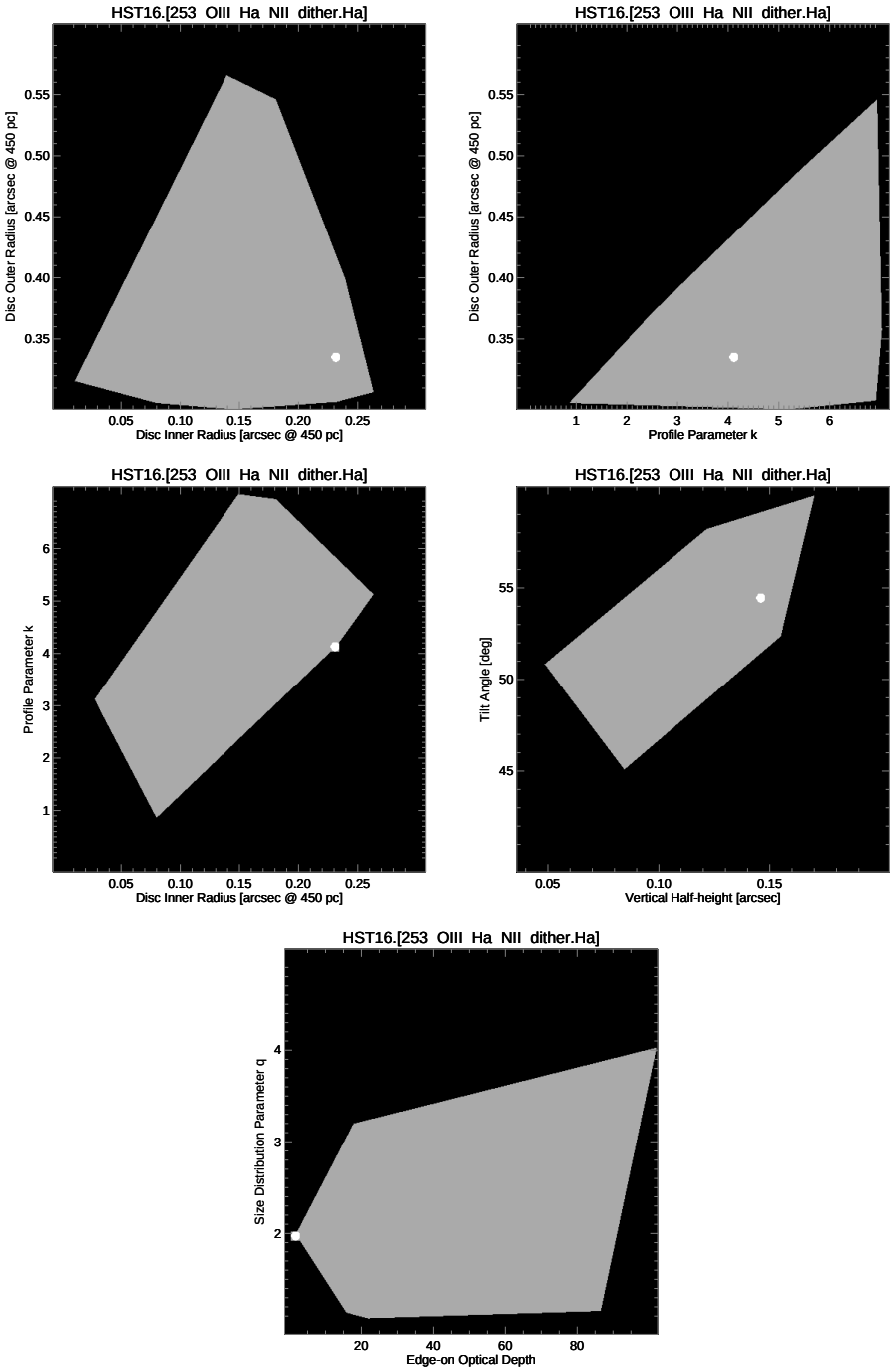

Figure 2.22: HST16 parameter fits. On each plot, the outer boundary encloses the $\chi^2 < 1$ level as per (2.10), and the small circle denotes the single best fit to the data. The hulls enclose ~ 50 data points out of the of the $\sim 100{,}000$ iterations for each disk.

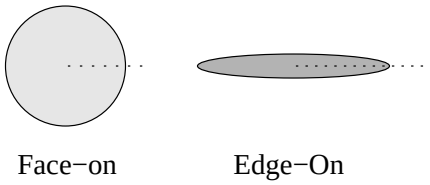

Figure 2.23: Cartoon of optical thickness in face-on vs. edge-on disks. In the former, column density decreases for 'impact parameter' b as b^{-k_r}. In the latter case, column density drops much faster, making determination of R_2 easier but k_r more difficult.

HST10

Fits to the HST10 disk are shown in Figure 2.24. In general, they are similar to those for HST16. Some small asymmetries in the disk can be seen in the dithered Hα images (Figures 2.19–2.20)

Although the HST10 disk covers barely one-quarter the number of pixels as HST16, its outer radial cutoff R_2 is far better constrained (Figure 2.24a). This is an effect of its high inclination angle, with the line-of-sight edge-on rather than face-on; as a result, the projected column density through the midplane increases much faster with 'impact parameter' than for a face-on disk (Figure 2.23). This same effect was noted by McCaughrean *et al.* (1998) in the edge-on SW disk.

As with HST16, the inner radius R_1 is largely unconstrained, but varies again with k_r. The correlation between h and θ is as expected, as is the relationship between q and $\tau_{\rm max}$. However, due to the disk's lower spatial resolution coupled with the artificially steepened behavior of τ from the edge-on tilt, the particle sizes cannot be constrained meaningfully.

Although $\tau_{\rm max}$ cannot be constrained well by the Monte Carlo simulations, the 2.12 μm non-detection of HST10's central star by Chen *et al.* (1998) place a limit $A_{\rm V} > 60$ ($\tau > 55$) for this disk. Their result, however, assumes an extinction coefficient $A_{\rm K}/A_{\rm V} = 10$, which may be true for ISM particles but dramatically overstates the case for larger grains. If one makes the assumption that grains have grown to $r \gtrsim 2\mu$m, the

A_V is not 60, but 6. This constraint, then, is comparable to that from the Monte Carlo results. τ_{max} quite likely is indeed much larger, but the current observations provide no upper limit.

SW Disk

Finally, fits to the SW disk are shown in Figure 2.25. The general trends are similar to those in HST10. However, this disk shows significant asymmetries in several regards: a) the is clearly warped; b) there are two large bulges near the SW ansa of the disk; c) both ansae show extended (10-100 AU), tendrilled asymmetric regions of low optical depth; and d) the central star – visible by reflection – appears to be displaced $\sim 20\%$ from the disk's center. Therefore, the errors due to fitting a clearly asymmetric object with a symmetric model should be kept in mind.

Computational time for computing the 3D models scales as the cube of the number of pixels, and thus the search efficiency at dithered PC resolution is 1/64 that of the WF observations. Therefore, I have for now omitted the otherwise high-quality 0.023" Hα and 814 observations from the analysis.

Best-fit results for the SW disk are broadly similar to the other disks; the longer-wavelength 1.87 μmimage allows somewhat tighter constraints on the fits than the visible wavelengths alone. The disk mass ($9M_\odot$, Table 2.4) estimated is particularly high and probably unreasonably so. This number should be interpreted more as an indication of the difficulty in constraining the true optical depths from the observations, than as a reliable estimate of the actual disk mass.

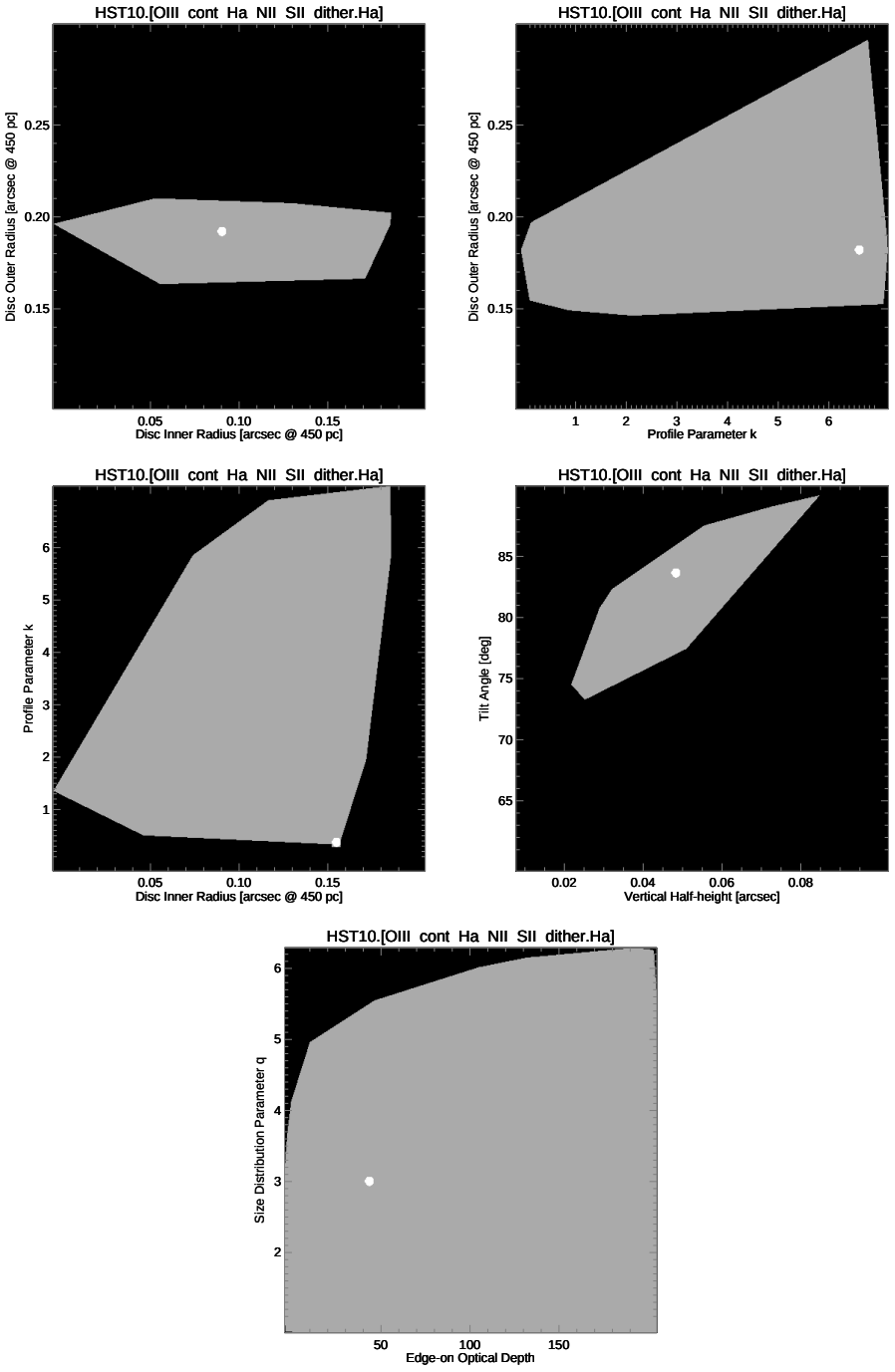

Figure 2.24: HST 10 parameter fits

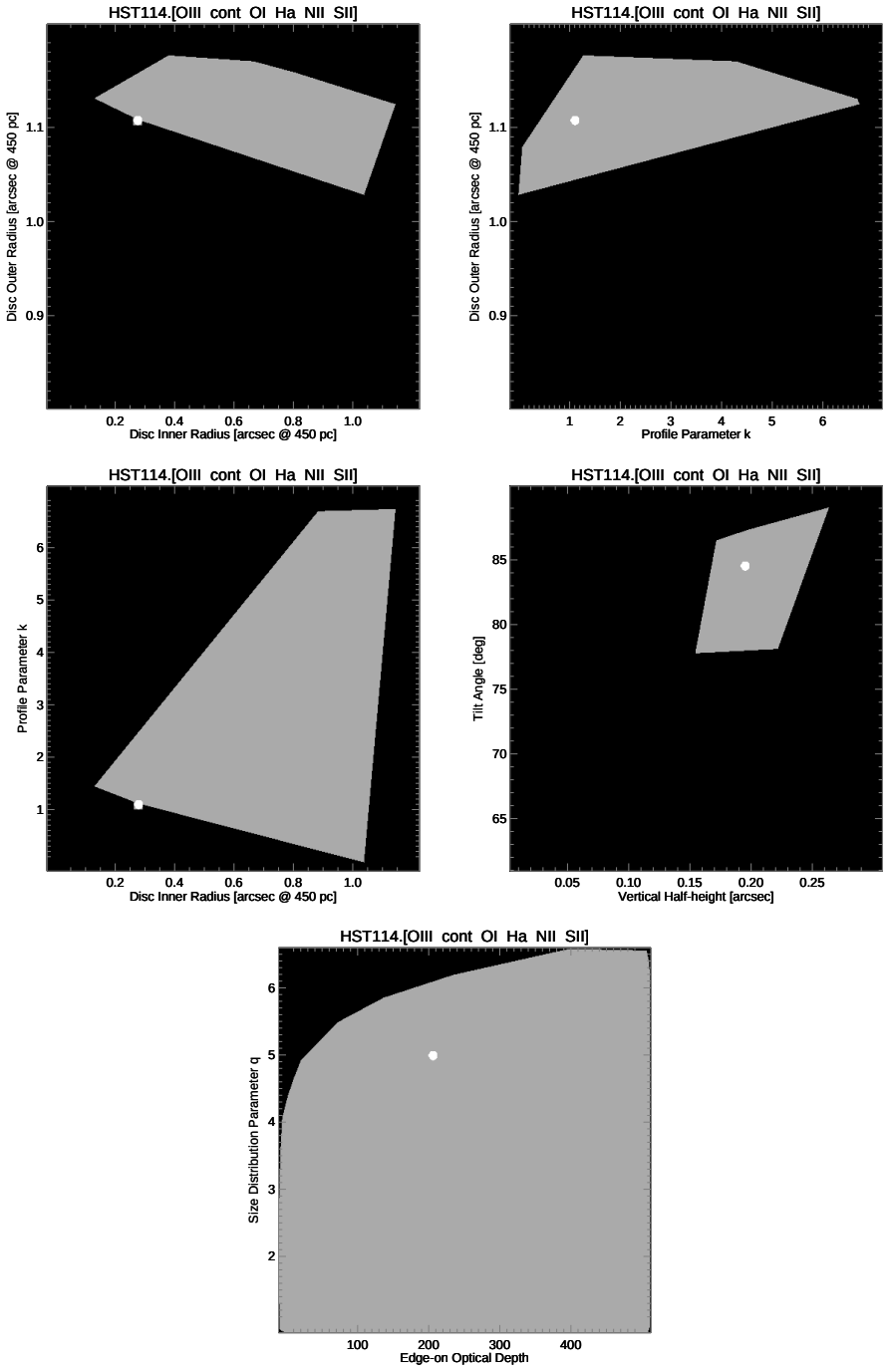

Figure 2.25: SW Disk parameter fits

Table 2.4: Summary of 3D model best-fit parameters. The numerical values given here represent liberal ranges for parameter values, because many parameters are interdependent. Table should be used only as a guide; detailed parameter relationships are shown in Figures 2.22–2.25.

Name	Parameter	HST16	HST10	SW
Inner radius	R_1	56 ± 35 AU	47 ± 33 AU	270 ± 180 AU
Outer radius	R_2	192 ± 55 AU	83 ± 7 AU	495 ± 23 AU
Half-height	z	46 ± 21 AU	24 ± 12 AU	90 ± 23 AU
Mass exponent	k_r	4 ± 3	4 ± 3	4 ± 3
Edge-on optical depth	$\tau_{\rm max}$	> 10	> 3	> 5
Inclination	θ	$50 \pm 10^\circ$	$83 \pm 7^\circ$	$82 \pm 7^\circ$
Foreground emission	E	0.2 ± 0.1	0.3 ± 0.1	0.2 ± 0.1
Particle albedo	a	0.45 ± 0.45	0.45 ± 0.45	0.45 ± 0.45
Particle size exponent	q	< 3.7	< 5.5	< 6
Inferred disk mass	$M_{\rm disk}$	0.16 $M_\odot$	0.1 $M_\odot$	9 $M_\odot$

2.6 Millimeter-wavelength Optical Modeling

During the winter of 1995-1996, Bally *et al.* (1998b) used the Owens Valley Radio Observatory (OVRO) near Big Pine, California to observe two fields in Orion, covering a) the HST10 & HST16 region, and b) the SW Disk region. Both fields were observed at 1.3 mm, in line emission from the rotational ^{13}CO(2−1) and C^{18}O(2−1) transitions and in continuum thermal emission. Although the Orion region has been mapped extensively in the mm-regime, this search was the first high-resolution search in these fields for the proplyds in the radio. The OVRO interferometer, consisting of six 10.4 m dishes over a maximum 400 m baseline, provides a beamsize 1.7" × 2" across the 40" fields.

Bally *et al.* (1998b) reported no detection at the 3σ level of any thermal or line emission from the six known proplyds in the two fields. They used these results to put upper limits on abundances of both gas and dust in the disks, and concluded that $M_{\rm disk} \lesssim 3 \times 10^{-4} - 2 \times 10^{-2} M_\odot$ (Table 2.5). It is worth considering in more detail the analysis they used, in the context of evidence for grain growth in this and the next chapter, and I believe that their mass limits may be substantially too low.

Table 2.5: Revised disk masses, 1.3 mm. Continuum-derived masses of Bally *et al.* (1998b) assume mass opacity of small grains only, and their line-derived masses use CO/H_2 abundances for low-density ISM regions. Both these assumptions cause the disk masses to be underestimated; the actual adjustments are somewhat arbitrary and discussed in the text.

1.3 millimeter-derived Disk Masses

Disc	Mass (continuum)	Mass ($^{13}CO(2-1)$	Reference
HST10, 16	$< 0.015 M_\odot$	$< 3 \times 10^{-4} M_\odot$	Bally *et al.* (1998b)
SW	$< 0.02 M_\odot$	$< 3 \times 10^{-4} M_\odot$	Bally *et al.* (1998b)
HST10, 16	$< 0.15 M_\odot$	$< 0.3 M_\odot$	(current work)
SW	$< 0.2 M_\odot$	$< 0.3 M_\odot$	(current work)

2.6.1 1.3 mm Thermal Emission

Bally *et al.* (1998b) detected no thermal emission from the dust grains, and used this to put a mass limit on the dust. The disk was assumed to be an optically thin region of small particles of total mass $M_{\rm disk}$, radiating at temperature $T_D = 50$ K, with a mass opacity $k_\nu = 2 \times 10^{-2}$ cm^{2}g^{-1}. For a non-resolved source, the total flux F_ν at distance d is

$$F_\nu = B_\nu(T_D)\, k_\nu M_{\rm disk}/d^2 \tag{2.11}$$

and thus

$$M_{\rm disk} = \frac{F_\nu d^2}{B_\nu(T_D)\kappa_\nu} \quad . \tag{2.12}$$

They then calculated that, based on $F_\nu < 21$ mJy and a gas:dust mass ratio $R_{g/d} = 100$, the disk mass $M_{\rm disk} < 0.02 M_\odot$ for the edge-on SW disk.

If the disk were composed of large particles with $x \gtrsim 1$, the value for mass opacity k_ν must be adjusted, because far more mass can be 'hidden' in large particles, where extinction depends on surface area, rather than volume. As per Beckwith & Sargent (1991), we take

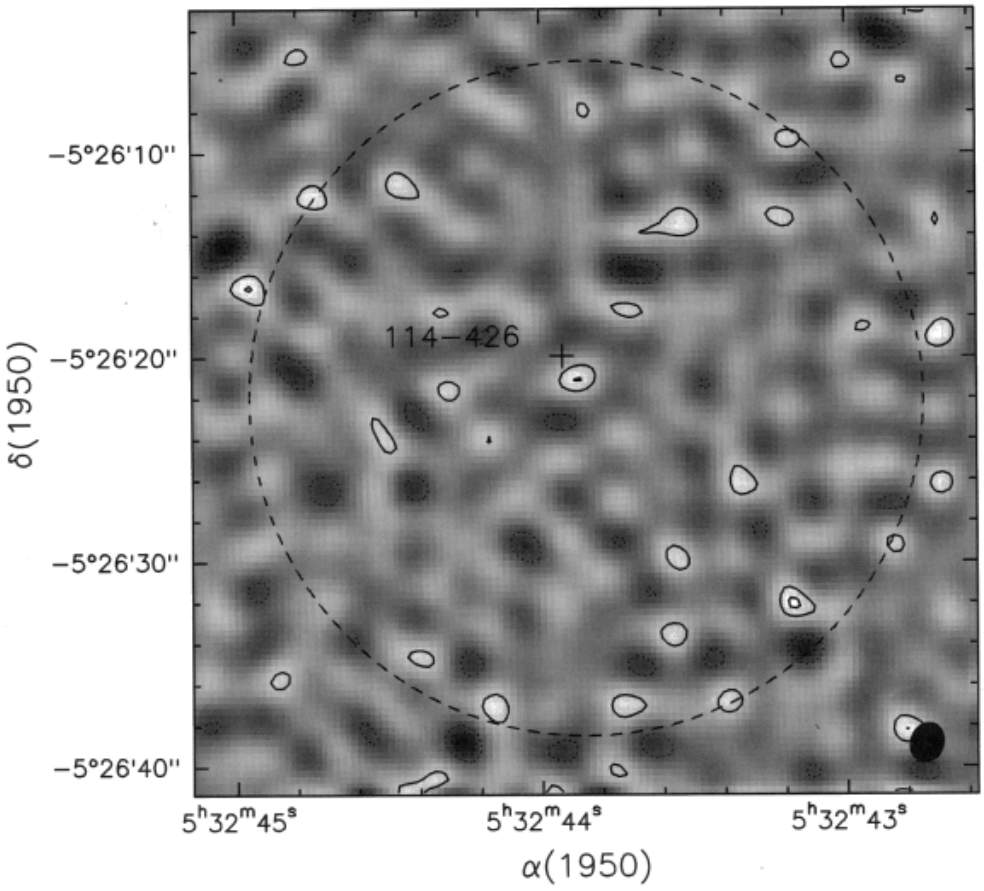

Figure 2.26: One of two 1.3 mm continuum fields observed with OVRO by Bally *et al.* (1998b). This map is centered on the SW disk (marked); neither field showed any significant emission. Brightest contours are 21 mJy. Reproduced from Bally *et al.* (1998b).

$$k_\nu = \frac{3}{4r\rho_s} Q_{\rm abs} \ . \tag{2.13}$$

In the large particle limit for moderately absorbing particles,

$$Q_{\rm abs} \approx 1 \qquad \text{for } x \gtrsim 10 \tag{2.14}$$

and thus the disk mass is underestimated, by roughly a factor of r/λ. Estimates for r can be taken from the observation results in this chapter or the modeling in Chapter 3; for the sake of comparison, I take $r = 10\lambda \sim 1$ cm, a typical value predicted in Chapter 3. For this case, it is clear that the upper mass limits of Bally *et al.* (1998b) are significantly low.

2.6.2 1.3 mm Line Emission

A similar analysis can be applied to the Bally *et al.* (1998b) non-detection of 1.3 mm line emission from the disks. In this case, they use an assumed H_2:^{13}CO abundance ratio $X_{13} = N(H_2)/N(^{13}CO) = 7 \times 10^5$, and imply a disk mass limit

$$M_{\rm disk} < 3 \times 10^{-4} \frac{X_{13}}{7 \times 10^5} M_\odot \ . \tag{2.15}$$

This calculation is based on an assumption that the disk is optically thin; that is, all flux radiated by the dust leaves the disk. This assumption can be checked by calculating the optical depth from first principles. The disk can be approximated by a flat 'pancake' of radius R and height $R/10$, populated by a unimodal distribution of particles of size r. These particles extinct radiation with an efficiency

$$Q_{\rm ext} = Q_{\rm abs} + Q_{\rm sca} \approx Q_{\rm abs} \tag{2.16}$$

$$\approx 4x \, {\rm Im} \left\{ \frac{m^2 - 1}{m^2 + 2} \right\} \qquad \text{for } x = \frac{2\pi a}{\lambda} \lesssim 1 \tag{2.17}$$

The edge-on optical depth can then be calculated, assuming $m \approx 2 + 0.02i$ for a silicate-ice mixture (Warren 1984; Philipp 1985):

$$\begin{aligned} \tau_\nu &= N\,\pi r^2\,Q_{\rm abs} \\ &= \frac{M_{\rm disk}}{\frac{4}{3}\pi r^3 \rho_s}\,\frac{R}{\frac{\pi R^3}{10}}\,\pi r^2\,\frac{8\pi r}{\lambda}{\rm Im}\left\{\frac{m^2-1}{m^2+2}\right\} \\ &\approx \frac{0.6\,M_{\rm disk}}{R^2 \lambda \rho_s\,R_{\rm g/d}}\quad . \end{aligned} \tag{2.18}$$

For typical intermediate-scale disk parameters ($R = 40$ AU, $M_{\rm disk} = 0.1 M_\odot$, $\rho_s = 1$), the $\lambda = 1.3$ mm optical depth is $\tau_\nu = 25$. Thus, even for small particles, the disk is significantly optically thick. I note the interesting result that the optical depth is independent of particle size and only dependent on the total particle mass; therefore, this result holds for even an evolved disk where particles have grown to sizes $r \sim \lambda$. In the *thermal* emission case, the optical thickness may have a minimal effect, because any radiation absorbed by dust is immediately re-radiated at the same wavelength; however, in the *line emission* case, flux is reduced by $f \sim \exp -\tau_\nu$, potentially affecting the result significantly. It should be noted that (2.18) assumes an unrealistic unimodal size distribution, and in reality secondary products of collisions between large particles may leave a high-τ, low mass dusty envelope throughout the disk, similar to debris disks or planetary rings. Therefore, (2.18) may substantially underestimate the true optical depth of a realistic collisional disk, and thus further contribute to an underestimate of the disk mass.

Furthermore, numerical modeling of molecular abundances in large protoplanetary disks suggests that CO may rapidly condense onto grains, making it a poor tracer of H_2 abundance. For instance, work by Aikawa *et al.* (1997) found that, at $a = 87$ AU and $T = 30K$, CO level relative to H_2 has dropped by $f > 10^6$ at $t = 10^6$ yr. Recent observational work by Shuping (2000) partially supports this result; his work observed a depletion fraction $f > 20$ of CO in cold regions. Therefore, the value of X_{13} adopted

by Bally *et al.* (1998b) may be inappropriately high for non-ISM regions, in both the optically-thin and -thick cases – perhaps to the extent that CO simply cannot be used as a viable tracer. The mass limits in (2.15) should therefore be revised upwards by a factor f; for the point of comparison I take $f = 10^3$, but this choice is quite arbitrary in either direction.

2.7 Discussion

In this chapter, a variety of observations at different wavelengths have been used to constrain fundamental properties of the disks: their size, structure, and particle composition. Most disk properties cannot be uniquely determined; however, relationships between various parameters can be observed and the conclusions make physical sense.

There is suggestive evidence on three grounds that particles in the disks are large. First, the *disk radial profiles are observed to be achromatic*, with no selective extinction seen through the disks' outer edges. Second, un-biased multi-parameter 3D structural *fits to the visible observations are consistent with large particles*, but do not require them. Finally, the *disks emit no measurable continuum emission*, a result that is difficult to understand without a mass opacity coefficient appropriate for large particles. The combination of these three analysis methods is compelling evidence for – if not proof of – disks which are dominated by large particles.

The first two methods are limited by the spatial resolution. Higher spatial resolution is necessary to unveil the disks' true structure from behind the curtain of PSF smearing. In the current data set, the disk edges are of comparable size to the PSF, and simply cannot always be uniquely inverted to yield the radial profile. Higher spatial resolution could come with observations at shorter wavelengths (the FOC observations are unfortunately severely underexposed), with observations of closer disks (possible in closer, smaller OB associations such as Sco-Cen), or with larger apertures. It is possible that either ground-based adaptive optics systems or sub-mm/optical interferometry

could yield significant insight into the disk radial structure.

However, higher optical spatial resolution will still allow imaging only of the outer, $\tau < 1$ disk edges, and radial structure inward of this will remain largely unconstrained. Observations at longer wavelengths probe for larger particles, and may be able to solidly constrain the particle sizes. Infrared observations *can* be difficult to interpret, however, as the disks and central stars begin to radiate thermally, and of course the lower diffraction-limited spatial resolution can be an additional problem. For instance, initial estimates for 10 μm observations of the disks from the 2.3 m WIRO observatory indicated that largest SW disk would be difficult detect above thermal emission from the central, IR-excess star. The best hopes for IR observations lie in the edge-on disks which shield their central stars.

The lack of detection in the millimeter wavelength observation was initially surprising, but in retrospect can be easily explained by an evolving disk with gas and dust properties that – naturally – are not well approximated by those of the ISM.

Longer integrations, bigger telescopes, and higher spatial resolutions can all be of great benefit. However, perhaps a more effective approach is to constrain the disk properties from the opposite direction: given a set of initial conditions and physical processes, what would the current proplyds be *expected* to look like? In Chapter 3, I examine the disks from this approach.

Chapter 3

Numerical Evolution Models of Protoplanetary Disks

Before this could be done, however, a violent storm arose and the surging within the enclosure caused by wave action made it impossible to hold firmly in place with mooring lines. It battered the steelwork and concrete with such force that the contractor secured permission to remove the cassion at once and abandon that part of the construction plan.

Final Report of the Chief Engineer
Golden Gate Bridge Project, September 30, 1937

3.1 Introduction

The circumstellar disks in Orion are fascinating objects in their present state. They make up one of the few collections of young disks orbiting nearby that are seen in a variety of sizes, shapes, and environments, and their existence can tell us much about the stellar and planetary formation process.

What is perhaps even more fascinating is what we cannot see directly. Since their discovery, the Orion objects have been proposed to be harboring planetary formation; indeed, the name 'proplyd' used to describe the objects refers to the PROtoPLanetarY Disks scattered throughout the nebula. In Orion, we have the opportunity to literally watch the planetary formation process happen before our eyes. Will some of these disks form planets? Have they already? What might these systems look like? Or, will planets be torn apart in the violent stellar nursery that is the Orion nebula, victims of harsh UV radiation and stellar winds? Could our own solar system have formed in a region like Orion – or has our Sun been brought up in a cooler, calmer environment?

The existence of our solar system has been observationally justified for some time

(*e.g.* Galilei 1610). However, it is always satisfying to justify its existence on the solid grounds of theory, and no small number of studies have attempted to do exactly that. These results form a basis for our study of planetary formation in the Orion nebula.

To evolve from the presently-observed Orion clouds of dust into a small swarm of planets, the small primordial dust grains must collide and stick together. Unlike disks in the solar system such as planetary rings or the asteroid belt, the dynamics of particles in young circumstellar disks are dominated not by keplerian particle orbits, but by the gas dynamics transporting entrained small particles. The transition size between these two regimes occurs roughly where the particle's frictional stopping time and the keplerian time are equal; *i.e.*, $\tau_f \Omega < 1$. An even larger size scale come in when particles begin to gravitationally interact not only with the central star, but with each other. Particle growth in the keplerian and gravitational regimes has been modeled by many studies.

The Orion disks studied here are unique in the context of protoplanetary disks studied to date because of the external illumination from young O stars, which significantly affects the disk dynamics. No previous models have examined grain growth in a photoevaporative environment. In this chapter, I will first summarize the previous work, and then describe a numerical model of grain growth in a photoevaporating protoplanetary disk.

3.1.1 Previous models

Solar nebula evolution & coagulation models

Several models of the early evolution of the post-collapse solar nebula have been created in the past. The existence of turbulence fundamentally distinguishes these models from laminar situations dominated by particle-in-a-box Keplerian velocities. The turbulence is sustained by a convective heat flux escaping the disk midplane: viscous energy production and the heat of collapse drives the instability, which in turn provides

the convection and usually turbulent viscosity (*e.g.* Lin & Papaloizou 1980; Lin & Bodenheimer 1982; Mizuno *et al.* 1988; Ruden & Pollack 1991; Hawley *et al.* 1999). As long as thermal opacity is maintained, the disk remains turbulent. The largest grains decouple from the gas, but for the earliest stages, grain dynamics are dominated by gas dynamics.

Voelk *et al.* (1980) describe the turbulent properties of the disk in terms of a series of cascading eddies with a Kolmogorov velocity spectrum. Mizuno *et al.* (1988) extended their work and applied it to a numerical model of grain coagulation in the early solar nebula. Within each eddy, grains of particular sizes are selected; the characteristic time of a particle is defined by its frictional time τ_f. Grains are preferentially picked up into eddies of turnover time comparable to their friction time. They then calculate the RMS grain-grain collision velocities as a function of the frictional times of two particles.

Grain growth or coagulation[†] can be described by the coagulation equation

$$\frac{\partial}{\partial t} n(m,t) = -\int_0^\infty (\sigma v_{m,m'})\, n(m,t) n(m',t)\, dm' + \frac{1}{2}\int_0^m (\sigma v)_{m-m',m'} n(m-m',t) n(m',t)\, dm' + \varphi(m) \qquad (3.1)$$

between particles of mass m and m'. $n(m,t)$ represents the particle number distribution, $\sigma = \pi(r+r')^2$ the collision cross section, and $v_{m,m'}$ the collision velocity. φ represents additional, non-coagulation terms such as mass loss or mass input. This expression can be numerically integrated to give the grain size distribution at any point in time t.

Starting with an ISM-like power law distribution of sub-micron dust, Mizuno *et al.* (1988) integrate (3.1) and find the peak size to grow to $r = 1$ mm after $t \sim 1000$ yr. As grains grow, the opacity drops proportionally; their model switches off convection when the thermal opacity drops below 10^{-2} cm^2 g^{-1}, based on Mie cross-sections of the particles.

[†] 'Accretion' is used for several other astrophysical processes.

Weidenschilling (1977, 1997) has developed a similar grain growth model using slightly different physics. In contrast to the Mizuno *et al.* model, which considered only turbulent coagulation and particles in the μm-cm range, the Weidenschilling (1997) model calculates particle growth up to km-sized planetesimals, using thermal motion, radial drift, vertical settling, and gravitational interactions. The model is thus valid for longer timescales, up to 3×10^5 yr.

In the Weidenschilling model, a state vector tracks $n(r, t, z)$ at $R = 30$ AU. The smallest particles are assumed to be in thermal equilibrium, and grow by thermal motion given by

$$v_{\rm th} \equiv \sqrt{\frac{3kT}{m}} \quad . \tag{3.2}$$

Turbulence is ignored. After particles grow beyond $r \sim 1$ cm, grains begin to settle vertically and drift radially, both due to differential shear between the keplerian and pressure-supported gas velocities. The radial drift is significant for a narrow range of sizes, reaching $v_{\rm r} \sim 10^3$ cm s^{-1} for meter-sized bodies. Below this size, particles are coupled to the gas; above it, they are decoupled. In contrast to the earlier models, Weidenschilling considers the aerodynamic properties of aggregate, fractal grains. For the largest km-sized particles, runaway gravitational growth becomes the dominant process.

The timescales for growth to cm-sized particles are roughly an order of magnitude longer than those presented by Mizuno *et al.* (1988). This is apparently because typical thermal collision velocities (Weidenschilling 1997) are lower than typical turbulent collisional velocities (Mizuno *et al.* 1988); The Weidenschilling model explicitly ignores turbulence because its effect on large-particle collision rates is negligible.

The models of Stepinski & Valageas (1996, 1997) consider similar processes as Weidenschilling, but extend the model over a range of R for both high-mass (0.24

$M_\odot$, 15 AU) and low-mass (0.02 $M_\odot$, 250 AU) disk models. Neither thermal motions nor gravity are included. To decrease the problem's dimensionality, two significant simplifications are made: a) the particle size distribution at each location is tracked only as a characteristic particle size, and b) the vertical profile is defined only by a characteristic height. Stepinski & Valageas (1997) define the initial surface density to be

$$\Sigma_0(r, t_0) = 8540 \left[1 + \frac{R}{15 \text{ AU}}^2\right]^{-3.78} \text{ g cm}^{-2} \qquad \text{high-mass disk (3.3)}$$

$$\Sigma_0(r, t_0) = 2 \left[1 + \frac{R}{200 \text{ AU}}^2\right]^{-3.78} + 600 \left[\frac{R}{1 \text{ AU}}\right]^{-1.5} \text{ g cm}^{-2} \qquad \text{low-mass disk} \quad (3.4)$$

using grains of $r = 10^{-3}$ cm and $M_{\text{gas}}/M_{\text{dust}} = 100$.

For the high-mass models they find the intriguing result that rapid radial drift ($v_r \sim 10^4$ cm s^{-1}) causes *all* solids in the disk to be accreted onto the star. The low-mass disk produces final mass distributions that closely match our own solar system. At 30 AU, the growth timescales they calculate are roughly similar to those of Weidenschilling.

Photoevaporation models

To the extent that the Orion disks are rough analogues to the early state of our own solar system, the solar nebula models can be applied to the Orion disks. However, several studies have indicated that the external environment of Orion may significantly affect the disks' evolutionary histories (*e.g.* Johnstone *et al.* 1998; Stoerzer & Hollenbach 1999). Therefore, any nebula evolution models must be substantially modified before being applied to the Orion disks.

The Trapezium stars, dominated by 06p $10^5 L_\odot$ star θ^1 Ori C, are the source of bright EUV (ionizing; $h\nu >$ 13.6 eV <) and FUV (non-ionizing; 6 eV $< h\nu <$ 13.6 eV) radiation into the Orion nebula. Ionizing radiation excites atomic hydrogen

and lights the entire nebular region, illuminating the disks in silhouette. This same light source, however, may be responsible for the eventual destruction of many of the disks and the return of their components to the nebula. The Trapezium is the source of 10^{49} photons s^{-1} of Lyman continuum radiation with $\lambda < 912$Å. Additionally, softer FUV radiation of 912 Å$< \lambda <$ 2000 Åfloods the nebula with a radiation field of $\sim 10^4 - 10^6$ G_0 at typical disk distances, where $G_0 = 1.6\ 10^{-3}$ erg cm^{-2} s^{-1} is a mean interstellar FUV flux near the Sun.

According to the models of Stoerzer & Hollenbach (1999) and Johnstone *et al.* (1998), in many regions of Orion, FUV radiation causes a process of 'photoevaporation' to rapidly destroy the disks by heating their gas component to larger than the escape velocity. Gas leaves the disks in a warm outflow, and it is this gas envelope (denoted with the mildly confusing term "proplyd", for PROtoPLanetarY Disk) which can be seen surrounding $\sim$ half of the Orion dark disks (Bally *et al.* 1998a). Photoevaporation destroys the disks at rates of $10^{-6} - 10^{-8} M_\odot$ yr^{-1}, yielding disk lifetimes on the order $10^4 - 10^6$ years. Although dark disks are not directly seen at the center of every one of the $\sim$ 150 proplyds, many disks may be obscured or simply too small to resolve with current instruments.

The photoevaporation model proposes that disks are destroyed by the following process (Stoerzer & Hollenbach 1999) (Figure 3.1): First, FUV radiation passes through the ISM and through the proplyd envelope until being absorbed by dust grains in disk's outer optical depth. This occurs mostly in the $\tau_{\rm dust} < 1$ layer at the disk surface. For normal ISM grains this corresponds to $N(H) \sim 10^{21}$ cm^{-2}. Photoelectrons are then ejected from the grains into the disk, and warm the gas to 10^{2-3} K. At this temperature the majority of the disk gas – predominantly neutral atomic H – is no longer gravitationally bound and leaves the disk by Jeans escape. The flow expands outward at several times the sound speed, passes through a decelerating shock front, and reaches an ionization front (IF) where it is ionized by EUV photons. This IF is

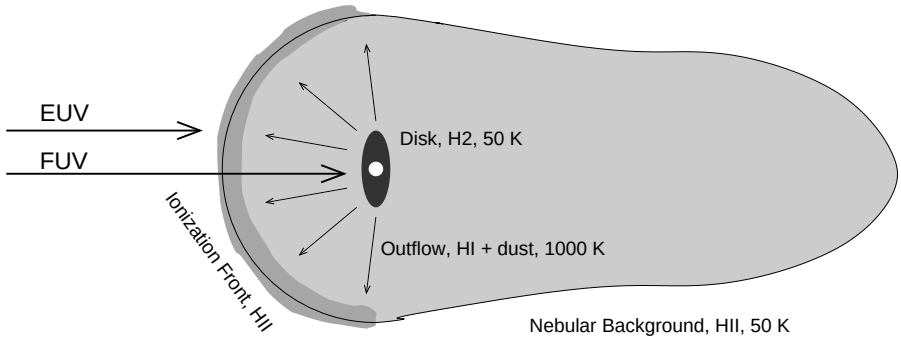

Figure 3.1: Cartoon of the photoevaporation process in the Orion Nebula.

clearly visible as the brightest region of the proplyds, pointing directly toward θ^1 Ori C. A balance keeps the IF from expanding outward indefinitely; however, some outflow material is blown backward around the proplyds in cometary-resembling tails.

To model the system, Stoerzer & Hollenbach (1999) simplify the 'disk' to be a sphere of radius R. The outflow expands spherically out to the IF, several disk diameters away, with a envelope column density of

$$N_D = n_0 R \tag{3.5}$$

which supports a total mass loss rate from the disk

$$\dot{M} = 4\pi R^2 v_0 n_0 m_H, \tag{3.6}$$

assuming number density n_0 at the disk surface and outflow velocity v_0. N_D, the depth of FUV penetration, corresponds to an atomic H column density $\tau_{\rm FUV} \sim 1 - 3$. Thus,

$$\dot{M} = 1.3 \times 10^{-8} \frac{R}{10^{14}\ {\rm cm}} \frac{N_D}{10^{21}\ {\rm cm}^{-2}}\ M_\odot\ {\rm yr}^{-1}\ . \qquad {\rm FUV-dominated mass loss rate} \tag{3.7}$$

The FUV photoevaporation process describes the physics for the majority of the proplyds. However, objects particularly close to or extremely far from the UV source

($d < 0.01$ pc; $d > 0.3$ pc), or small disks ($R < 20$ AU) are dominated not by FUV but by EUV flux: close to the UV source, EUV flux is high enough to penetrate to the disk surface, and far from the source, FUV heating is too low to maintain the ionization front. The theory described in more detail in Johnstone *et al.* (1998), and are characterized by an ionized (rather than neutral) outflow. In the EUV-dominated case it can be shown that (omitting several constants of order unity)

$$\dot{M} = 9.5 \times 10^{-9} \left[\frac{R}{10^{14} \text{ cm}} \right]^{3/2} M_\odot \text{ yr}^{-1} \qquad \text{EUV} - \text{dominated mass loss rate} \quad (3.8)$$

For the FUV case in particular, the mass loss rate depends on the disk size, but is surprisingly *independent of distance* from the UV source, due to the self-regulating nature of the IF. For a 'minimum mass solar nebula' disk of $R = 40$ AU and $M_{\text{disk}} = 0.01 M_\odot$, $\dot{M} \sim 10^{-7} M_\odot$ yr^{-1}, and the timescale for loss of the entire disk is $\sim 10^5$ yr.

Johnstone *et al.* (1998) apply the photoevaporation rates to a simple analytical model of disk evolution, where a disk is eroded from the outside inward under photoevaporation. Their model takes a flat disk with a power law surface density exponent k_r,

$$\Sigma(R) = \Sigma_0 \left(\frac{R}{R_0} \right)^{-k_r} \quad (3.9)$$

and integrates it under (3.7) and (3.8). They find for $k_r = 3/2$, the presently-observed disks (*e.g.*, HST10) are consistent with disks of original mass and radius 10 and 100 times their present values (assuming an ionization age $\sim 10^5$ yr), and predict that these disks will be ultimately lost to the central stars by viscous accretion. They note that k_r would naturally increase at the outer edge, but don't make explicit calculations.

The EUV flux from a disk's own central star is *not* considered here. Several modelers (Shu *et al.* 1993; Hollenbach *et al.* 1994) have investigated the effects of EUV radiation in ionizing and destroying the disk from the inside out. Although the mass

loss rate is much lower ($\dot{M} \sim 10^{-9} - 10^{-10}\, M_{\odot}$ yr^{-1}), over the lifetime of a low mass star and a long-lived disk, significant disk loss could eventually be accounted for by flux from the central star.

A number objects in the Orion HII region (*e.g.*114-426) are not observed to have any ionization front or photoevaporation. It is quite likely (Johnstone *et al.* 1998) that these objects either lie far enough away to have no visible ionization, or are simply outside the Trapezium's "Strömgren sphere" of ionized hydrogen (Wen & O'Dell 1995). Projected distances can be deceiving!

3.2 Physical Processes in a Numerical Model

No protoplanetary disk evolution models to date have considered grain growth within a photoevaporative environment. The relevance of this situation has been justified in Chapter 1: the majority of solar-type stars appear to form in regions like Orion, so the effect of external illumination *must* be considered in nebula evolution models which form large grains and eventually planets.

Many successful models have explained the formation of the solar system in the gravitational regime, starting with km-sized planetesimals. Furthermore, models which explain the creation of these planetesimals from cm-sized particles are also successful, and fully applicable in a photoevaporating environment (eg Weidenschilling 1997). However, models which follow the very initial stages of grain growth, from μm to cm-sized particles, must be substantially modified in an externally illuminated environment. It is this regime of particle growth that I model.

Rather than re-inventing from first principals, the approach taken has been to develop a numerical model which takes 'best guess' parameterized inputs from a variety of sources for a variety of physical processes. For instance, the particular details of the turbulence are not modeled; rather, the parameterized velocity equations from a prior model are used. In this way, the model is computationally simplified and easy to adjust

for a variety of initial conditions and physical processes.

3.2.1 Coagulation in a turbulent, convective medium

The model of Mizuno *et al.* (1988) is used for the intergrain collision velocities. Various quantities in the disk can be defined (Figure 3.3):

$$u_s = Re^{-1/4} u_0 \qquad \text{velocity of smallest eddy} \tag{3.10}$$

$$u_0 = c_s/10 \qquad \text{velocity of largest eddy} \tag{3.11}$$

$$\tau_s = Re^{-1/2} \tau_0 \qquad \text{turnover time of smallest eddy} \tag{3.12}$$

$$\tau_0 = h/c_s \qquad \text{turnover time of largest eddy} \tag{3.13}$$

$$Re = \alpha c_s h/\nu \qquad \text{Reynolds number} \tag{3.14}$$

$$c_s = \sqrt{1.4kT/m_{\mathrm{H}_2}} \qquad \text{sound speed} \tag{3.15}$$

$$\rho_g = \Sigma/h \qquad \text{gas density} \tag{3.16}$$

$$\nu = \frac{c_s\, m_{\mathrm{H}_2}}{2\,\sigma_{\mathrm{H}_2}\,\rho_g} \qquad \text{molecular viscosity} \tag{3.17}$$

$$\tau_f = \frac{3}{2}\frac{\sqrt{\pi}\, r \rho_s}{\rho_g c_s} \qquad \text{particle friction time} \tag{3.18}$$

$$T(R) = 50 \text{ K} \left(\frac{\mathrm{R}}{40 \text{ AU}}\right)^{-3/4} \qquad \text{Temperature structure, } R < 40 \text{ AU} \tag{3.19}$$

$$T(R) = 50 \text{ K} \qquad \text{Temperature structure, } R > 40 \text{ AU} \tag{3.20}$$

$$h(R) = 1.7\text{AU} \left(\frac{\mathrm{R}}{40 \text{ AU}}\right)^{3/4} \qquad \text{vertical half-height} \tag{3.21}$$

$$\Sigma(R) = 2.2 \times 10^{-12} \text{g cm}^{-2} \left(\frac{R}{40 \text{ AU}}\right)^{k_r} \qquad \text{surface density} \tag{3.22}$$

using disk vertical thickness h and viscosity parameter α. The particle friction time is calculated assuming the Epstein regime, valid for particles of $r \lesssim 1$ m (Cuzzi *et al.* 1993). These parameters are similar to those used by Mizuno *et al.* (1988) and Weidenschilling (1997). For a disk extending between $R_1 = 10$ AU and $R_2 = 500$ AU, and taking $k_r = 2$, the nominal disk mass is $M_{\mathrm{disk}} = 0.1 M_\odot$. M_{star} is taken to be $M_\odot$, and α is taken to

be 10^{-2}.

Mizuno *et al.* (1988) then derive the particle collision velocity for the case $\tau_f < \tau_s$:

$$v_{12} = \frac{u_s}{\tau_s}|\tau_{f_1} - \tau_{f_2}|\sqrt{\frac{1}{2}\frac{\ln Re}{Re^{1/2}}\frac{\tau_0}{\tau_{f_1}+\tau_{f_2}}} \quad . \qquad \text{turbulent collision velocity} \tag{3.23}$$

For $\tau_f > \tau_s$ regime, the collision velocity is somewhat more complex than (3.23) and the detailed relationships are given in Voelk *et al.* (1980), and plotted in Figure 3.2. At $R = 40$ AU, Mizuno *et al.* (1988) assume values of $T = 10$ K, $\alpha = 1/3$, $\rho_g = 2.2 \times 10^{-12}$ g cm^{-3}, $h = 1.6$ AU, and sticking coefficient $\epsilon = 1$.

They then use (3.23) to numerically calculate the evolution of a grain size distribution, starting from a power law size distribution $n(r)\,dr = r^{-q}\,dr$ of sub-micron grains at $q = 3.5$. In the Mizuno *et al.* (1988) model all particles are assumed to be small enough to couple to the gas; typically this is valid for particles up to cm-sizes, as discussed in Section 3.2.4.

Convection is maintained only when heat cannot directly radiate from the midplane out of the disk; *i.e.*, the vertical temperature profile exceeds the adiabatic lapse rate $\Gamma = c_p/g$. This appears to be a condition readily satisfied in many large, viscous disks (*e.g.* Lin & Papaloizou 1980; Stepinski & Valageas 1997; Mizuno *et al.* 1988). Following the model of Mizuno *et al.* (1988), we turn convection entirely on or off when the thermal optical depth $\tau_t(R) > 1$ or $\tau_t(R) < 1$. Because the Orion HII region is relatively warm ($T \sim 10 - 30K$ *e.g.* Stoerzer & Hollenbach 1998a), convection *might* be inhibited at the cool outer edges under some conditions; the detailed thermal and convective structure of disks in a warm environment requires more study.

Given these input parameters, calculating the Mizuno *et al.* collision velocities is straightforward, using 3.23 and the tabulated results in Voelk *et al.* (1980).

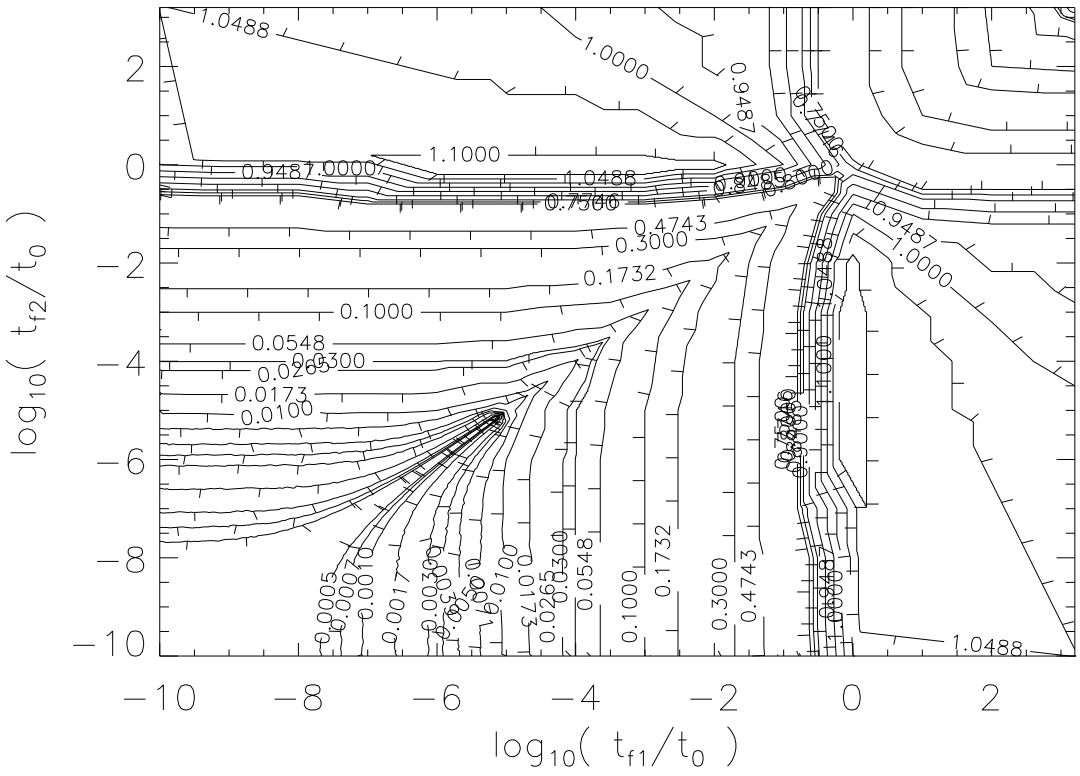

Figure 3.2: Grain-grain collision velocities from the model of Mizuno *et al.* (1988). Grains of similar size are trapped in eddied with similar velocities, so have comparably low collision velocities compared with different-sized particles. The model here is an extension of the Voelk *et al.* (1980) model, and is based on a Kolmogorov velocity spectrum with hard cutoffs at the smallest and largest eddy sizes, λ_s and λ_0.

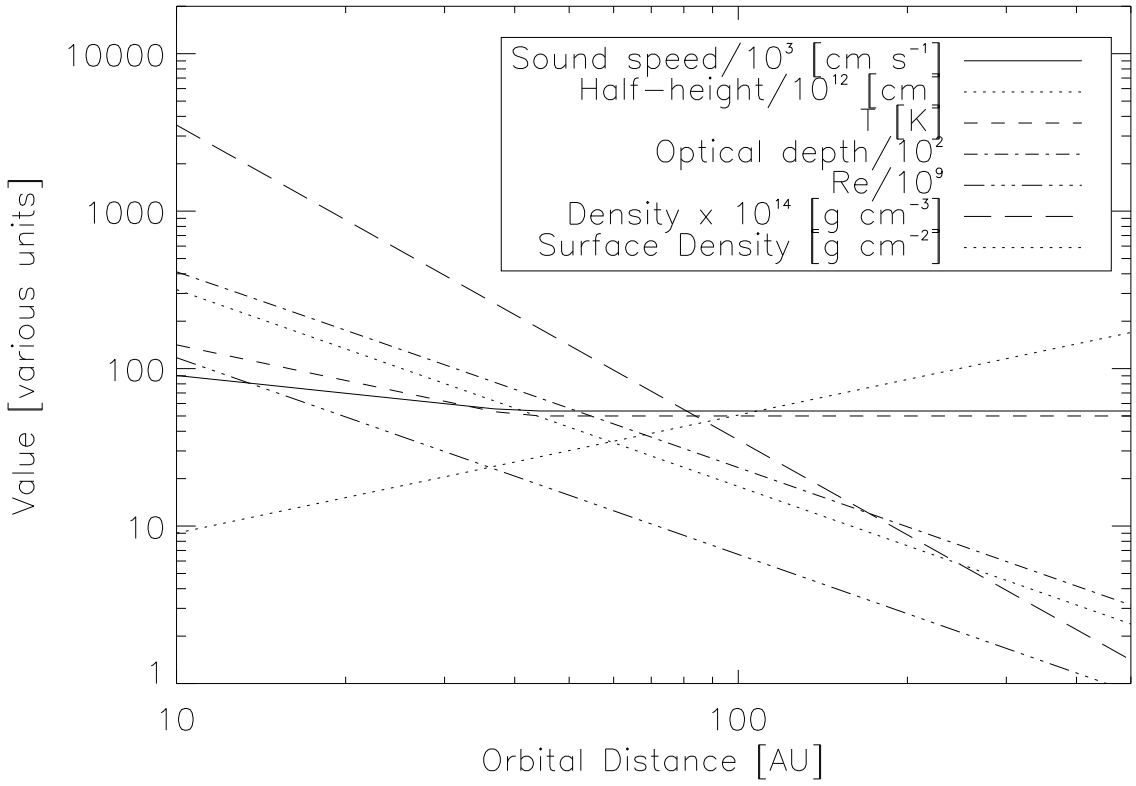

Figure 3.3: Several quantities across the initial input disk, Baseline case.

3.2.2 Photosputtering

Photosputtering, or photodesorption, is the process whereby photons incident to a surface cause the ejection of surface atoms or molecules. This process has been used to explain the lack of ice mantles on interstellar grains, and as one candidate intermediate source for the atomic hydrogen atmosphere of Ganymede (Barlow 1978; Westley *et al.* 1995; Barth *et al.* 1997).

Laboratory measurements of Westley *et al.* (1995) at $T = 35 - 100$ K with 10.2 eV photons into water ice indicated an ejection efficiency (molecules photon^{-1}) of $\epsilon_s = 0.1\% - 1\%$. The destruction rate can be calculated:

$$(dr/dt)_{\rm sput} = \frac{L\,\epsilon_s}{4\pi d^2}\frac{m_{\rm H_2O}}{\rho_{\rm H_2O}} \quad . \qquad \text{ice sputtering rate} \qquad (3.24)$$

For luminosity $L(\lambda > 912\text{Å}) = 5 \times 10^{49}$ photon s^{-1}, $d = 0.1$ pc, $\epsilon_s = 0.1\% - 1\%$, $m_{\rm H_2O} = 3 \times 10^{-23}$ g, $\rho_{\rm H_2O} = 1$ g cm^{-3}, it follows that $(dr/dt)_{\rm sput} \sim 0.5 - 5$ μm yr^{-1}. Presumably in the Orion nebula this range is an upper limit, because only a fraction of the surface area will be clean, exposed ice. Furthermore, in an optically thick disk the sputtering rate must be weighted by the fraction of time each particle is actually exposed to FUV radiation; *i.e.*,

$$(dr/dt)_{\rm sput} = \exp(-\tau_{\rm FUV})\frac{L\,\epsilon_s}{4\pi d^2}\frac{m_{\rm H_2O}}{\rho_{H_2O}} \quad . \qquad \text{ice sputtering rate, } \tau > 1 \qquad (3.25)$$

3.2.3 Photoevaporation

Gas loss

The FUV-dominated photoevaporation case of Stoerzer & Hollenbach (1999) is relevant to most of the large (*i.e.*, spatially resolved, $R > 20$ AU) dark disks in Orion. I

choose it and handle it according to (3.5) – (3.6). The disk size R evolves, and is defined as being the outermost location in the disk with $\tau_{\rm FUV} > 1$. Within the disk, the mass loss rate per area is taken to be constant – a simplification that slightly overestimates the mass loss for $R \lesssim G m_{\rm H} M_{\rm star}/(kT) = 60$ AU, where the velocity of the 1000 K outflow is sufficient to gravitationally escape the star. Most of the surface area is – and most of the interesting results are – beyond this distance, where the mass loss rate is accurate.

Dust loss by entrainment

The bright ionization fronts surrounding the photoevaporated disks are usually seen by their bright emission. In several disks, however, a fascinating phenomenon is seen: dark patches obscure portions of the otherwise bright IF. Instead of just losing gas mass, the disks appear to be losing dust grains entrained with the gas in the outflows

Presumably these dust grains represent the small end of the size distribution in the disks. Small particles are easily entrained, while large particles do not have sufficient force per mass to escape the gravitational bounds of the star and disk. Entrainment may be caused either by neutral-neutral or ion-ion interactions between the gas and dust; however, in both cases, forces from radiation pressure by FUV photons going against the flow could reduce the entrainment force. To constrain the conditions under which dust loss can occur, the flow forces can be calculated.

For a neutral outflow, the Stokes cross-section of a particle in a flow can be used to calculate the force on a particle,

$$F_{\rm neutral} = 2 n_0 \, \pi r^2 m_{\rm H} v_0^2 \qquad \text{neutral-neutral outflow drag force} \qquad (3.26)$$

The ion-ion drag force depends on the charging ratio of both the grains (charged directly by the FUV photons), and the outflow (charged by byproducts of the grain charging). Mathews (1967) investigates grain charging mechanisms in HII regions, using

a balance between ionization and recombination of dielectric grains. Assuming his ionization efficiency $\phi = 0.2\ e^{-1}$ photon^{-1}, $T = 10^3$ K, and a hydrogen ionization fraction 10^{-4}, his work (eq. 18) yields a typical grain charge of

$$q_{\rm dust} = 22,000\, q_e \frac{r}{\mu{\rm m}} \tag{3.27}$$

per grain. The coulomb drag force of Northrop & Birmingham (1990) can then be used to calculate the force on a particle, assuming a 3D Lorentzian velocity distribution,

$$F_{\rm ion-ion} = \frac{6\, q_{\rm dust}^2\, n_0}{\pi r^3 \rho_s v_0^2} \left(\tan^{-1} \frac{v_0}{a} - \frac{v_0/a}{1+v_0^2/a^2} \right) \ln \frac{\lambda_{\rm D}}{r} \tag{3.28}$$

with ion thermal velocity a and Debeye length $\lambda_{\rm D} = (kT/r\pi n_0 e^2)^{1/2}$.

The radiation pressure on a grain can be easily calculated,

$$F_{\rm rp} = \frac{r^2}{d^2} \frac{L_{\rm star}}{c} \tag{3.29}$$

as can the gravitational force,

$$F_{\rm grav} = \frac{4}{3} \pi r^3 \rho_s \frac{G M_{\rm star}}{R^2}\ . \tag{3.30}$$

All four of these quantities are plotted in Figure 3.4 for nominal HST10 parameters. The number density at the outflow base is $n_0 = 4.2 \times 10^6$ cm^{-3} (Stoerzer & Hollenbach 1999). As can be seen, the dominant loss process is neutral drag; the low ionization fraction causes ion drag to be unimportant. Even at the relatively close distance of HST10, radiation pressure is also not significant. A balance between the gravitational and neutral drag forces yields the maximum particle size entrained,

$$r_{\rm entrain} = \frac{3}{2} \frac{m_{\rm H}\, v_0^2\, n_0 R^2}{\rho_s\, G M_{\rm star}}\ . \tag{3.31}$$

I assume that particles smaller than this are entrained with the outflow, and larger particles are retained by the disk. Because of the R^2 dependence, particles are

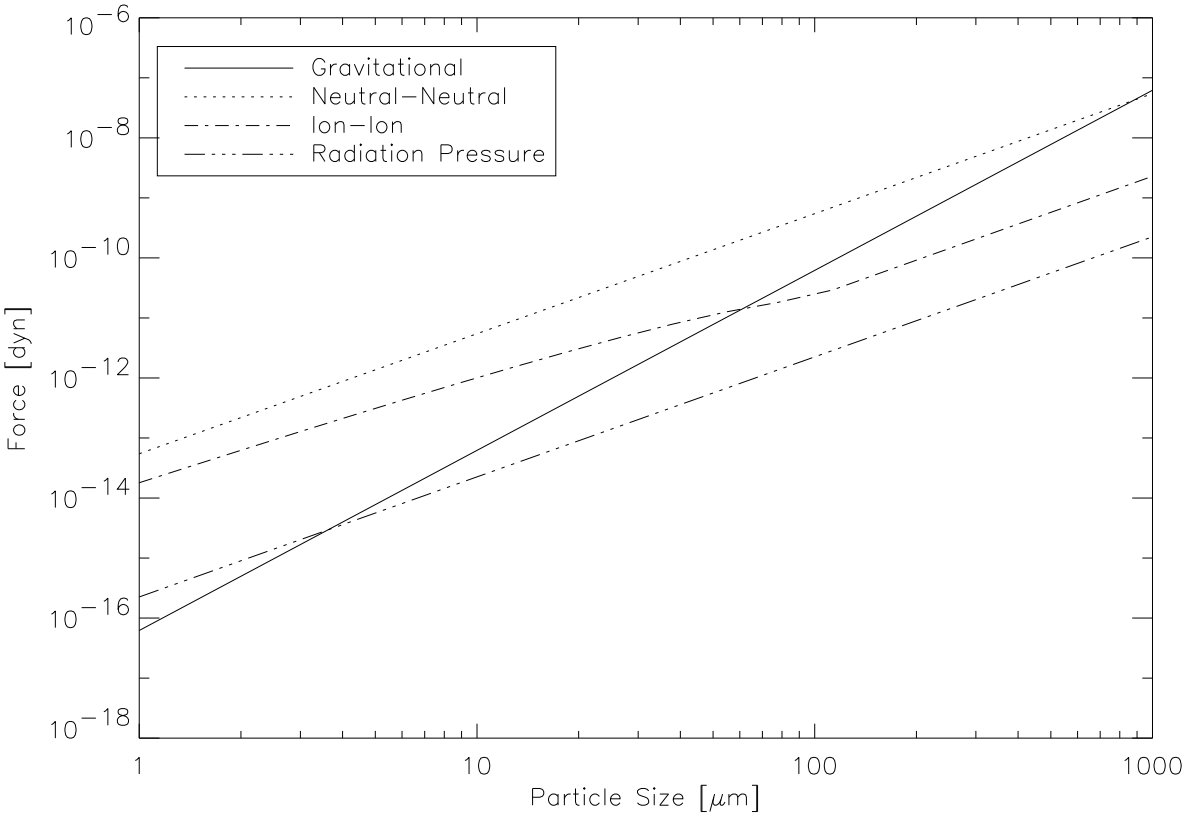

Figure 3.4: Particle forces, $R = 66$ AU. Only the neutral-neutral drag force is comparable to the the force of gravity. At this distance, particles up to $r \sim 900\mu$m are efficiently entrained into the neutral outflow (3.31).

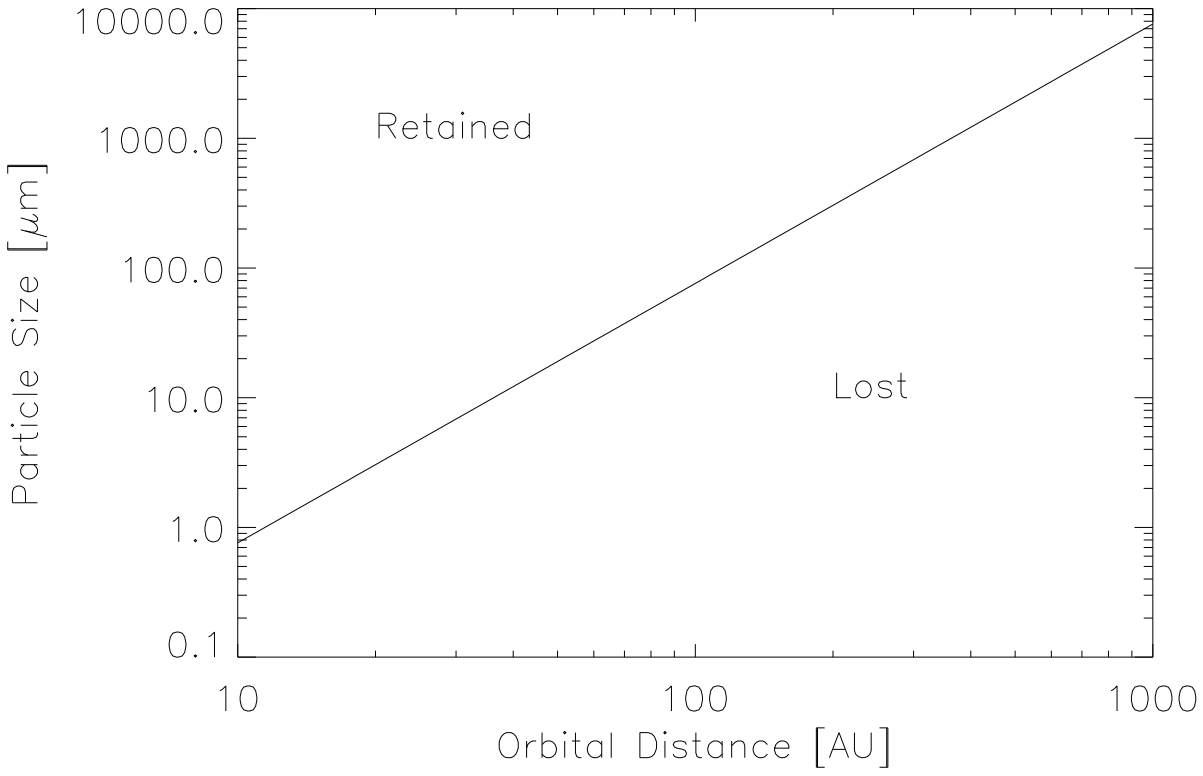

Figure 3.5: The largest particles entrained by the evaporating neutral outflow. Particle size decreases inward as grains are more strongly gravitationally bound.

more difficult to retain in the outer disk, where they also are expected to coagulate more slowly: both the production and retention of large particles at the outer edge are difficult.

3.2.4 Other processes

There are several processes considered by earlier models that are not used in the present one, in particular: thermal motion, vertical settling, radial drift, and gravitational growth. These effects will now be considered.

Vertical settling

As particles grow in mass, their motions become controlled less by the gas nebula as they decouple. Small grains are efficiently suspended by the gas nearly indefinitely, but large grains gravitationally settle to the midplane on shorter timescales. As was noted by Weidenschilling (1980), if coagulation does not occur, micron-sized grains well not settle to the midplane on a planetary formation timescales.

Dubrulle *et al.* (1995) have analytically modeled the settling times and scale heights for particles in the solar nebula. Based on a model using turbulent diffusive transport, they calculate an equilibrium dust scale height h given a gas scale height H,

$$h = H \left(\frac{1}{\gamma + 1} \right)^{1/4} \sqrt{\frac{\alpha}{\Omega \tau_f}} \quad . \tag{3.32}$$

Rearranging, inserting (3.18), and taking $\gamma = 2$, we find the maximum particle size suspended a distance $h/H = 1/2$ above the midplane to be

$$r = \frac{8}{3\pi\sqrt{3GM}} \frac{\rho_g}{\rho_s} \alpha c_s R^{3/2} \quad . \tag{3.33}$$

For the nominal input parameters in Table 3.1, the characteristic size suspended ranges from 30 cm at the outer edge to 1.2 cm at the inner edge. Therefore, for parti-

cles up to this size, the disk can be considered well-mixed, and vertical settling not a controlling factor.

The disk's vertical homogeneity may also be affected by sputtering ablation at the outer edge, if sputtering occurs on a faster timescale than the 'exposure time' of a particle at the outer edge. Assuming sputtering occurs only in the outer optical depth, the effect can be characterized by the relationship

$$\frac{2\pi}{\Omega\ \tau} < \frac{r}{(dr/dt)_{\rm sput}} \quad . \tag{3.34}$$

The applicability of both these conditions will be examined in section 3.5.2.

Radial drift

Radial drift due to differential keplerian-gas velocity is included in both the Stepinski & Valageas (1997) and Weidenschilling (1997) models. The characteristic property is that mass is transported inward at speeds reaching $10^3 - 10^4$ cm s^{-1} for a narrow range of particle sizes that are only moderately well-coupled to the gas. Between 30 and 300 AU, $v_{\rm rad}$ decreases by a factor of 50 (Weidenschilling & Cuzzi 1993), due to the lower differential rotation and lower gas density. Turbulent collision velocities, however, decrease much more slowly over the same range, a factor of three for nominal disk parameters, *e.g.* (3.35). Therefore, radial drift has been omitted in the current model. A future model should include radial drift, in order to study the interesting mass redistribution results found by Stepinski & Valageas (1996) and Weidenschilling (1997), even though the effect at the outer edge may be small.

Thermal motion, gravity, and Poynting-Robertson drag

Although Weidenschilling (1997) included thermal motion as a grain growth process for the smallest, micron-sized particles, this was probably chosen because of the emphasis of that work on radial mass distribution at much larger sizes. For nearly all

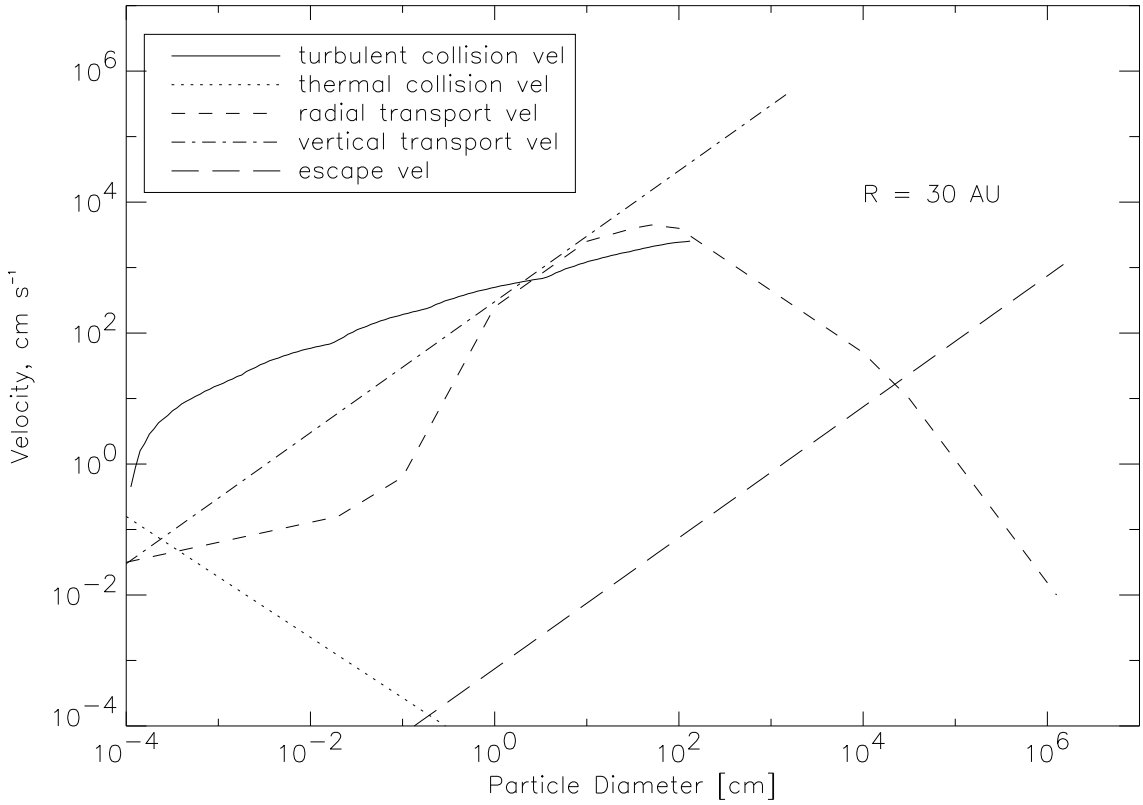

Figure 3.6: A variety of velocities for the model disk at 30 AU. Turbulent coagulation velocities exceed those of thermal motions, which are ignored in the model. Radial drift is potentially important in both redistributing mass and causing collisions between different-sized particles; however, radial collision velocities will be much smaller than the transport velocities shown here. Gravitational effects become important only for the largest particles. Vertical velocity ('settling') is plotted for reference. The solid curve plots the collisional velocity between particles of r and $2r$; like-sized particles have relative velocity of zero (3.23), and this effect will reduce the *collisional* radial velocity from the radial velocity shown. Adapted in part from Weidenschilling (1997).

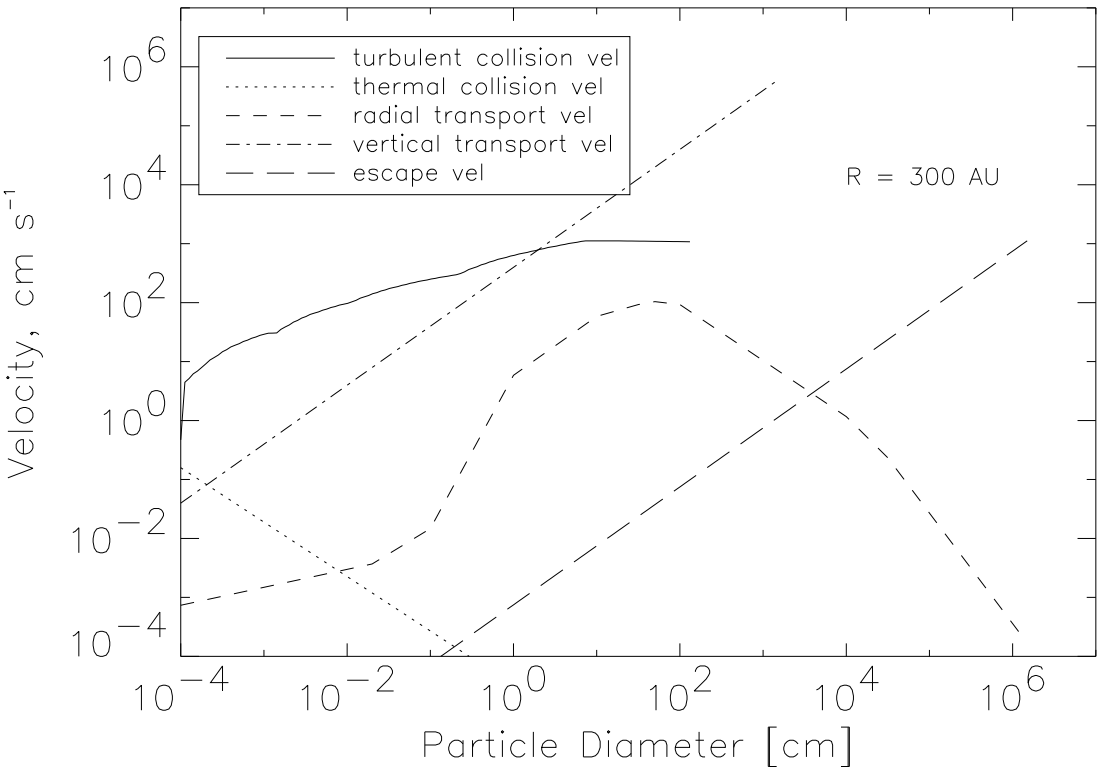

Figure 3.7: Same as above, for $R = 300$ AU.

sizes and locations considered here, collision velocities from convection greatly exceed those of thermal motion, and I have neglected the latter.

Inter-particle gravitational effects begins to become important when the collision speeds approach the particles' escape velocities. This condition is met for $r \gtrsim 10^4$ cm, and I explicitly stop the model before particles reach this size.

Poynting-Robertson drag (*e.g.* Wallis 1986) is a relativistic momentum-loss process that causes particles to spiral in toward a central illuminating and gravitating body. In the case of the Orion disks, particles are typically several hundred optical depths beneath the exterior, so P-R drag from either the central or external star is unlikely to be a dominant process on short timescales.

3.3 Numerical Model

The two-dimensional PAPADUM (**P**roplyd **A**ggregation **P**hotoevaporation **A**nd **DU**st **M**odel) code developed here numerically tracks the evolution of gas and dust in circumstellar disks like those seen in Orion. A flowchart is shown in Figure 3.3. The processes included are a) grain growth due to turbulent convection; b) photoevaporation of gas and entrained dust in an FUV-induced outflow; and c) photosputtering of ice particles. The nebula is described by three state vectors $n_i(r, R, t)$, $n_s(r, R, t)$, and $\Sigma_g(R, t)$ for the abundance of ice, silicate, and gas at radial distance R, grain size r, and time t. No transitions between the three independent state vectors are made, and mass may be lost from the system but is not added. Subsequent bins have a mass ratio $\sqrt{2}$, which is observed to be small enough to prevent bin-size effects. Collisions between particles result in a new particle with the same density as the parent particles. The gas:dust mass ratio is 100, and 'dust' is defined as being 1/3 ices and 2/3 silicates by mass (*e.g.*, Pollack *et al.* 1994).

The time increment is adjusted after each timestep so as to maximize accuracy while minimizing computation time. The quantity of material leaving or entering any

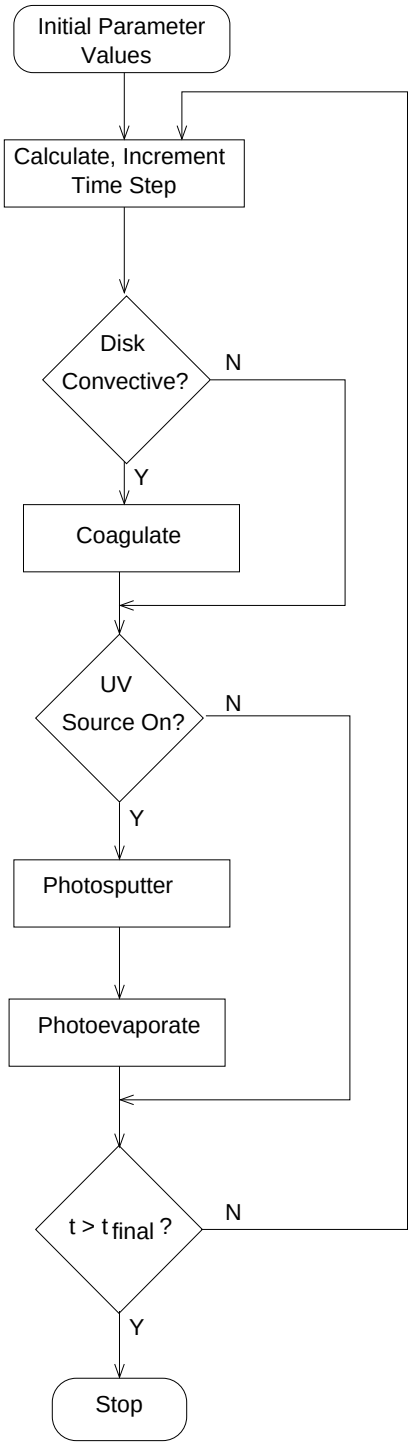

Figure 3.8: Flowchart of the PAPADUM model.

Table 3.1: Nominal input parameters for disk model

Name	Parameter	Shallow Disk	Baseline Disk	Steep Disk
Inner disk cutoff	R_1	10 AU	10 AU	10 AU
Outer disk cutoff	R_2	500 AU	500 AU	500 AU
Surface density, 40 AU [g cm^{-2}]	Σ	100	100	40
Mass distribution exponent	k_r	1	2	3
Photosputtering rate	$(dr/dt)_{\rm sput}$	0.01 μm yr^{-1}	0.1 μm yr^{-1}	1 μm yr^{-1}
Sticking coefficient	ϵ	1	0.5	0.1
UV photoevaporation start time	$t_{\rm UV}$	10^4 yr	10^3 yr	0 yr
Outflow column density [cm^{-2}]	N_D	1×10^{21}	3×10^{22}	3×10^{22}
Distance to θ^1 Ori C	d	0.1 pc	0.1 pc	0.1 pc
Gas:Dust mass ratio	$R_{\rm g/d}$	100	100	100
Silicate:Ice mass ratio	$R_{\rm s/i}$	2	2	2
Turbulent viscosity parameter	α	10^{-2}	10^{-2}	10^{-2}
Initial dust size exponent	q	3.5	3.5	3.5
Initial dust size range	$r_{\rm max}(t_0)$	$0.1 - 1$ μm	$0.1 - 1$ μm	$0.1 - 1$ μm
Outflow temperature	$T_{\rm outflow}$	1000 K	1000 K	1000 K
Central star mass	$M_{\rm star}$	1 $M_\odot$	1 $M_\odot$	1 $M_\odot$

particular bin must be small (typically $\sim 5\%$), so as to eliminate numerical artifacts; this is observed to usually correspond to a stepsize $\sim 2\%$ of the elapsed time. Bins with extremely low populations (typically $\lesssim 10^{-20}$ of the disk mass) are considered to be numerical artifacts and eliminated. When convection and photoevaporation have ceased throughout the entire disk the model is stopped, typically after a few 10^5 yr and a few hours of CPU time.

3.4 Results of Numerical Model

Runs were performed for three classes of input parameters: 'Steep,' a low-mass disk with a steep dropoff in mass distribution ($k_r = 3$), a high sputtering rate, a low sticking coefficient, and UV illumination for the entire age of the disk; 'Shallow,' a broad, massive disk with $k_r = 1$, $t_{\rm delay} = 10^4$ yr, a low sputtering rate, and fully-sticking particles; and 'Baseline,' with moderate parameter values. The inner edge is set to be $R_1 = 10$ AU; inward of this distance, heating by and accretion onto the central star become significant and require different methods to handle. The outer disk radius was chosen to be $R_2 = 500$ AU; because there is no radial mass transport, the dynamics

Table 3.2: Nominal initial conditions for disk models

Name	Quantity	Shallow Disk	Baseline Disk	Steep Disk
Total disk mass	$M_{\rm disk}$	3.5 $M_\odot$	0.3 $M_\odot$	0.1 $M_\odot$
Edge-on optical depth	$\tau_{\rm edge}$	6.8×10^5	7.1×10^5	3.7×10^6
Face-on optical depth (inner edge)	$\tau_{\rm face}$	8300	2.4×10^4	8.1×10^4
Face-on optical depth (outer edge)	$\tau_{\rm face}$	3900	2.8×10^2	13
Disk mass loss rate at $t_{\rm UV}$ [$M_\odot$ yr^{-1}]	$\dot{M}$	4.3×10^{-7}	1.3×10^{-5}	1.3×10^{-5}
Gas mass (final/initial)		0.99	0.61	0.57
Silicate mass (final/initial)		0.99	0.63	0.65
Ice mass (final/initial)		0.17	0.07	0.00

of a smaller disk would be similar to that in the inner region of a large disk. The evaporation model is taken to be the FUV-dominated case of Stoerzer & Hollenbach (1999), and thus the mass loss rate is independent of distance to the illuminating star over a wide range of distances. Nominal values for initial quantities are listed in Tables 3.1 and 3.2.

Results from the three models are plotted in Figures 3.9–3.18. Several key features can be seen, including fast grain growth to meter-sized particles, truncation of the outer disk edge, and loss of substantial parts of the original disk. I will explore the reasons for these features in the three cases.

3.4.1 Baseline model

This model (Figures 3.9–3.12) explores the 'best guess' parameter values, or at least a parameter set bounded by extreme cases. In this particular case, grains coagulate uninhibited for $t_{\rm UV} = 10^3$ yr, until photosputtering and photoevaporation begin. These processes compete with coagulation for about 3×10^4 yr, eventually eroding the disks' outer edge inward to $R_2 = 285$ AU. At this point ongoing coagulation and sputtering have caused the optical depth to drop to $\tau_{\rm FUV} < 1$, and photoevaporation is unable to continue because FUV photons are not efficiently absorbed by the dust. Photosputtering and coagulation continue to operate, however, and the model is stopped when $\tau_{\rm IR} < 1$ throughout the disk, inhibiting convection and thus coagulation. At this point the disk

has lost slightly over half of its original gas and silicate mass, and nearly all the ice mass. The remaining disk is sharply truncated, with its outer edge dominated by a wide size distribution ($q \approx 2$) of silicate particles at $r_{\rm entrain} \lesssim 0.16$ cm. This disk is now of low thermal optical depth, and coagulative processes move into regimes handled by other models.

3.4.2 Shallow model

The Shallow model (Figures 3.13–3.15) investigates a set of disk parameters which decrease the effect of external illumination on the final disk structure. The initial disk mass is (unrealistically) high, $M_{\rm disk} = 3.5 M_\odot$ due to the low mass exponent, $\Sigma \sim R^{-1}$. Because of the high initial optical depth throughout the disk, fractional mass loss is minimal, and the final disk mass is $0.78 M_0$. Because of the long delay $\tau_{\rm FUV} = 10^4$ yr before UV onset significant grain growth happens throughout the disk, and most of the mass loss is of the gas component.

The UV onset time in this model nominally indicates the delay between formation of the disk and fusion time of the O star. It should be noted, however, that disks that are formed coeval with O stars may have a non-zero UV onset time if the disks are formed outside the HII region's Strömgren sphere. Typical orbital times for disks *through* the nebula are on the order $10^5 - 10^6$ yr, so effective onset times higher that those examined here are quite possible. Photoevaporation of disks under a temporally-varying UV flux is not considered in the current model but will affect the final disk populations in Orion.

3.4.3 Steep model

The Steep model (Figures 3.16–3.18) probes the disk structure at parameter values tending to increase the effect of photoevaporation. The initial disk mass is the lowest of the three models, at $0.1 M_\odot$, and most of this mass is concentrated toward the inner disk, with a mass distribution $\Sigma \sim R^{-3}$. The radial exponent is significantly steeper than

our own present-day solar system, but comparable to that used by some other models (*e.g.*, $k = 3.78$ in the Stepinski & Valageas models) and derived from observations of large disks. The low optical depth coupled with immediate UV onset begins to truncate the disk quickly. In the inner regions – where most of the mass is – fast fast particle growth prevents significant mass from being lost from the entire system, even with external illumination turned on from the beginning. The Steep disk at $t \sim 1500$ yr (Fig. 3.17) provides the best qualitative fit of the three models to the Orion disks, with large particles at the outer edge of a thick, truncated disk.

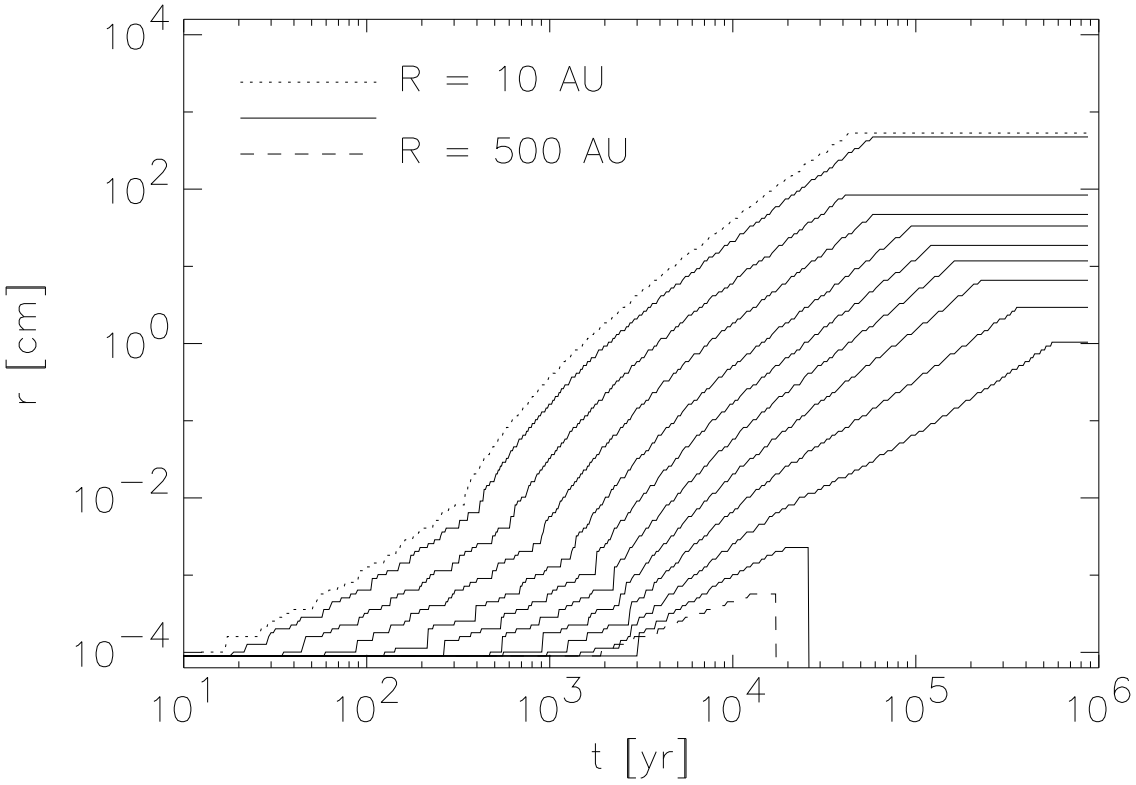

Figure 3.9: Evolution of peak particle size, Baseline model. Particles grow by turbulence-driven coagulation. When $r(R)$ is sufficiently large, the thermal opacity drops below unity, inhibiting convection and coagulation. Particles at the outer edge are swept away from the disk before growing sufficiently large so as to be gravitationally retained. The y axis represents the size where $n(r)\,r^2$ is the greatest. Slight changes in slope are due to transitions between two velocity scaling laws.

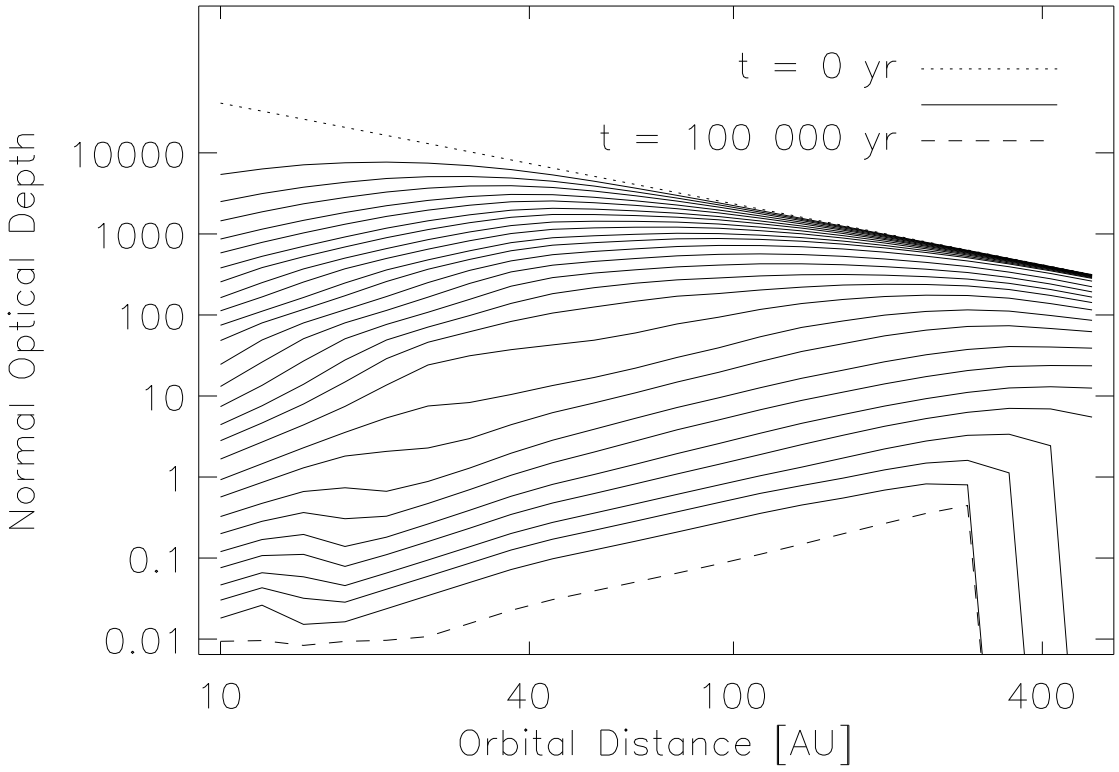

Figure 3.10: Evolution of optical depth, Baseline model. Grains at the inner edge coagulate fastest, quickly reducing their optical depth and turning off convection. Particles at the outer edge grow slowly and are more easily entrained by the outflow, and are quickly lost from the disk on short timescales. The transition between these regimes causes a sharp-edged disk populated by large particles. Timesteps are spaced exponentially; that is, the $n = 26$ solid lines correspond to times of $t = \exp(5.1 + 0.21 n_i)$ yr; $n_i = 1 \ldots 26$.

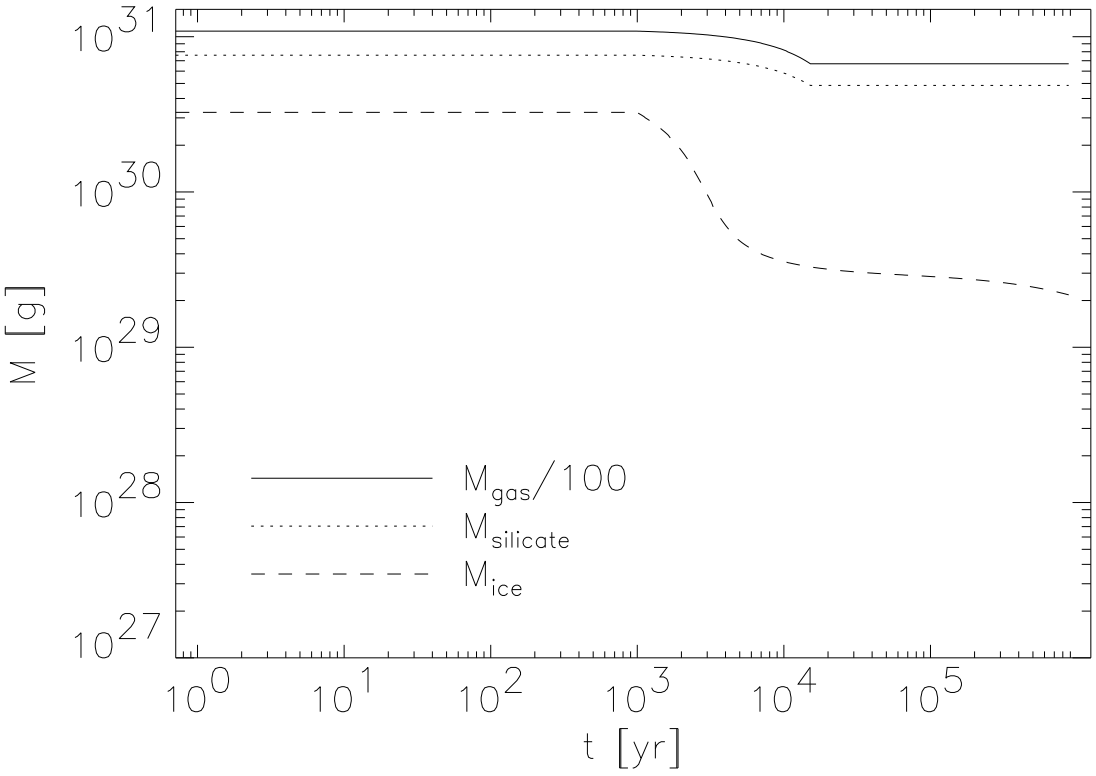

Figure 3.11: Evolution of bulk disk composition, Baseline model. After θ^1 Ori C turns on at $t = 10^3$ yr, gas outflow entrains both ice and silicate particles. As the silicate optical depth drops, photoevaporation is eventually inhibited, while photosputtering continues to reduce the ice mass.

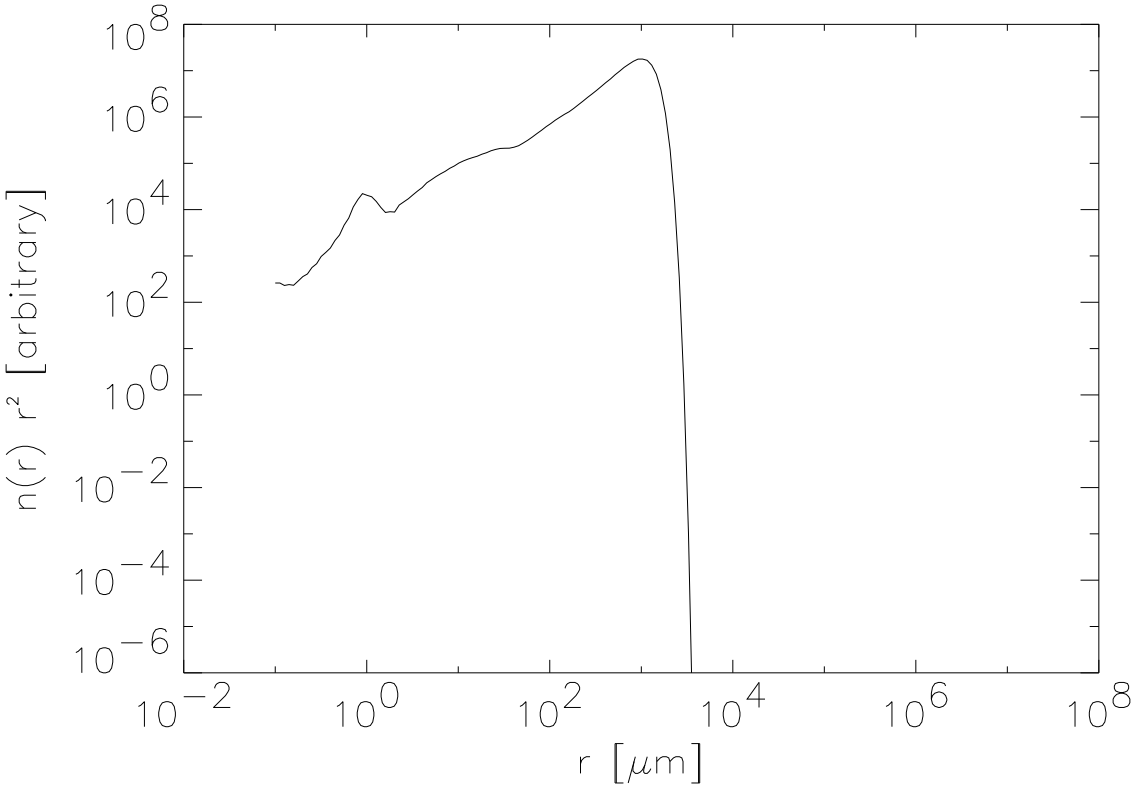

Figure 3.12: Final size distribution at outer edge, Baseline model. At this location, particles beyond $r_{\rm entrain} \sim 0.16$ cm are always safe against photoevaporation. When the optical depth is sufficiently low to inhibit photoevaporation, as it has here, all particles are retained.

3.5 Analytic treatments of model results

Some of the model results can been compared with published results as a validity check. Mizuno *et al.* (1988) presents numerical results of grain growth from sub-μm to cm-sized particles. Their Figure 2 (reproduced here, Figure 3.22) can be directly compared with the output from the Baseline model for equal parameter input (Figure 3.23). Agreement is very good.

3.5.1 Grain Growth

The equation for particle collision velocity (3.23) for grains well-coupled to a turbulent gas can be approximately integrated to analytically estimate the grain size evolution. Plugging in (3.10–3.18) and (3.21) and dropping small terms, one finds that

$$v_{\rm coll} \sim r^{1/2}\ D^{k_r/4} \quad . \tag{3.35}$$

To calculate an approximate particle growth timescale, one can consider collisions between a unimodal distribution of like-sized particles, and calculate that

$$\begin{aligned} \frac{dm}{dt} &\sim r^2\,\rho\,v_{\rm coll} \\ &\sim r^{5/2}\,R^{-\frac{3}{4}(k_r+1)} \end{aligned} \tag{3.36}$$

and thus

$$r(t,R) \approx c_1\,t^6\,R^{-\frac{3}{4}(k_r+1)} \tag{3.37}$$

where c_1 contains all the physical constants. Figure 3.24 plots (3.37) versus the model results. The good agreement suggests that model is working properly.

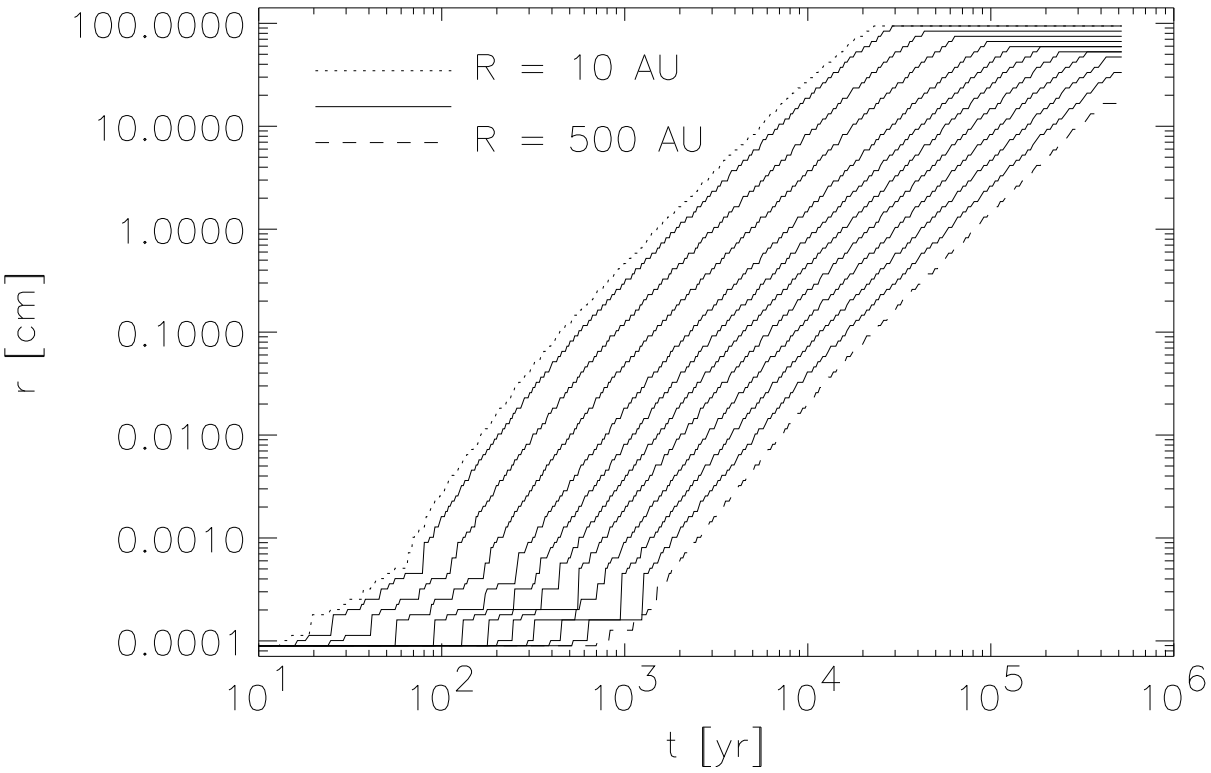

Figure 3.13: Evolution of peak particle size, Shallow model

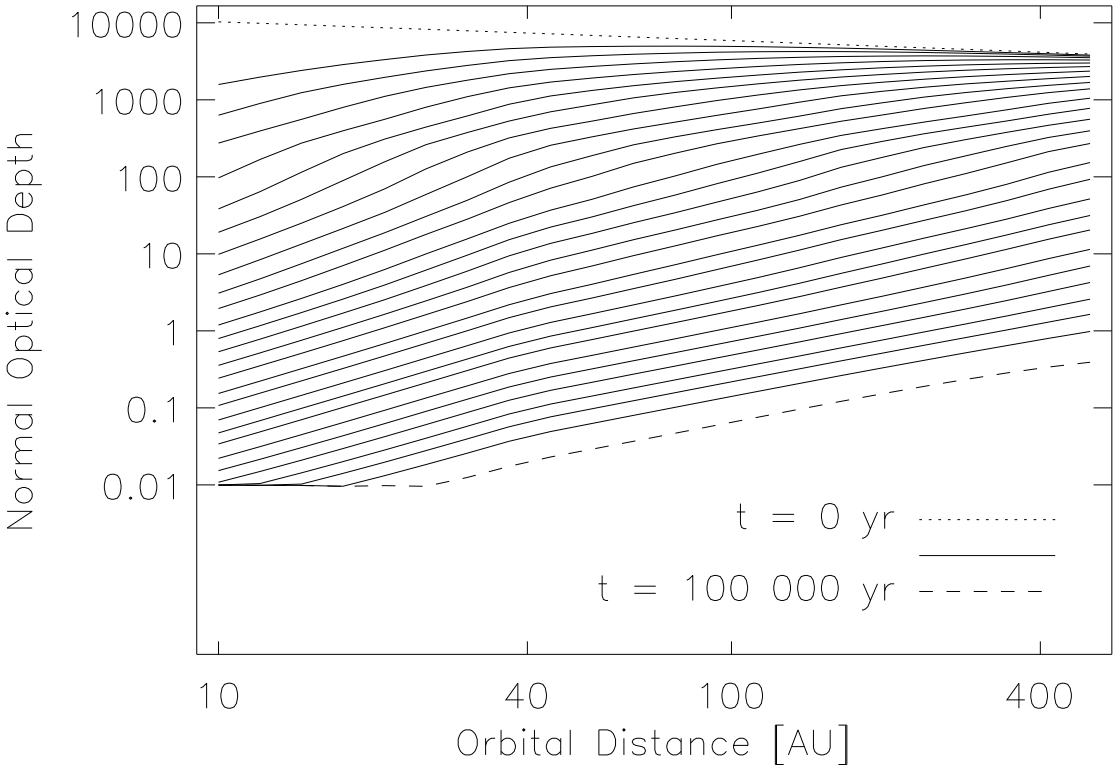

Figure 3.14: Evolution of optical depth, Shallow model

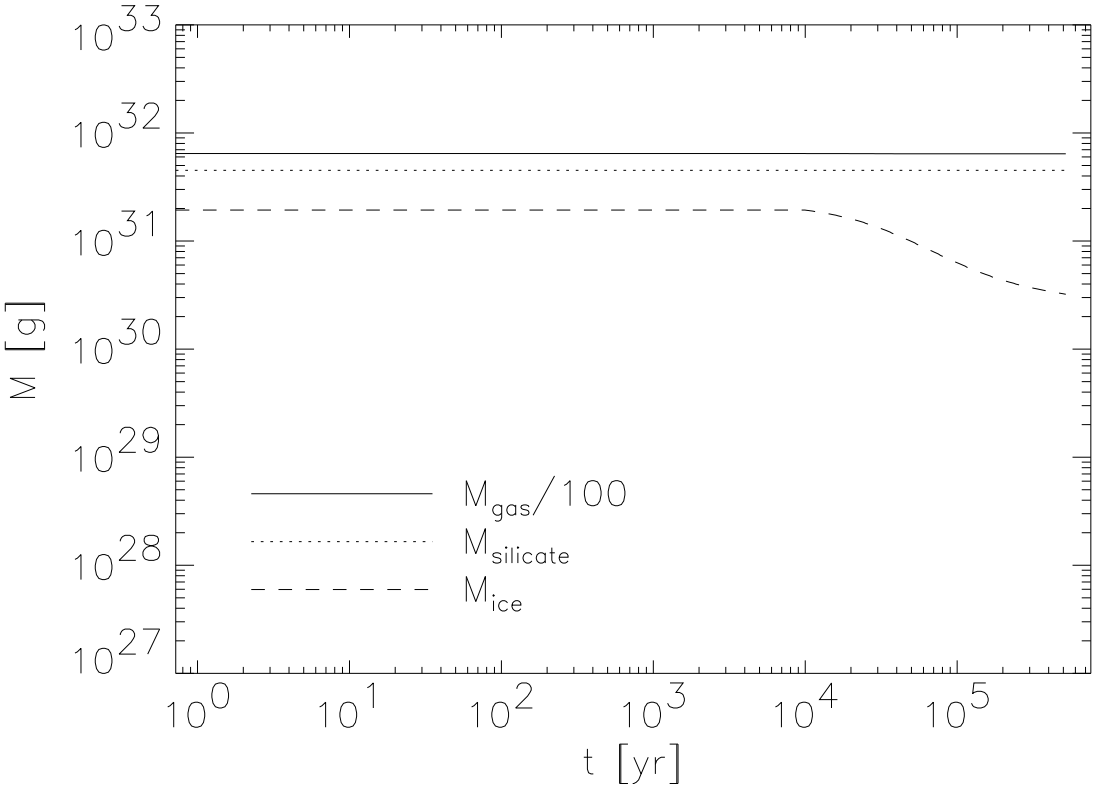

Figure 3.15: Evolution of bulk disk composition, Shallow model

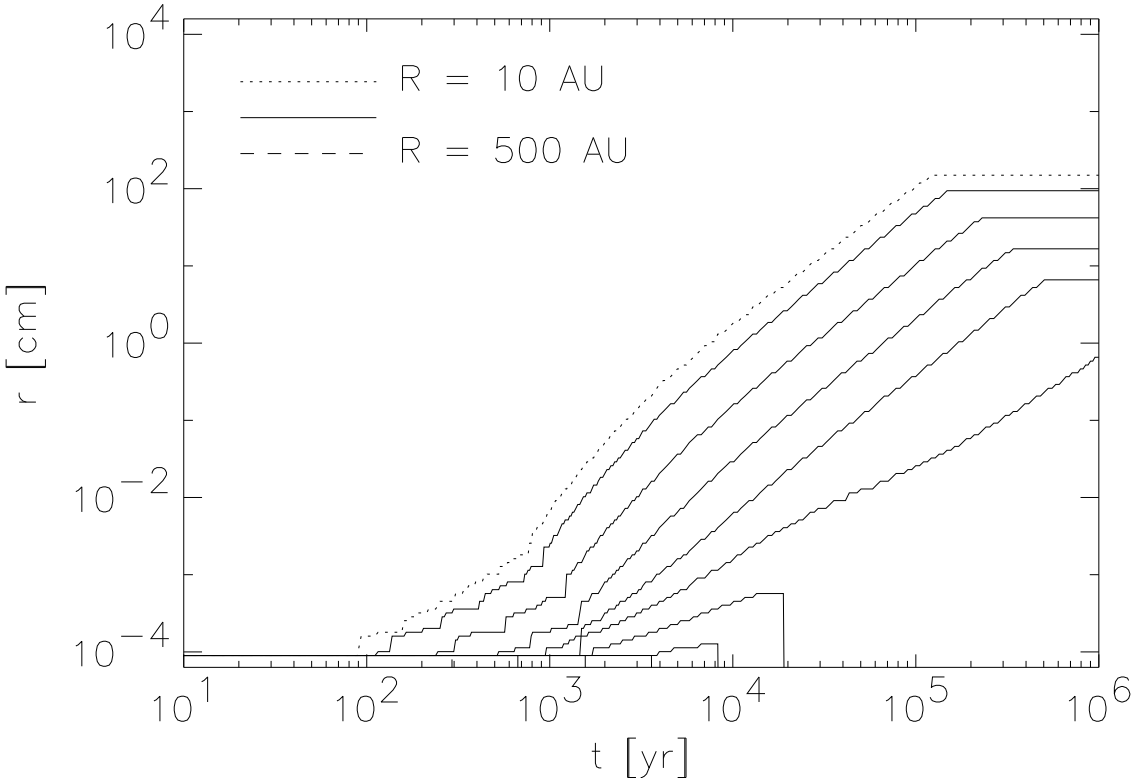

Figure 3.16: Evolution of peak particle size, Steep model

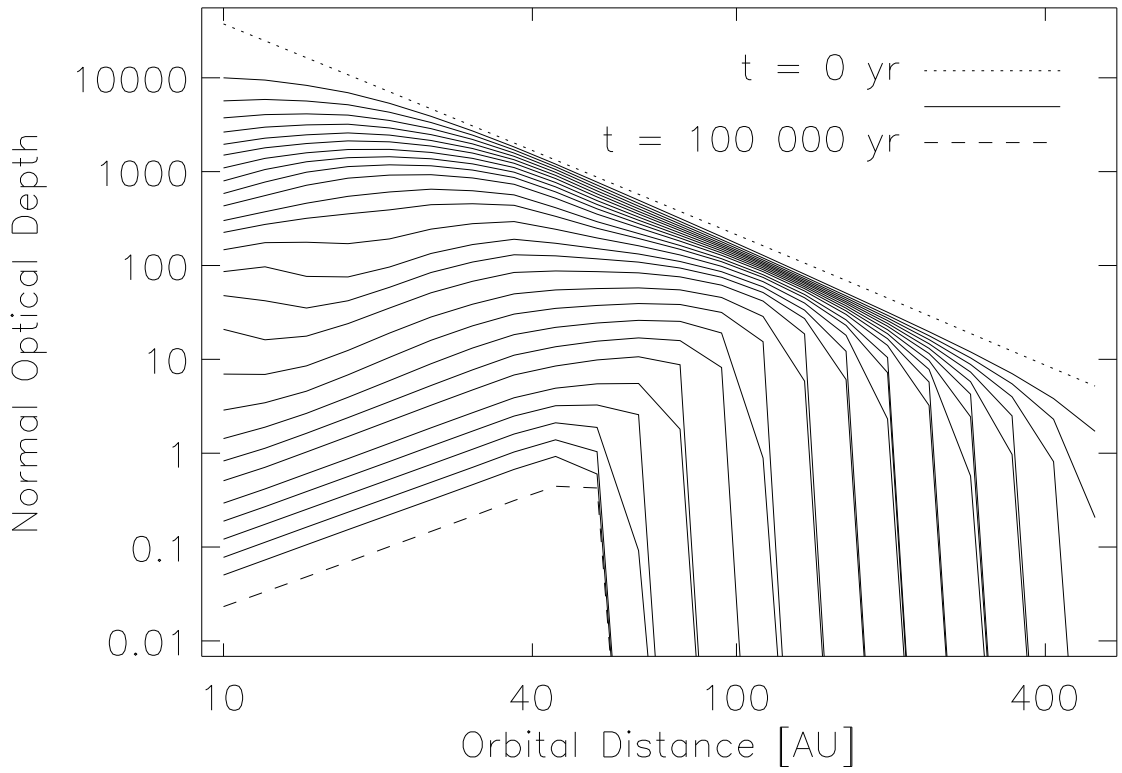

Figure 3.17: Evolution of optical depth, Steep model

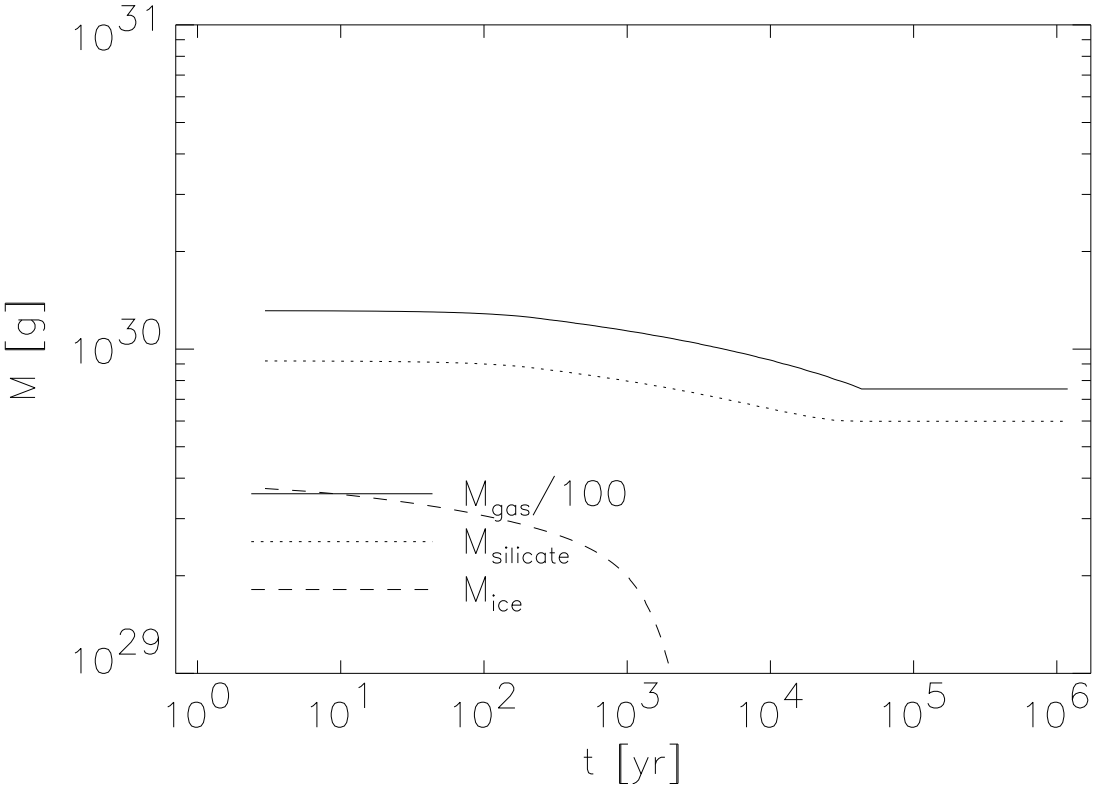

Figure 3.18: Evolution of bulk disk composition, Steep model

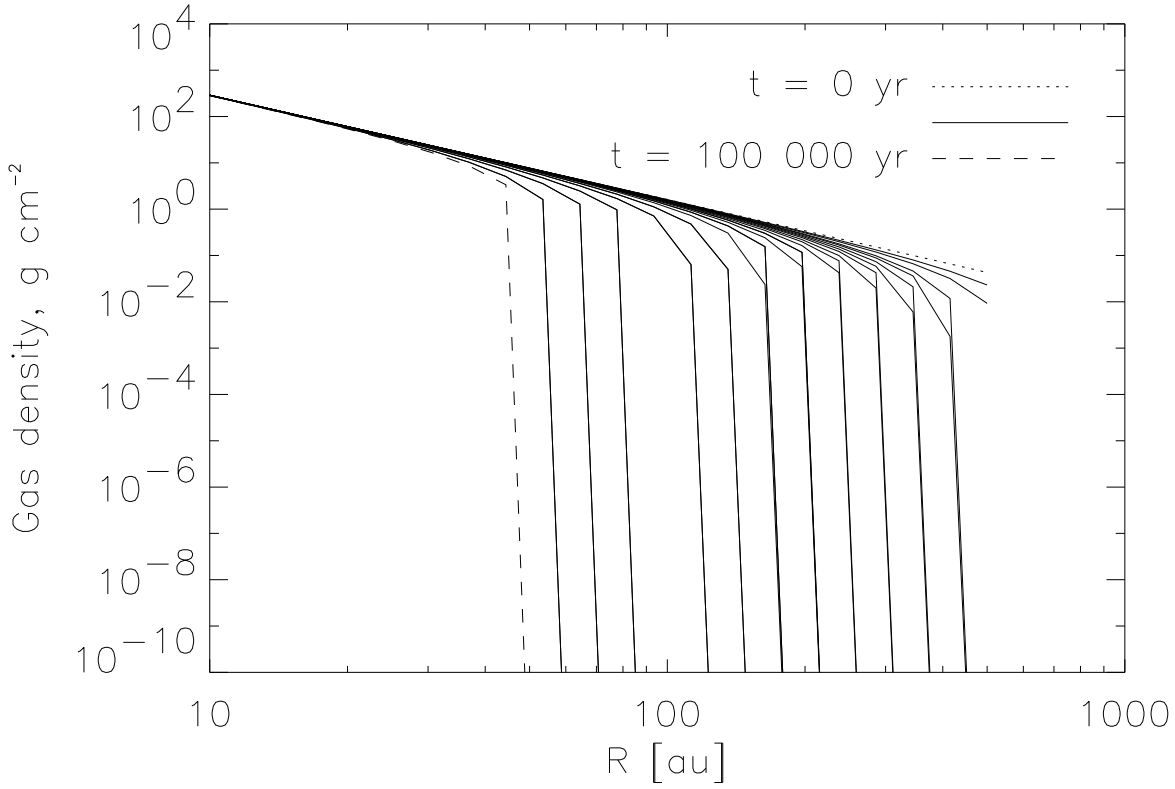

Figure 3.19: Evolution of gas distribution, Steep model

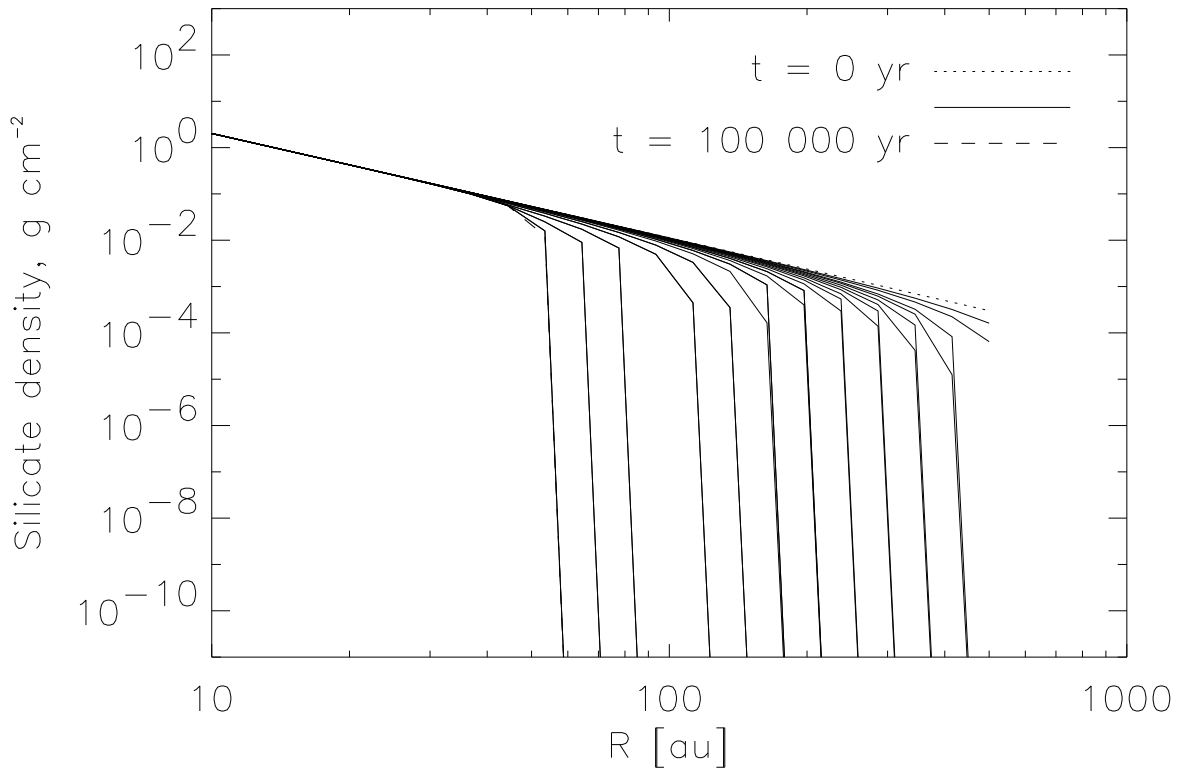

Figure 3.20: Evolution of silicate distribution, Steep model. Because gas loss is tied to the presence of dust, these two distributions closely follow each other.

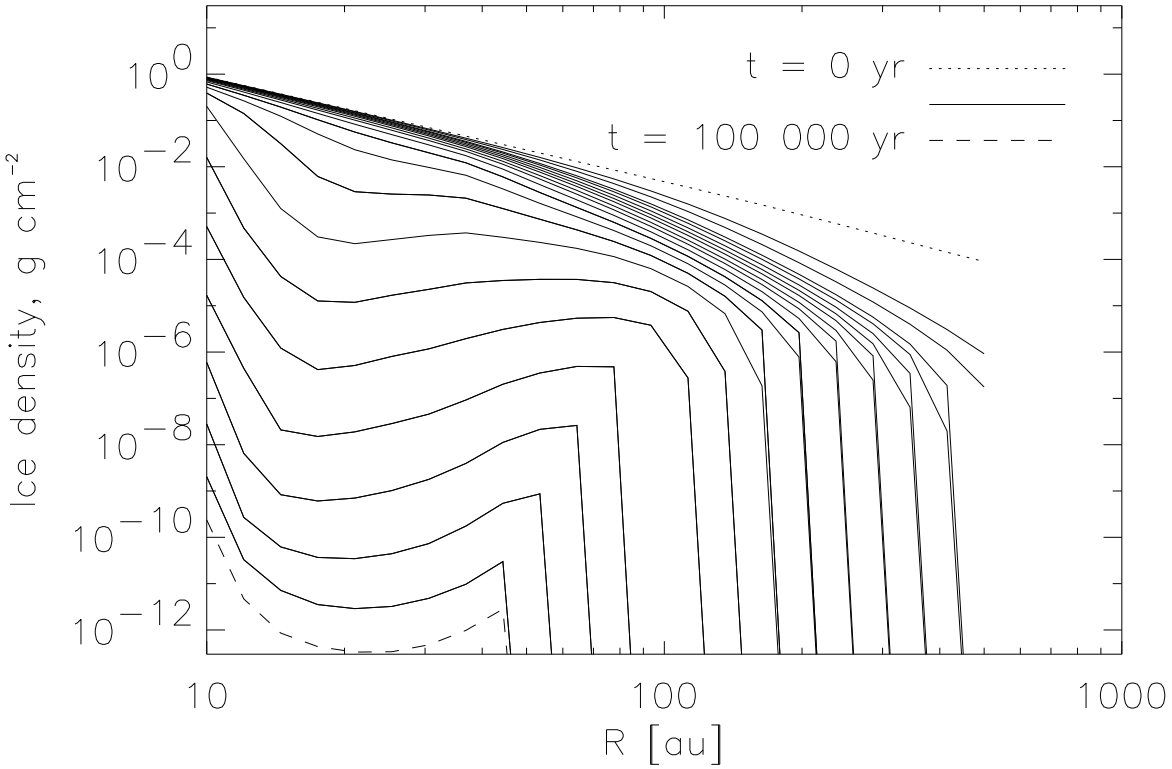

Figure 3.21: Evolution of ice distribution, Steep model. Ice loss exceeds that of silicates at the outer edge due to photosputtering. At the inner edge, coagulation causes a low τ, inhibiting sputtering relative to the rest of the disk.

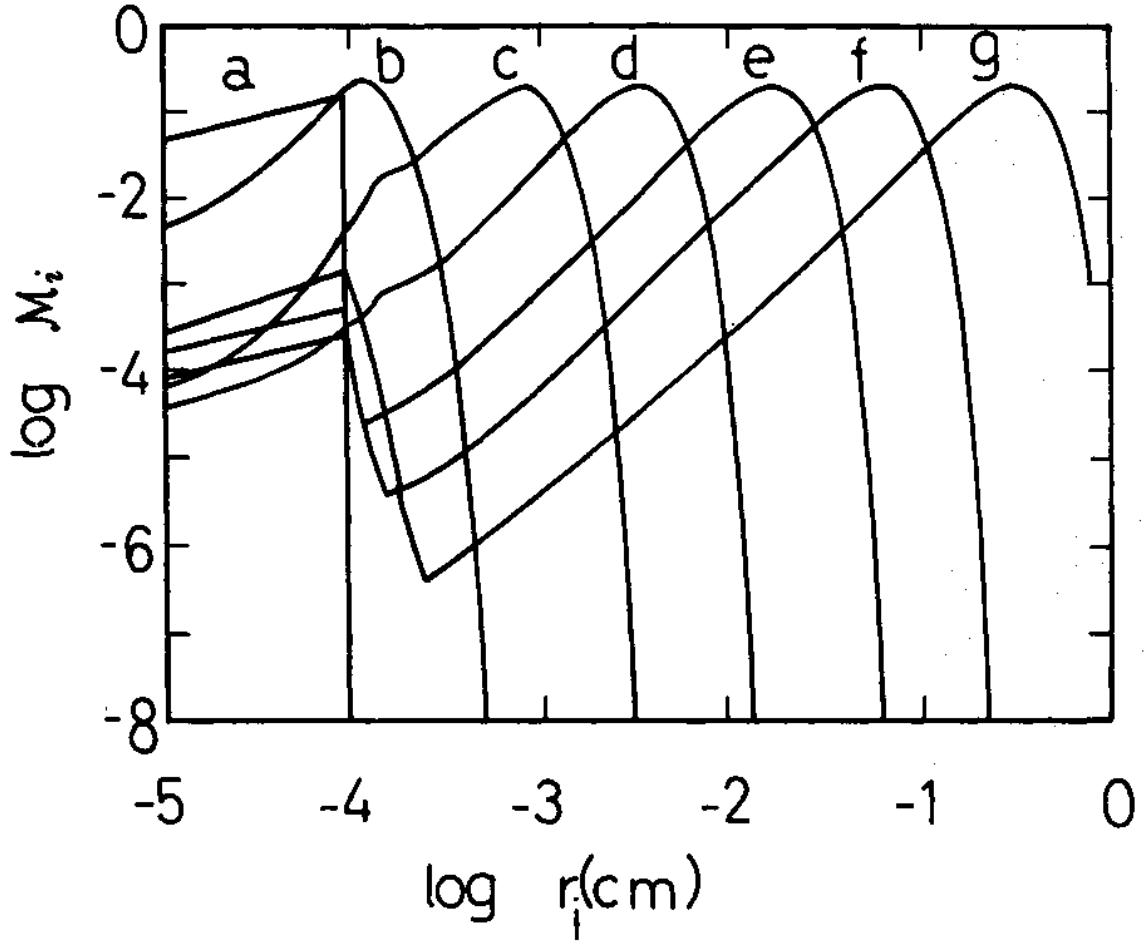

Figure 3.22: Grain growth in the Mizuno *et al.* (1988) model. Times a–g marked are for 0, 20, 98, 222, 517, 1020, and 2420 years. In a mass-conserving system, the area under each curve is preserved. All parameters are the same as the Baseline case. Reproduced from Mizuno *et al.* (1988).

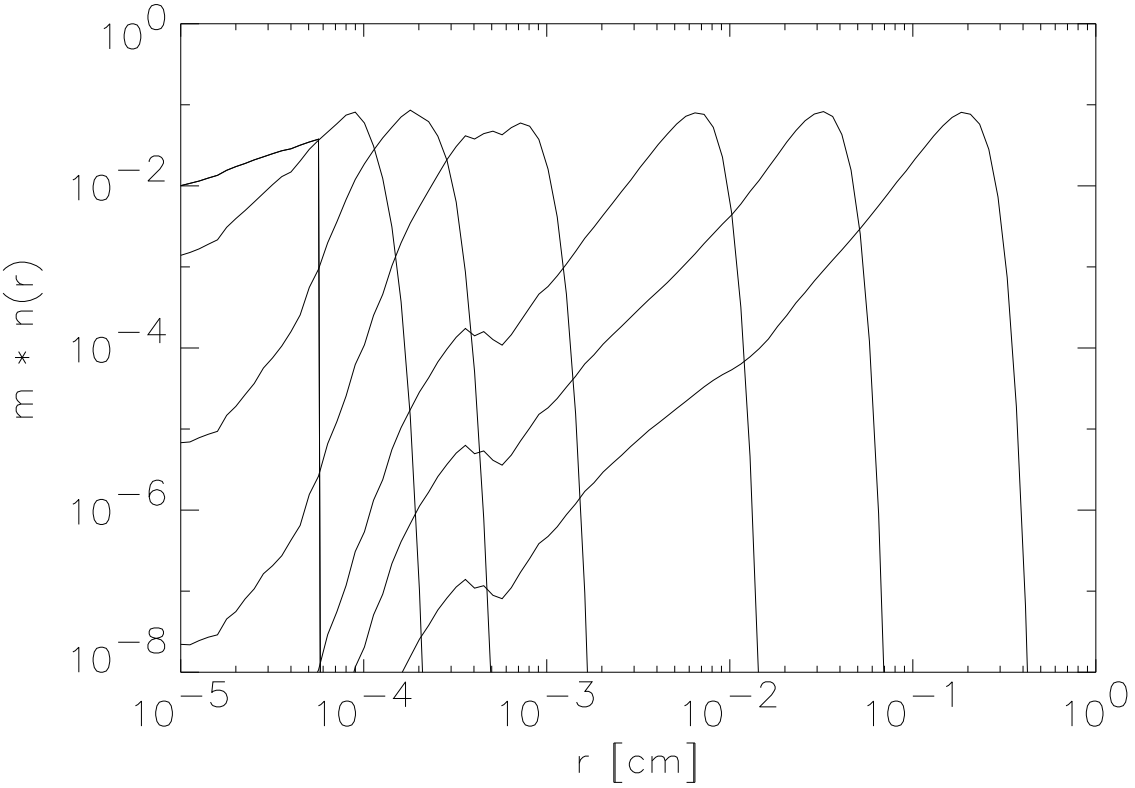

Figure 3.23: Same as figure 3.22, but the present implementation, Baseline model, silicate particles. The 'lumpiness' on the distribution tails is probably due to interpolation effects inherent in using the tabulated numerical results of Voelk *et al.* (1980).

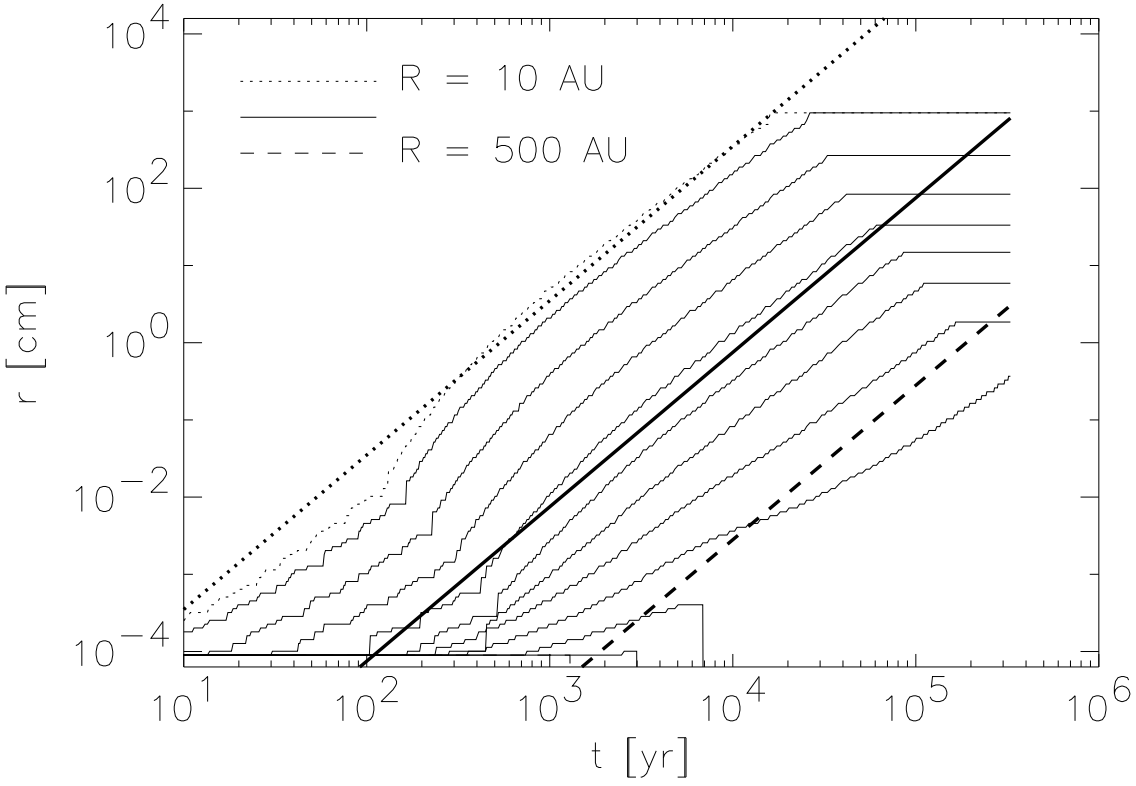

Figure 3.24: Fit to particle size evolution. The solid lines represent an analytic treatment of grain growth between like-sized particles, (3.37), where $r \approx 10^{22}\, t^6\, R^{-3}$ in cgs units. Thin lines are data for the Steep case. The greatest divergence is at high R, where sputtering and photoevaporation both discourage particle growth.

Table 3.3: Inputs that would *increase* loss processes, and make planetesimal formation more difficult.

• Ongoing dust accretion onto disk from nebula
• Production of secondary collisional products
• Self-consistent handling of photoevaporation rate across disk
• Realistic (< 1) sticking probabilities
• Aerodynamic properties of fractal grains
• Radial drift velocities due to high gas densities
• Steep (silicate) mass exponents in outer edge
• Ion-ion drag processes in EUV regime
• Further distances or FUV extinction causing EUV-dominated photoevaporation
• Treatment of condensation from gas onto dust
• Charged grain interaction with magnetic field

3.5.2 Discussion

The output from the numerical models is encouraging in that it uses realistic physical processes and parameters to quantitatively reproduce several key measurements of the Orion dark disks. In this work, the present parameter space has only begun to be explored, as is evident from Table 3.1, and there are far more processes occurring in the real disks than are considered in this model.

Tables 3.3–3.4 summarizes a few of the simplifications of the present model and the direction of their expected effect. It is difficult to quantify the effects of all these processes on the current results, except to note that most of them alone would have perhaps factor-of-several quantitative effects, but none have the obvious ability to make or break the bulk of the work here. Most of these processes have been studied in one or models before, and all of them could be parameterized and incorporated in a complete protoplanetary disk model. With that in mind, I shall consider the three models discussed previously, and their implications for solar system structure.

Comparing the two extreme cases, Steep and Shallow, it is not clear that the effects of external illumination have any measurable effect in the inner disk, $R \lesssim 40$ AU. Within this orbital distance, the evolution is almost completely dominated by coagula-

Table 3.4: Inputs that would *decrease* loss processes, and increase the production and stability of large bodies formed far out.

• Full treatment of ice-silicate collisions
• Full treatment of photosputtering in compound ice-silicate particles
• Self-consistent handling of secondary products in outflow opacity
• Generation of turbulence by vertical settling and decoupling
• Longer incubation times before UV onset
• High-mass ($> M_{\odot}$) central star
• Self-consistent vertical settling
• Incomplete convection at outer edges
• Mass loss by T Tauri winds

tive grain growth; growth is fast enough that photoevaporation does not significantly change the particle size distribution. It is reasonable to conclude that, given the current assumptions, the formation of terrestrial planets from silicates at several AU is not significantly affected by external illumination.

The formation of bodies in the outer solar system is more interesting. Current understanding of our solar system identifies the Edgeworth-Kuiper belt (EKB) of icy bodies extending outward from $R = 30$ AU to at least $R = 60$ AU, and perhaps much further (*e.g.* Tegler & Romanishin 1999). Due to collisional evolution and erosion after formation, much of the original population has been lost; the model of Stern & Colwell (1997) predicts that the original EKB had $\sim 15-50 M_{\oplus}$ in the region $30-50$ AU, corresponding to $\Sigma \sim 20$ g cm^{-2} assuming normal gas:dust ratios. Beyond this distance, knowledge of our own solar system is very limited. Presumably the EKB terminates at some distance, but neither observations (limited by the $1/R^4$ detection difficulty) nor theory have offered significant progress into this problem (*e.g.* Farinella *et al.* 2000). Could our own EKB have formed in a region like Orion? The Steep model truncates the disk at a distance comparable to the outer known edge of the EKB, suggesting that it may be difficult with these parameter values to recreate our outer solar system. However, uncertainties in the initial conditions preclude making a strong statement about the formation of our EKB just yet.

Bodies in the Solar System's Oort cloud of proto-comets were probably formed slightly closer than the EKB and were then gravitationally flung after a few 10^7yr to much larger distances ($R \sim 10^5$ AU, *e.g.* Levison *et al.* 1999). Because the radial transport occured well after the formation of giant planets, probabilites of Oort cloud formation are probably similar to those of Edgeworth-Kuiper belts.

The biggest modeling uncertainty in the structure of outer solar system populations may lie in our lack of knowledge of the initial mass distribution $\Sigma(R)$. Most models for our inner solar system have required power laws[†] with relatively shallow exponents, $k_r = 1/2 - 2$ (*e.g.* Lissauer 1987), in order for runaway gravitational growth to form the terrestrial planets and the gas giant cores. Clearly, the exponent must increase to $k_r > 2$ at some distance in order for the solar system's mass to be bounded. Some constraint on k_r at high R can come from observations of other large disks; for instance, modeling of the invisible parent bodies in the β Pictoris disk by Lecavelier des Etangs *et al.* (1996) suggested $k_r \lesssim 3$ out to $R = 800$ AU based on the present dust abundances. This disk's current configuration, however, is significantly more evolved than the Orion disks'. Theoretically, Yorke *et al.* (1993) have studied the collapse of a large ($R \sim 2500$ AU) cloud into a solar-mass disk and star, and found that between $R = 20 - 300$ AU, the disk was well-described by $\Sigma \sim R^{-3.5}$. [‡] This collapse was assumed to be in a cold molecular cloud, so the initial conditions may be substantially different from those in Orion. Still, it is clear that large disks *do* form in Orion, and it is possible that formation outside of the Strömgren sphere of θ^1 Ori C– indeed, where the largest disk currently lies – would not be entirely unlike that modeled by Yorke *et al.*. In that case, the high k_r could cause substantial truncation of large disks into the distance of our EKB.

[†] There is of course no *a priori* reason to use a power law, except that such a distribution is observed to fit portions of many disks, including our own solar system.

[‡] Their text erroneously gives an exponent of 2, but their figures are correct (H. Yorke, personal communication 2000.)

After photoevaporation has ceased, all the models continue to evolve the icy particle size distribution under photosputtering, and most of the cases result in nearly complete loss of all icy material from the disk. At a nominal sputtering rate (3.24), $(dr/dt)_{\rm sput} = 0.1\mu$m yr^{-1}, an O star could remove up to $r \approx 1m$ of material from a pure ice body over 10^7 yr. This result should be used with care, and may be unrealistic; actual loss rates are unlikely to be this high, because real bodies would quickly develop a protective silicate mantle and lower their sputtering efficiency. On the other hand, real bodies would also be in collisional evolution, and expose fresh surface on a regular basis. At the level of sophistication of the current model, it cannot be determined how important photosputtering may be on the final population of icy bodies.

Could photoevaporation affect the formation of giant planets in our solar system? The Jovian planets (Jupiter and Saturn) have historically been assumed to have formed by runaway gravitational growth of a rocky core of mass $10 - 20M_\oplus$, followed by gravitational sweepup of another $300M_\oplus$ of gas (*e.g.* Pollack *et al.* 1996). The major time constraint comes from the 10^7 year timescale for the sun's T Tauri winds to clear away gas from the nebula. Some recent models, however, form the Jovian planets in a qualitatively different manner which is much faster than is actually required; for instance, Boss (1997) uses gravitational instabilities in a heavy, shallow ($k_r = 1/2$) gas disk to form Jupiter within 10^3 yr. If the latter timescale is accurate *and* Jovian planets form near their present location, it is unlikely that photoevaporation could remove enough gas to significantly alter their formation. Orbital migration theories (*e.g.* Ward 1997) typically create torques between a viscous disk and a giant planet, and can move a planet inward from $R \sim 10$ AU. It is not clear that a giant planet could quickly form significantly further out and migrate inward to, for instance, 10 AU.

Could photoevaporation cause a loss of significant gas and dust at 10 AU over the longer, 10^7 year timescale? The numerical results from the runs presented here gives a definitive no, because coagulation is fast enough that the dust optical depth drops to

$\tau < 1$ within 10^4 yr. However, in this case the model may be deficient in its handling of collisions being entirely a coagulative process, with no secondary production. Gas can be lost in the presence of dust to heat it by FUV absorption. A small but continual production of dust by collisions between (meter-sized) planetesimals might be able to sustain photoevaporation at the same rate $\dot{M}$ as during the early phase. Given a gas density $\Sigma(10\ \mathrm{AU}) = 200\ \mathrm{gcm}^{-2}$, the timescale for loss of all gas is roughly 10^5 yr, significantly faster than the T Tauri nebular loss timescales. It is not clear whether collisional dust would or would not be produced at a rate sufficient to maintain this loss; this issue should be investigated more thoroughly.

Chapter 4

Planetary Rings

They say that heaven is like TV
A perfect little world that doesn't need you
And everything there is made of light
And the days keep going by
Laurie Anderson, Strange Angels

4.1 Introduction

Planetary ring systems have been discovered orbiting our solar system's four largest planets, and have been proposed to exist around two more (Mars & Pluto; *e.g.* Krivov & Hamilton 1997). Although the ring systems are diverse, each of the systems contains at least one dusty ring: a long-lived, low-optical depth ring sustained in steady-state by collisional production of dust by large, generally invisible parent bodies.

In many ways, dusty rings can be considered nearby analogues to the debris disks found orbiting dozens of stars, such as surrounding β Pictoris. The physical similarities are broad, as characterized in Table 1.1: each is dynamically old, collisionally relaxed, optically thin, and dominated by keplerian and laminar processes. The dust is quickly lost in a variety of ways, and replaced by production from much larger, usually unseen parent bodies. The debris disks are generally understood to be a somewhat older evolutional state of the protoplanetary disks described in Chapters 2 and 3. Dating the disks is relatively difficult once their central star has entered the main sequence; estimates for β Pictoris vary from 20 Myr to 1 Gyr (*e.g.* Navascues *et al.* 1999). Estimates for the lifetime of dust against loss indicate that the dust *cannot* be primordial like that in

the Orion disks, but must be constantly resupplied. The production and loss methods in the disks and rings are nearly identical, differing only on scales of time and size.

In addition to being cousins dynamically, the rings and debris disks share many observational similarities. Both systems are generally flat ($i \lesssim 10^\circ$), are optically thin, and are illuminated by a well-defined point source. These characteristics mean that solving the forward light scattering problem is 'trivial' – unlike the Orion disks – and the inverse problem can be attacked quite easily. Deeper layers of the onion, of course, are soon visible, as the light scattering problem becomes dependent on particle shape, structure, and composition: properties that are hopeless to recover from the Orion observations. Rings have also been sampled *in situ*, constraining many of their physical parameters.

In this chapter (*viz.* Throop & Esposito (1998)), I describe the observations of Saturn's G ring, a typical dusty ring. I use recent observations of the ring to directly characterize its dust population, and use a numerical, evolutionary model to characterize its population of 'invisible' parent bodies and to constrain the history of the ring. My approach for both light scattering and evolutionary modeling is similar in spirit to that done of the younger, denser disks in Orion.

4.2 Observations and previous analysis

Twice during its 29-year orbital period, the ring plane of Saturn enters a period where it is oriented nearly edge-on to the Earth. In this viewing geometry, the planet's G ring – usually far too faint in the glare of the main rings to be detected from Earth – brightens substantially due to the increased line-of-sight particle abundance. During the 1995–1996 ring plane crossing (RPX) period, the ring plane passed through the exact edge-on orientation to the Earth three times, on 22 May 1995, 10 August 1995, and 11 February 1996, and passed through the Sun's plane on 19 November 1995. Observers using the Hubble Space Telescope (Nicholson *et al.* 1996) during the August and

November events and the W. M. Keck 10 m telescope (de Pater *et al.* 1996) during the May and August events were successful in detecting the G ring from Earth – an observation that was considered unlikely only recently (Showalter & Cuzzi 1993). Observations of the G ring during four orbits using the HST Wide Field/Planetary Camera (WFPC2) yielded a spectrum from 0.3 – 0.89 μm at 5 wavelengths, while Keck imaged the ring at 2.26 μm. Observations of the ring were also made by observers at the Infrared Telescope Facility (Bauer *et al.* 1997) at 2.2 μm during the August event, and by observers using the Hubble Space Telescope (French *et al.* 1997) in October 1996, several months after the RPX events. This set of observations represents the first new data from the G ring in nearly 15 years, and the first spectrally resolved observations of the ring. In this chapter, I interpret the reflectance of the ring as being from a size distribution of small ice particles, develop a light scattering model for these particles, and find several classes of particle size distributions – some derived from physical models of the ring – that can explain the observed spectrum. My models are constrained by observations (Table 4.1) of the spectrum, the Voyager phase curve (Showalter & Cuzzi 1993), the RMS particle mass (Tsintikidis *et al.* 1994), and the charged-particle absorption signature of the ring Hood (1989) as well as relevant laboratory light-scattering and impact experiments.

The G ring was first detected in 1979 by absorption of 100 MeV charged particles measured by Pioneer 11 as the spacecraft flew near the ring; initially, the absorption signature was ascribed to the satellite Janus. Voyager 1 detected the ring visually in 1980 and returned one clear image of the ring; in 1981 Voyager 2 returned one additional image. Showalter & Cuzzi (1993) later showed that Voyager 2 flew through the outer edge of the ring, and data from the plasma wave antennas at this crossing have subsequently been associated with direct ring particle impacts with the spacecraft (Aubier *et al.* 1983, Gurnett *et al.* 1983 Tsintikidis *et al.* 1994).

The recent observations differ from those of Voyager in that the recent ones are nearly in backscatter (scattering angle $\theta_{\rm Aug} = 176.4°$; $\theta_{\rm Nov} = 174.5°$; $\theta_{\rm May} = 174.4°$)

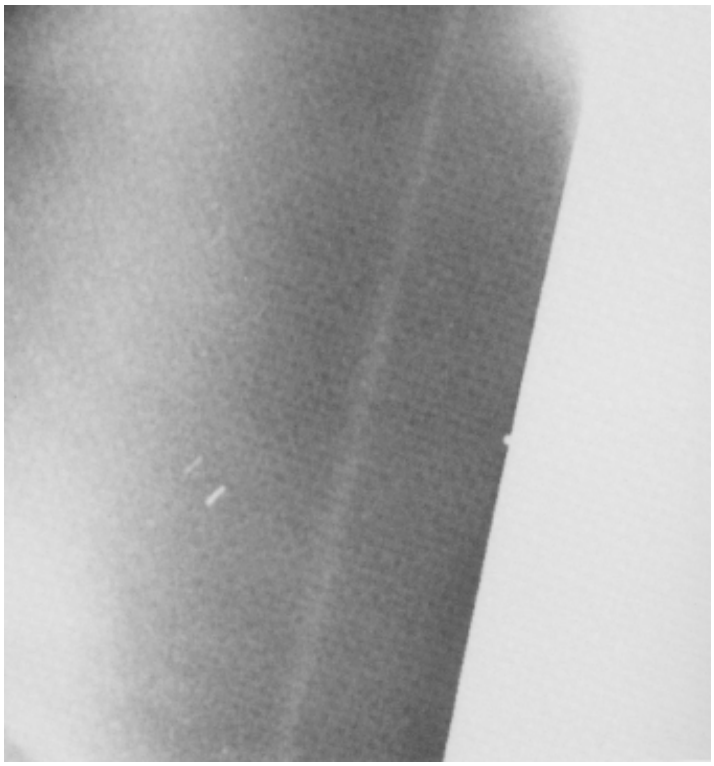

Figure 4.1: G ring at $\theta \sim 30°$, Voyager 2 image FDS 44007.50. The narrow G ring is bounded by the wide E ring and overexposed A/F rings.

Table 4.1: Summary of G ring observations

Date	Instrument	Constraint	References
1979	Pioneer 11 proton absorption	Parent body cross section $10 - 40$ km^2	Hood 1989
1980-81	Voyager 1 & 2 V-band photometry, phase curve	Optical depth dominated by sub-μm particles	Showalter & Cuzzi 1993
1981	Voyager 2 *in situ* sampling	$\langle r \rangle = 1 - 15$ μm	Meyer-Vernet *et al.* 1997, Tsintikidis *et al.* 1994
1995-96	HST, Keck, IRTF, CFHT 0.3-2.26 μm spectra	Dust particle size distribution and evolution	Throop & Esposito 1998, French *et al.* 1997, Nicholson *et al.* 1996, de pater *et al.* 1996, Bauer *et al.* 1996

at five wavelengths (broad filters at $\lambda = 300$, 450, 555, 675 nm, and narrowband methane at 890 nm), while the Voyager images are mostly in forward scatter, $\theta = 30$–$60°$, through one broad-band visual filter centered at $\lambda = 500$ nm. Showalter & Cuzzi (1993) detected faint signatures of the ring in eleven Voyager images in addition to two clearly visible images. The former images were subject to substantial processing, including frame co-addition and a polynomial background subtraction. The wide, diffuse E ring partially obscured the August edge-on G ring images; these images were processed to remove the contribution from the E ring.

Observations by French *et al.* (1997) consisted of a single HST image at $\lambda = 400$ μm and scattering angle $\theta = 178.1°$. This observation was significantly later than the RPX events and thus had a comparably large 3.8° ring opening angle, allowing for a measurement of the radial profile.

The first in-depth analysis of Voyager G ring photometry (Showalter & Cuzzi 1993, hereafter SC93) described it as a dusty "ghost" ring of V-band optical depth $\tau \sim 10^{-6}$, lying at an orbital radius a between 166,000 and 173,000 km (2.72 – 2.85 R_S), beyond the bright B and A rings and just inside the E ring. SC93 compared G ring observations at four scattering angles to phase functions predicted for several ring particle size distributions using Mie theory. They found the observations to be consistent with the phase function of contaminated ice particles in the range $r = 0.03$–40 μm, with

a size distribution described by a power law

$$n(r)dr = r^{-q_{\rm dust}}\,dr \tag{4.1}$$

with an unusually high exponent $q_{\rm dust} \simeq 6$ (a "steep distribution"). With this distribution, the majority of the ring's cross-section is in small particles, which have extremely short lifetimes against drag forces in the ring; SC93 calculated a lifetime of 8–800 years for 1 μm particles. Because of the statistical unlikelihood of observing such a short-lived ring, SC93 proposed the ring to be sustained by a small number of "parent bodies" of $r \sim 1$ km, similar to models proposed for the Uranus and Neptune rings (*e.g.*, Esposito & Colwell 1989, Colwell & Esposito 1990). In the parent body model, large bodies sustain the ring by providing a dust source to balance the loss by various processes. Reanalysis of the Pioneer absorption data (Hood 1989) has been interpreted to indicate a parent body geometric cross-section of 10–40 km^2 in a narrow band $\Delta a \sim 1000$ km across. SC93 proposed that these parent bodies were the remnants of a catastrophically fragmented Saturnian satellite. The km-sized parent bodies have a total optical depth $\tau_{\rm par} \sim 10^{-8}$ and are too small to be directly visible in any current images.

Canup & Esposito (1997, hereafter CE97) developed a physical model of the G ring that describes the evolution of the ring particle size distribution from the breakup of a Saturnian satellite, until loss and production of free dust particles in the ring approached steady-state. They constrained their model to match the SC93 normal optical depth and the Hood (1989) parent body cross section. A third constraint – which SC93 did not have at the time of their study – was the root-mean-square particle mass $m_{\rm rms}$ from Tsintikidis *et al.* 's (1994) reanalysis of the Voyager 2 *in situ* particle sampling detected by the plasma wave spectrometer and planetary radio astronomy instruments (PWS/PRA). Tsintikidis *et al.* (1994) found $m_{\rm rms} \sim 1.8 \times 10^{-8\pm1}$ g, or $r_{\rm rms} \sim 16$ μm, for particles larger than the PWS/PRA detection limit of $\sim 5.4 \times 10^{-9}$

g. With these three constraints, CE97 predicted the slope of the G ring dust to be $2.5 < q_{\rm dust} < 4.5$ for the smallest particles, and were unable to match the observations with $q_{\rm dust} \sim 6$ found by SC93.

The CE97 model matched the bulk optical depth of the ring, but did not attempt to match spectral or phase observations of the ring. Their light scattering calculations considered only the physical cross section of particles and did not use Mie or other more accurate scattering methods. The current work expands on that of CE97 by considering the complete set of G ring observations, including new spectral and phase observations, and by using a more complete light scattering model.

4.3 G Ring Model

In this paper, I adopt the CE97 G ring physical model. This model considers particles in the size range $r = 0.03$ μm – 10 km. The distribution is stored in two state vectors divided into discrete size bins, one vector which includes only particles in the free state (*i.e.*, single particles which contribute to ring optical depth and are not accreted to parent bodies), and one which includes both particles in the free state and those contained in parent body regoliths. The ring is assumed to be both radially and azimuthally homogeneous. At each time step, the number of particles added to the system, lost from the system, and moving between bins is calculated, and the state vectors updated. The simulation ends when a near-steady-state free particle distribution has been achieved, typically in $\lesssim 10^5$ years; at this point, loss and production of dust are nearly equalized. The subsequent lifetime of the parent bodies against catastrophic fragmentation is $\sim 10^8$ years, significantly shorter than the $\sim 10^{11}$ year timescale against steady meteoroid erosion (SC93).

The processes considered by the CE97 model are *i*) dust *production* into the free state by meteoroid flux into parent body regoliths and mutual collisions between parent bodies, and *ii*) dust *loss* from the free state by parent body sweep-up, destructive

Table 4.2: G ring evolutionary model parameter space

Parameter	Range	Description
$q_{\rm ej}$	2.5–7.0	Power law index, regolith ejecta
$m_{\rm largest}$	Unprocessed: $N > m_{\rm largest} \equiv 1$ Processed: $m_{\rm largest} = 0.1 - 10\, m_{\rm impactor}$	Upper size cutoff, regolith ejecta
Flux model	High	Model of Colwell & Esposito (1990); $10^2\times$ higher than Low model
Surface yield	High ('Unbonded quartz sand')	Model of Greenberg *et al.* 1978; $13\times$ higher than Low model
$t_{\rm drag}(1\ \mu{\rm m})$	10-100 yr	Ring crossing time, plasma drag
$f_{\rm l}$	0.12	Mass fraction of largest body, initial disruption event
$r_{\rm trans}$	3–200 μm	Mie-Isotropic scattering transition size
Parent belt radial width	100 km	
Parent belt total cross section	40 km^2	

meteoroid impacts, and plasma and Poynting-Robertson drag forces. Three-body accretion criteria in the Roche zone (Canup & Esposito 1996) are used to calculate the size distribution of the parent bodies; typical distributions are 5–15 bodies of 0.1–1 km. A description of the CE97 model parameters that I consider in this study is presented in Table 4.2; I refer the reader to CE97 for a complete description of their model.

Both my work and that of CE97 consider only the processes occurring in the core ($\Delta a \sim 1000$ km) of the ring. After small particles are removed outward from the core they continue to drift outward but do not interact with the parent bodies. However, the ring profile is observed to be broadly symmetric inward and outward from the central core (SC93), suggesting that dust particles on eccentric orbits dominate the radial profile. Therefore, I assume that the entire brightness of the ring is due to particles currently interacting with the central core, and do not consider those swept out of the core. In a future work I will consider the complete radial profile of the ring.

4.3.1 Dust Production Processes

Mass yields from meteoroid impacts into parent bodies are calculated using the meteoroid flux models described in Colwell & Esposito (1990) and the surface yield parameterizations of Greenberg *et al.* (1978). I make one significant change to the

CE97 model in calculating the size range of regolith ejecta from micrometeoroid impacts. Their model assumes that the ejecta from each micrometeoroid impact is distributed in a power law of slope $q_{\rm ej}$, with lower size cutoff $r_{\rm min} = 0.03$ μm. The upper size cutoff is set such that exactly one particle exists larger than the largest size in their distribution, *i.e.*,

$$N_{\rm r\,>\,r_{max}} \equiv 1 \quad . \tag{4.2}$$

The $n(r)$ ejecta distribution from each impact is then determined by setting the total mass ejected

$$m_{\rm ej} = 1/2\ m_{\rm imp}\ v_{\rm imp}^2\ k_{\rm ej}, \tag{4.3}$$

where I use the ejection yield constant $k_{\rm ej}$ for unbonded quartz sand of Greenberg *et al.* (1978).

This model for upper particle size (an "unprocessed regolith") is based on consideration of initial fragmentation events for impacts into solid bodies (*e.g.*, Lissauter & Safronov 1991), and neglects the likely evolution of the regolith size distribution. Ejecta sizes from an evolved regolith should be smaller due to the fact that sustained meteoroid bombardment only decreases regolith particle sizes. I use as an alternate model (a "processed regolith") the upper size cutoff

$$r_{\rm max} \equiv f \cdot r_{\rm impactor}; \quad f = 0.1\ ...\ 10 \tag{4.4}$$

with the same power law distribution. For shallow size distributions, this size cutoff is significantly smaller than that of the unprocessed model: for $q_{\rm ej} = 2.5$, a 100 μm impactor, and the low extreme of (4.4), I calculate $r_{\rm max} = 2800$ μm and 10 μm for the unprocessed and processed models, respectively. For $q_{\rm ej} = 5.5$, the corresponding values are $r_{\rm max} = 48$ μm and 10 μm.

In both models, the lower end of the size distribution is set at $r_{\rm min} = 0.03$ μm. Such small particles are inefficient scatterers and my results are not strongly sensitive to the lower cutoff size.

My description of dust production due to meteoroid impacts is not entirely self-consistent because the production model does not depend on regolith history. Dust production and loss due to sweep-up by parent bodies of free particles and subsequent release by mutual parent body collisions is handled self-consistently.

4.3.2 Dust Loss Processes

A ring particle can be considered to be in a Keplerian orbit slightly modified by various drag forces. The main loss process is plasma drag due to direct and distant collisions with co-rotating particles in the Saturnian magnetosphere. Poynting-Robertson drag can be calculated to be roughly two orders of magnitude slower than plasma drag (Burns *et al.* 1979), and I ignore it. I also ignore the effects of radiation pressure, shown by Burns *et al.* (1984) to pump micron-sized particles to a maximum eccentricity $\epsilon \sim 0.1$, equivalent to roughly the radial width of the G ring and thus not an important loss process.

SC93 calculated that the particle density of the G ring is high enough such that Debye shielding prevents particles from charging significantly; *i.e.*, the Debye length exceeds the average interparticle distance. Because charges on typical ring particles are small or zero (*e.g.*, Turner *et al.* 2000), SC93 found that the Lorentz force is unimportant in the G ring. Although the size distributions I use in this work have interparticle spacings up to two orders of magnitude higher than those of SC93, the particles are still in the Debye shielded regime, and therefore I do not consider the effects of the Lorentz force.

The co-rotating plasma at the G ring sweeps past Keplerian particles at $v_{\rm rel} \sim$ 15 km s^{-1}, transferring angular momentum to them and sweeping them outward from

the ring. The time for a dust particle of mass m to migrate from the inner to the outer ring edge is

$$t_{\rm cross} = \frac{F_D}{m\ \Delta v_k}, \tag{4.5}$$

where F_D is the total drag force on the particle and Δv_k is the difference in Keplerian velocities at the inner and outer edges of the ring. The total drag force F_D is the sum of drag forces $F_{\rm direct}$ from collisions between ions and dust particles, and $F_{\rm distant}$ from distant "Coulomb collisions." I use the plasma parameters of Richardson (1995) and Bridge *et al.* (1982) modeled from the Voyager encounters: $n_{\rm ion} = 100 \pm 50$ cm^{-3}; $E_{\rm ion}$ = 10 eV; $m_{\rm ion} = 16$ amu. Using Eq. (41) of Gruen *et al.* (1984) and Eq. (9) of Northrop & Birmingham (1990) I calculate the ratio

$$\xi(1\ \mu{\rm m}) \equiv F_{\rm distant}/F_{\rm direct}\ \sim\ 2\ , \tag{4.6}$$

and the ring crossing time

$$t_{\rm cross}(r) = \frac{r}{1\ \mu{\rm m}} 10 \pm 5\ {\rm yr}\ . \tag{4.7}$$

The effect of distant collisions in the G ring has been miscalculated in the past. Northrop & Birmingham (1990) point out that the equations for distant collisions used by Grün *et al.* (1984) – and subsequently Burns *et al.* (1984) and SC93 – assume a 1-D, not 3-D, Maxwellian distribution, and significantly overestimate the effect of distant collisions. This causes the value of ξ calculated to be somewhat lower than the $\xi = 100$ calculated by Grün *et al.* (1984). Using $\xi = 2$, I use Eq. (19) of Morfill *et al.* (1983) to confirm a short ring crossing time. I am unable to reproduce the upper end of the $t_{\rm cross}(1\ \mu{\rm m}) = 8 - 800$ yr crossing time calculated by SC93 based on Burns *et al.* (1984); the error in calculating ξ is in the opposite direction to explain this result.

All of the drag times I consider are defined as ring-crossing times for $\Delta a = 7000$

km. Note that the drag times used in the CE97 paper are defined as the time to cross only the central 1000 km.

The steady-state size distributions of CE97 are multi-component power-law distributions (Figure 4.2, upper curve). The size distribution of the smallest ice particles ($r \lesssim 10\ \mu$m) is shallowed by plasma drag and is well-described by the power-law exponent (Burns *et al.* 1984)

$$q_{\rm dust} = q_{\rm ej} - 1\ . \tag{4.8}$$

For larger r, $q_{\rm dust}$ steepens (Figure 4.2, lower curve) from this value due to *i*) direct grain destruction by meteoroid impact, and *ii*) dust sweep-up by parent bodies. In dust size regimes where the latter is the dominant loss process,

$$q_{\rm dust} = q_{\rm ej}\ . \tag{4.9}$$

Due to the competing effect of direct grain destruction, however, the region where (4.9) applies is typically quite narrow. For larger particles, q is determined by not by on-going processes but by the energy of the initial fragmentation event.

4.4 Light Scattering Model

In somewhat the same way that the Earth's blue skies and red sunsets are caused by light scattering by small particles, the color of light scattered by particles in dusty rings is indicative less of their intrinsic color than the particle size. In this paper, I use both the color and angular-dependence of the observations to constrain the size distribution in the G ring.

For sunlight scattered by the rings, the observable quantity is the ring intensity I, normalized by solar flux F at Saturn as

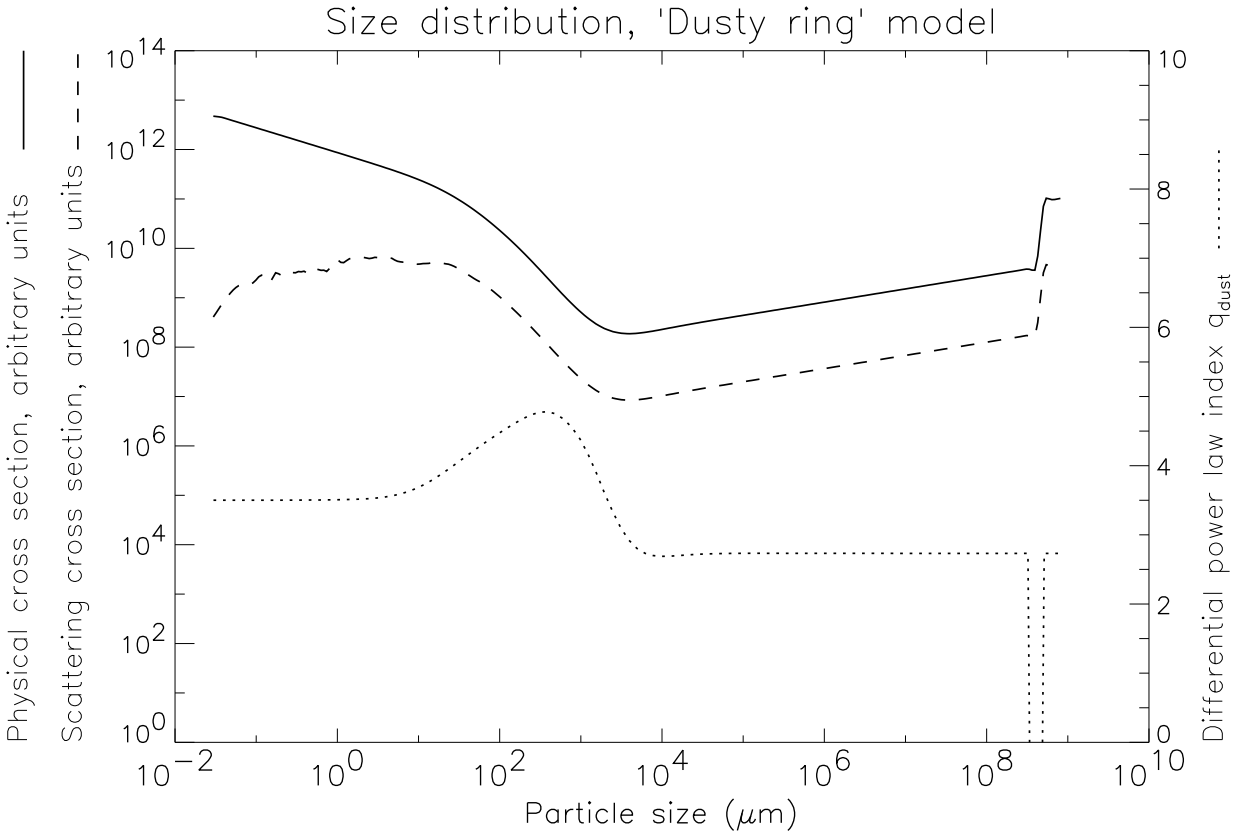

Figure 4.2: Typical G ring particle size distribution from Canup & Esposito (1997) model. The top curve is the incremental cross section per size bin, and the bottom curve the power law size index calculated between adjacent bins. The smallest particles ($r \lesssim 10$ μm) have a slope $q_{dust} = q_{ej} - 1$, and the slope of the largest bodies ($r \gtrsim 1$ cm) is determined by the initial fragmentation event. The parent body lower size cutoff, $r \sim 0.5$ km, is determined by three-body accretion criteria in the Roche zone. The middle curve is the incremental scattering cross section, i.e., the physical cross section multiplied by the scattering efficiency and phase function near at $\theta = 175°$, averaged over wavelength. The smallest particles dominate in the physical cross section but scatter inefficiently; thus, in this case, scattering is dominated by particles in the 1–10 μm range, even though the physical cross section is dominated by sub-micron particles.

$$\frac{I}{F}(\theta,\lambda) = \frac{\tau\ \varpi_0(\lambda)\ P(\theta,\lambda)}{4\ \mu} \tag{4.10}$$

(*e.g.*, Showalter *et al.* 1987), where τ is the normal optical depth, $\varpi_0(\lambda)$ is the single scattering albedo, $P(\theta,\lambda)$ is the normalized scattering phase function for the size distribution, $\mu \equiv \sin(\beta)$, and β is the tilt of the ring plane from edge-on as seen from Earth. For a rectangular G ring cross-section with ring width Δa and vertical height Δz, the edge-on optical depth is

$$\tau_{\rm edge} = \tau_{\rm normal}\ \frac{\Delta a}{\Delta z} \sim 10^{-6}\ \cdot\ \frac{7000\ {\rm km}}{100\ {\rm km}} \sim 10^{-4}\ , \tag{4.11}$$

which is sufficiently low for single scattering to be an accurate approximation.

I define the radially integrated equivalent width

$$EW(\lambda) \equiv \int_a \frac{I}{F}(\theta,a,\lambda)\ da \tag{4.12}$$

which, assuming a radially homogeneous ring, can be written as

$$EW(\lambda) = \frac{1}{4\ \mu}\int_r Q_{\rm sca}(r,\lambda)\ P(\theta,r,\lambda)\ n(r)\ \pi r^2\ \frac{\Delta a}{A} dr, \tag{4.13}$$

where $A = 2\pi a\ \Delta a$ is the area of the ring. Given $n(r)$, finding the equivalent width reduces to finding functions $Q_{\rm sca}(x)$ and $P(x)$, where I define the size parameter

$$x \equiv 2\pi r/\lambda \tag{4.14}$$

and scattering efficiency

$$Q_{sca}(x) \equiv \frac{A_{sca}}{A_{geom}}\ , \tag{4.15}$$

where A_{sca} and A_{geom} are the cross-sectional area for scattering light and the geometric cross-section of the particle. The phase function $P(\theta)$ gives the relative intensity of light as a function of scattering angle θ from the incident beam, and is normalized such that

$$\int_0^\pi P(\theta) \sin\theta \; d\theta = 2 \; . \tag{4.16}$$

Functions P and $Q_{\rm sca}$ are dependent on the size, shape, and other physical properties of the scatterers. I consider the behavior of P and $Q_{\rm sca}$ in three size regimes corresponding to small, medium, and large particles, and the transitions between these regimes. The regime boundaries are determined by the physical properties of the particles, as described below.

4.4.1 Small particle scattering model

Mie theory (*e.g.*, Bohren & Huffman 1983) gives the scattering properties of spherical, homogeneous particles of arbitrary size x and complex index of refraction $n = n_r + n_i i$, where n_r is the real index of refraction and n_i is the imaginary, absorptive component. From x and n, Mie theory calculates the phase function $P(\theta)$ and the scattering coefficient $Q_{\rm sca}$. In the very small particle limit ($x \lesssim 1$), Mie scattering reproduces roughly isotropic Rayleigh scattering; for large particles ($x \gtrsim 100$), Mie scattering approaches the geometric optics ("ray tracing") limit, dominated by forward scatter.

The RPX observations of the G ring are within 5° of backscatter. Laboratory and theoretical work near backscatter has identified several effects that are not present at higher scattering angles, including mutual shadowing (*e.g.*, Buratti & Veverka 1983 coherent backscatter (*e.g.*, Mishchenko & Dlugach 1992, Muinonen 1994) caused by phase interference between equal-length paths, and "glory" (*e.g.*, Khare & Nussenzveig 1977) due to resonant waves in spherical particles. The effect of each of these is to increase $P(\theta)$ near backscatter. Mutual shadowing between particles is only important in an optically thick medium, while coherent backscatter from ring particles has only been seen extremely close to backscatter ($\theta \gtrsim 179°$, Mishchenko & Dlugach 1992), and I do not treat it further.

The glory, however, can cause a strong backscatter peak and is likely to be present

at the sizes of particles in the rings. The glory is most evident as a narrow peak for $x \gtrsim 200$ and $n \gtrsim \sqrt{2}$. A smaller, wider peak appears near backscatter for somewhat smaller particles, $x \sim$ 10–100. Both peaks depend strongly on particle shape and index of refraction. Studies of the glory have indicated that it may be gone or substantially reduced for non-spherical or rough particles (Khare & Nussenzveig 1977), and I therefore look for an appropriate method to treat non-spherical particles in backscatter.

Pollack & Cuzzi (1980) developed a widely-used semiempirical model for the phase function of nonspherical particles, based on simple physical principles and parameterization of laboratory scattering results. For small particles ($x \lesssim 5$) they used Mie theory, while for larger particles ($x \sim$ 5–20), they constructed phase functions of components from transmitted, diffracted, and surface-reflected light. Laboratory work allowed them to parameterize the shape and relative contribution of each component; because their study focused on aerosols, they did not consider particles larger than $x \sim 20$. Laboratory experiments that they considered (*e.g.*, Zerull & Geise 1974, Holland & Gagne 1970) showed monotonically *decreasing* $P(\theta)$ toward backscatter, and their model thus included no backscatter peak. However, the particular experiments used did not measure any closer to backscatter than $\theta \sim 170°$, and the model's linear extrapolation to larger angles may have missed any very real backscatter peak.

Liou *et al.* (1983) used a combination of ray tracing and Fraunhofer diffraction to calculate the phase function for large ($x \sim 1000$) cubes and bricks. They observed a very strong, wide backscatter peak from rays undergoing between 3 and 5 internal reflections. Much of this backscatter is likely to be due to the trough and corner retroflections of the exact particles used and is likely to be significantly reduced for rough particles (*e.g.*, Muinonen *et al.* 1989).

In their analysis of the Saturn F ring, Showalter *et al.* (1992) used the results of Liou *et al.* (1983) to add a backscatter peak to the Pollack & Cuzzi (1980) model. Because of uncertainties of the applicability of *i*) Liou *et al.* 's results to non-rectangular

particles, and *ii*) their combining of different parts of phase functions for measurements of $x \sim 10$ and $x \sim 1000$ particles, I have not used the Showalter *et al.* (1992) modification of the PC80 model.

The transition-matrix ("T-matrix") method developed by Waterman (1971) is a series solution to Maxwell's equations that is similar to Mie theory, but that can be applied to non-spherical particles. Theoretically, the T-matrix method can be applied to particles of arbitrary shape and size; however, considerable analytic effort is required for new shapes (Draine 1988), and computation time increases quickly with size (x^3). Although the method is not new, its use has become practical only recently due to computational and analytical advances. Mishchenko *et al.* (1996) have recently used it to calculate scattering from ensembles of randomly oriented spheroids, cylinders, and Chebyshev particles. Current calculations are limited to $x \lesssim 70$ for axisymmetric particles, and the method is several orders of magnitude slower than Mie scattering for the size ranges computed here. Comparisons of phase functions calculated from prolate & oblate spheroids have been found to match very closely observed phase functions from highly non-uniform particles such as micron-sized soil particles. I have found phase functions from T-matrix calculations for ensembles of randomly oriented spheroidal low-n ($\lesssim \sqrt{2}$) particles to be qualitatively similar to that from Mie scattering, with a somewhat wider, weaker backscatter peak.

Although T-matrix computations would be ideal for my work, the current size limitations prevent me from using it. I have therefore used exclusively Mie scattering for my small particles, and preliminary work with T-matrix calculations for small particles suggests that the effect of this choice is that my computed dust optical depths may be high by a factor of up to two. I do not believe that the difference between spherical and non-spherical particles otherwise significantly affects the scattering calculations; however, computations for large non-spherical particles would be necessary to quantify the difference completely.

I have taken the index of refraction to be that of slightly contaminated amorphous ice, $n = 1.27 + 0.001i$ for visible light, measured by Berland *et al.* (1995), slightly lower than that of crystalline ice ($n = 1.33 + 0.001i$) used by SC93. The difference between these two indices has very little effect, however, nor does varying the imaginary index of refraction in the range $n_i = 10^{-3\pm1}$. The $n_i = 0.001$ assumed corresponds to an exponential absorption depth of $r \sim 20$ μm in the visible. A compilation by Warren (1984) indicates that these optical properties are nearly constant across the visible and at my far wavelength range, $\lambda = 2.26$ μm.

4.4.2 Large particle scattering model

As with previous studies of ring light scattering (*e.g.*, Showalter *et al.* 1992, Estrada & Cuzzi 1996), I assume that the macroscopic particles of the rings have spectra similar to that of contaminated water ice. I use the spectrum $\varpi_0(\lambda)$ of Saturn's main rings from Clark (1980) normalized to a V-band albedo of 0.7 (*e.g.*, Esposito *et al.* 1984), typical of relatively fresh, uncontaminated surfaces. This spectrum is slightly red in the visible and drops off in the IR. The phase function $P(\theta)$ observed by Voyager of Europa was determined by Buratti & Veverka (1983) to be very nearly that of a Lambert sphere; I assume Lambertian scatterers.

For simplicity I do not include the diffraction peak from large particles because the peak is not typically observed; *i.e.*, I assume $Q_{\rm sca} = 1$. Therefore, when I call a particle "backscattering", I refer only to the non-diffracted component.

I note that although the contribution to EW from parent bodies is small, the contribution from other macroscopic particles can be significant. This is a substantial difference between the current model and that of SC93.

4.4.3 Intermediate particle scattering model

As Showalter *et al.* (1992) notes, the phase functions for the large and small particle limits are fundamentally different: Mie theory used for small particles shows forward scatter, with their phase functions *decreasing* monotonically with scattering angle, while the Lambert scattering model for large, opaque bodies is dominated by backscatter, with phase functions *increasing* with scattering angle (*e.g.*, Figure 4.9). Previous photometric models (*e.g.*, Showalter *et al.* 1992, Showalter 1996) that included reflectance from both large and small particles have transitioned between these two regimes with a step function placed at a cutoff value between 20 and 100 μm. In the size distributions considered in those studies, there was very little optical depth at the transition size, so the ring reflectance was insensitive to the specific parameters of the transition. However, review of some laboratory work suggests that a more detailed scattering model in this region may be necessary.

While clear, spherical, crystalline ice can be treated by Mie theory, studies by McGuire & Hapke (1995) of particles with high internal scattering indicate that Mie theory may not be applicable for such particles. This is consistent with everyday observations: a large clear sphere of ice transmits light by forward scatter and can be described by geometric optics; however, a snowball of the same size is nearly opaque and strongly backscatters. McGuire & Hapke (1995) studied internal scattering by introducing 0.3 μm TiO_2 particles into cm-sized smooth, clear resin spheres they constructed in the lab. Spheres with varying amounts of internal scattering were fabricated, and the phase function of each measured. The amount of internal scattering was specified by non-dimensional parameter sD, with internal scattering coefficient s (cm^{-1}) and particle diameter D. For $sD = 0$, they observed Mie scattering in the geometric optics limit; $sD = 35$ yielded approximately isotropic scattering, and at $sD = 275$ the spheres scattered as Lambert surfaces. These results have been subsequently confirmed

by Monte Carlo simulations by Mishchenko & Macke (1997), with the additional result that voids can be treated in the same fashion as the high-n inclusions of McGuire & Hapke.

Internal scattering such as that observed by McGuire & Hapke (1995) is likely to be present in amorphous ice. A microporous, amorphous form of water ice is formed by slow condensation at temperatures below 120 K; between 120 K and 160 K, a denser, optically clear form of amorphous ice is formed, and above 160K crystalline ice is formed (*e.g.*, Brown *et al.* 1996). Amorphous ice will eventually undergo a one-way transition to crystalline ice: for T $>$ 160 K, the transition is nearly immediate, while for T $<$ 77 K, the transition time is roughly the age of the solar system (Schmitt *et al.* 1989). Studies of protosolar nebula formation by Mekler & Podolak (1994) have indicated that present-day small icy bodies formed of uncontaminated H_2O beyond 7.5 AU are likely to have never crystallized, and are good candidates for microporous amorphous ice. The crystalline and amorphous phases of ice can be distinguished by spectral features near 3 and 45 μm (*e.g.*, Moore & Hudson 1992); however, no data for the G ring exists at these wavelengths.

Based on the modeling of Mekler & Podolak (1994), I have assumed that the ring particles are made of microporous amorphous water ice, and I assume that the internal voids in this ice can be treated as internal scatterers. I estimate the function $sD(x)$ for ring particles, and use an appropriate phase function for each size regime as McGuire & Hapke (1995) identified.

Experimental studies by Schmitt *et al.* (1987) of amorphous water ice indicate that the transition to isotropic scattering ("the transition size") occurs in the several-μm range for visible light. This study used thin vapor-deposited ice films, and observed the backscatter from the films while increasing their depth. Detailed behavior of the transition is still largely uncharacterized; for instance, Schmidt *et al.* (1987) looked only at unprocessed, uncontaminated films of ice, and not the roughly spherical particles

present in the rings.

The transition size can also be calculated using the known characteristics of the internal scatterers. Adsorption studies of N_2 into amorphous ice by Mayer & Pletzer (1986) measure an internal scattering area of up to 400 m^2g^{-1}, and find that most of this surface area is in molecular-sized holes of radius $a \sim 20$ Å. Using the criteria of McGuire & Hapke for isotropic scattering, and treating the voids as individual Rayleigh scatterers, I calculate that the amorphous ice examined by Mayer & Pletzer should reach isotropic scattering at $r_{\rm trans} \sim 300$ μm; for $a \sim 50$ Å, isotropic scattering is reached at $r_{\rm trans} \sim 5$ μm. Thus, although large uncertainties exist in the laboratory work, two independent methods leads me to believe that internal scattering is important in this size regime.

In addition to internal scattering, scattering from roughened particle surfaces may also be important. Johnson *et al.* (1985) note that several studies (Brown *et al.* 1978; W. D. Smythe 1984 unpublished) of clear, smooth ice surfaces bombarded by fast (0.1–10 MeV) ions rapidly became highly reflecting. Electron microscope examination by Johnson *et al.* (1985) of the sputtered surfaces revealed them to be dominated by micron-sized pits, changing the surfaces' forward-scattering to highly non-Lambertian backscattering. Johnson *et al.* (1985) have indicated that the particle environment near the G ring is sufficient for sputtering to be an important process; they note that this process could explain, for instance, the non-Lambertian scattering strongly enhanced toward backscatter of Enceladus, which is slightly outside the G ring's orbit at 4 R_S. Further studies by Strazzulla *et al.* (1988) were performed by irradiating 10 K water ice films with 150 keV He^+ ions. They observed that the phase function became more isotropic after irradiation; however, detailed characterization of the phase functions have yet to be made.

I address both internal- and surface- scattering effects by leaving as a parameter $r_{\rm trans}$, defined as the size at which particles scatter isotropically. Thus, the phase

Table 4.3: Scattering transition sizes

$r \leq r_{trans}/7$	Mie scattering
$r_{trans}/7 < r < r_{trans}$	Linear combination: Mie and Isotropic phase curve and spectrum
$r_{trans} < r < r_{trans} \cdot 7$	Linear combination: Isotropic and Lambert phase curve and spectrum
$r \geq r_{trans} \cdot 7$	Lambert scattering

function is a function of particle size (Table 4.3; Figure 4.3), with the transitions between the three scattering regimes chosen to correspond to those measured by McGuire & Hapke (1995). Table 4.3 shows how the single parameter $r_{\rm trans}$ sub-divides the size distribution and the phase functions used for each size. I vary $r_{\rm trans}$ in the range 1 – 300 μm. Because the scattering efficiency of internal scatterers is wavelength-dependent, I vary $r_{\rm trans}$ linearly with λ; *e.g.*, I assume the transition size at $\lambda = 1$ μm to be double that at $\lambda = 0.5$ μm. All transition sizes in this paper are given for $\lambda = 0.5$ μm.

The ring brightness at each wavelength is the sum of the Mie, isotropic, and Lambert reflectances. The latter two components have a fixed color and phase function, while that of the Mie component depends on the particle size distribution.

4.4.4 Spectrum from small particles

The intensity scattered at a fixed θ from small particles is proportional to $P(x)\ Q_{\rm sca}(x)$ (*e.g.*, (4.13)). For spherical particles at $\theta \sim 175^\circ$ observed at the RPX events, this product is a peaked function which reaches a maximum in the range $x \sim$ 10–50 (Figure 4.4): below this size, the scattering efficiency decreases, and above it, forward scatter dominates the Mie phase function. Light scattered at this angle is dominated by particles in this range; both significantly larger and smaller particles are "invisible" to an observer at backscatter. Thus, in much the same way that kernel functions (*e.g.*, Goody & Yung 1989) may be used to probe atmospheric vertical structure at a particular temperature, each part of the reflectance spectrum probes abundance near a particular particle size.

If $q_{\rm dust}$ is such that the cross section in logarithmically spaced bins of r decreases with r (*i.e.*, $q_{\rm dust} > 3$, and the cross-section is dominated by *small* particles), *blue*

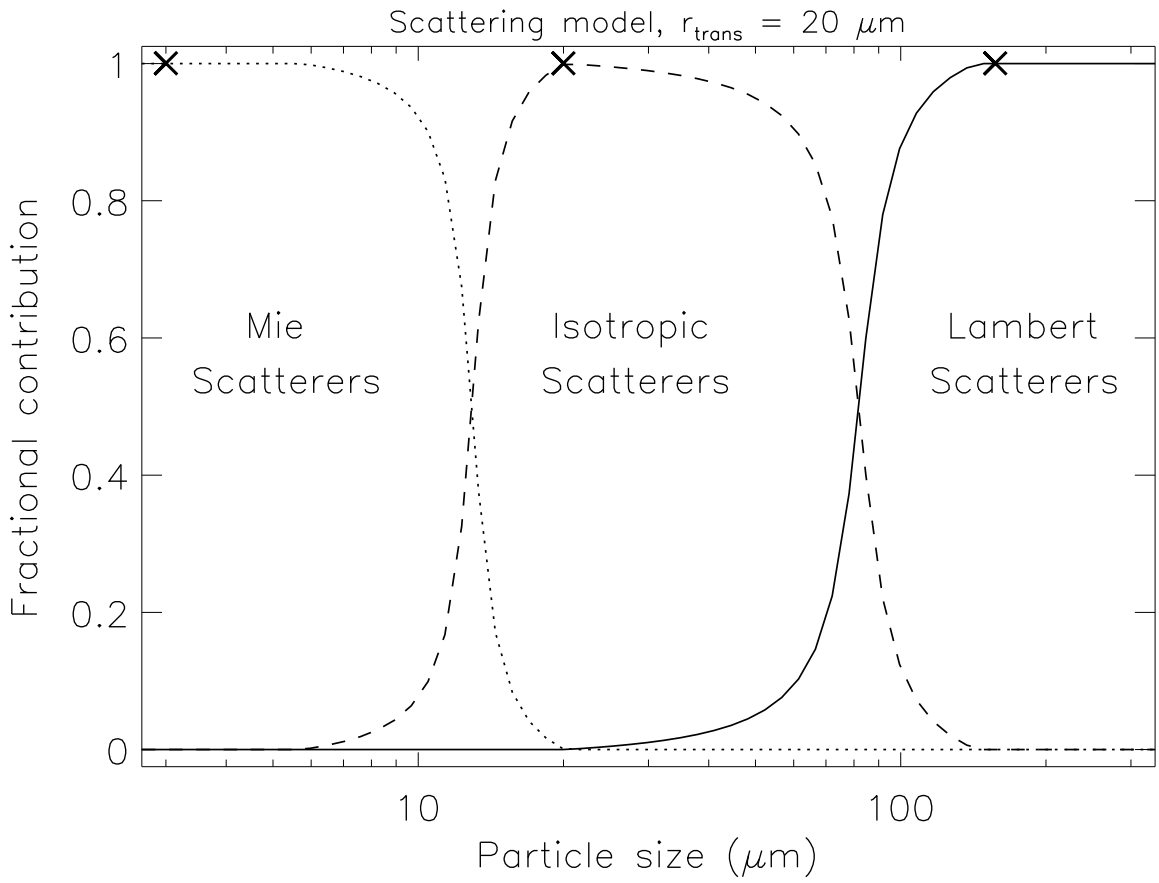

Figure 4.3: The transition sizes for the three-component scattering model. The smallest particles are treated as Mie scatterers, intermediate particles as isotropic scatterers, and the largest as Lambert scatterers. The transitions sizes, marked with symbols, are as identified by McGuire & Hapke (1995). Particles near region boundaries are treated as a combination of scattering types. Mie theory determines the spectrum of the small particles, while I use the spectrum of Saturn's main rings for intermediate and large particles. The transition between the regimes is caused by internal scattering due to voids in amorphous water ice, as described in the text. This figure assumes an internal scattering coefficient $D = 0.9\ \mu\text{m}^{-1}$; this is a parameter that I vary by varying r_{trans} in the range 1–300 μm.

wavelengths will be most visible in the reflected spectrum (Figure 4.5). If, on the other hand, the bulk of the surface area is in *large* particles (*i.e.*, $q_{\rm dust} < 3$) which are more strongly reflecting and thus seen best at longer wavelengths, the scattered light will appear *reddened*. Thus, the back-scattered spectrum from a power law distribution of scatterers can be directly related to the slope of the distribution. This differs from the result of Showalter *et al.* (1991), which showed no strong relation between the two. For generalized (*i.e.*, non power-law) size distributions, the inverse problem is non-unique: multiple size distributions can be consistent with the same spectrum.

The color of the Earth's sky and sunsets is caused by Rayleigh scattering by smaller particles than I consider here (in effect, the monotonic left half of Figure 4.4), and does not correspond in the same way to size distribution.

4.5 Model Results

I have constructed a grid of models, which vary the model parameters $q_{\rm ej}$, $m_{\rm l}$, $t_{\rm drag}$, and $r_{\rm trans}$ across their estimated ranges, as indicated in Table 4.2. For each of the $N \sim 800$ models, I have qualitatively assessed the goodness-of-fit to *i*) the spectrum from HST and Keck, *ii*) the phase curve from Voyager and HST, and *iii*) the $m_{\rm rms}$ derived from the plasma instruments. I find that $q_{\rm ej}$ in the range 2.5–4.5, with appropriate selection of the other parameters, can produce models that are reasonably consistent with the observations (Figures 4.6–4.9). Characteristic fits from the physical models are summarized in Table 4.4.

For the low $q_{\rm ej}$ solutions (*e.g.*, $q_{\rm ej} = 2.5$, "Rocky ring 1", Table 4.4a) the spectrum and phase curve match the observations well. This model, and several others, overestimates $m_{\rm rms}$ by a factor of up to 30; I discuss possible explanations for this difference below.

The "unprocessed regolith" model is inconsistent with a low $q_{\rm ej}$ because this regolith model implies a large maximum ejecta particle size. The total cross section of

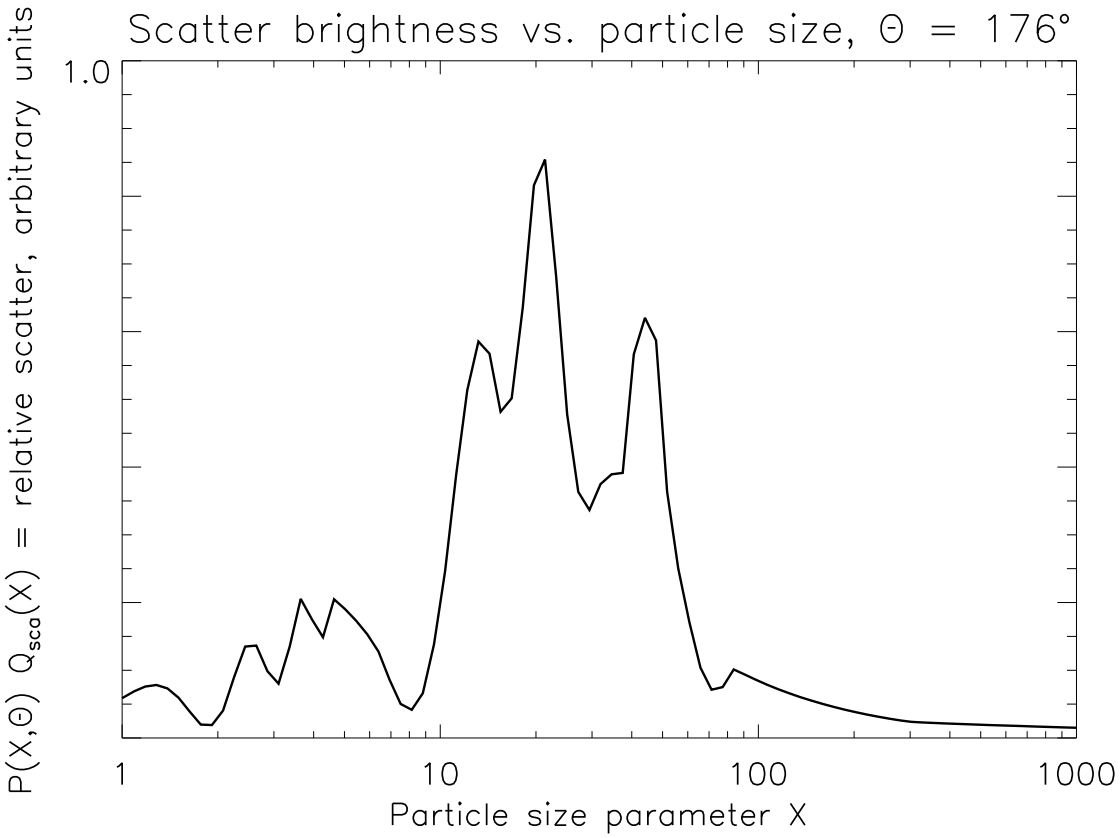

Figure 4.4: a) In Mie scattering, each wavelength scatters strongly only for a narrow range of particle size; for water ice at $\theta \sim 175°$, this size range is $x \sim 40-100$. Below this range Q_{sca} decreases quickly and above this range, the phase function P is dominated by forward scatter. Individual wavelengths in the scattered spectrum can be directly related to a particular particle sizes, and – were the ring to consist of a power-law size distribution of Mie scatterers – the size distribution slope could be directly related to the ring's color. This figure is calculated for the backscatter angle seen during the ring crossing; however, similar size-selection features are seen over a wide range of scattering angles. For reasonably physical size distributions, width will smear out the detail shown here and the function is single-peaked.

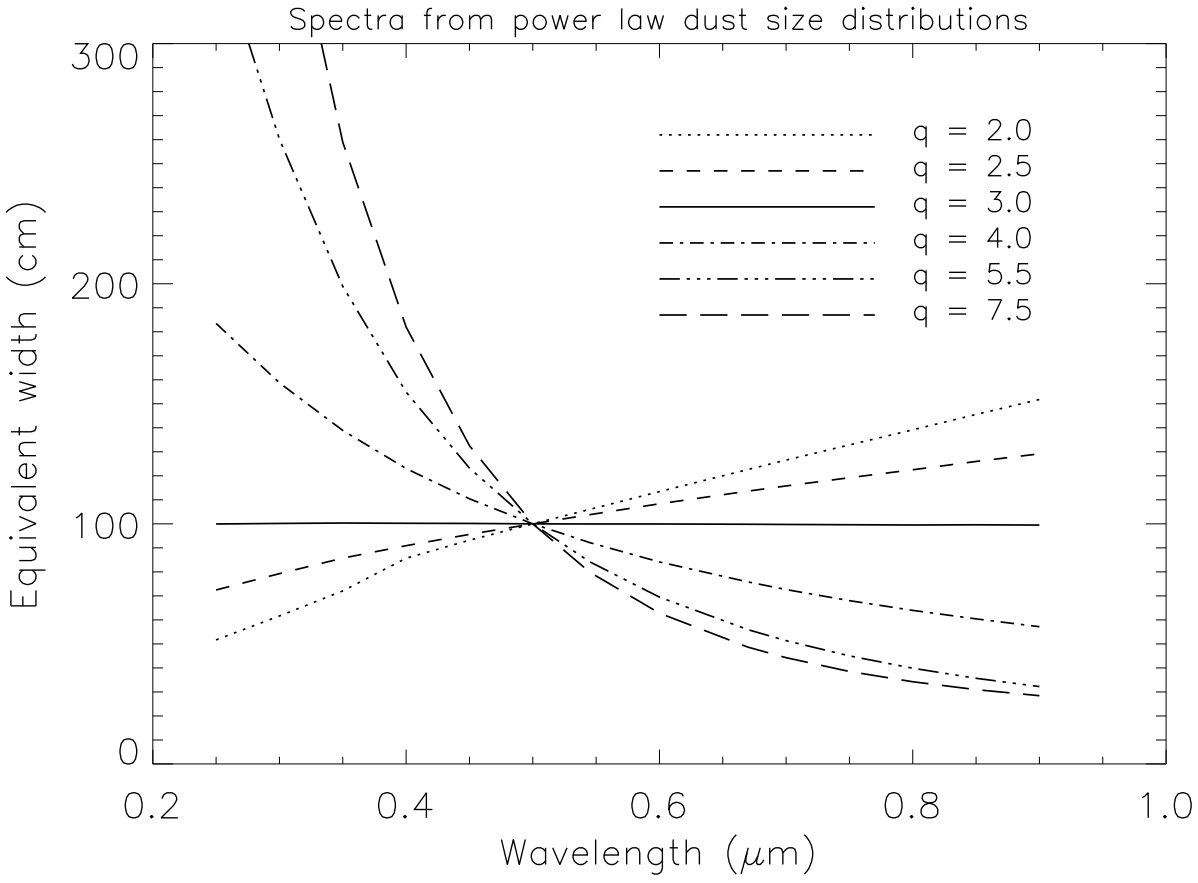

Figure 4.5: The power law slope of a distribution of Mie scatterers is directly related to its reflected color. Distributions dominated in cross-section by large particles ($q_{dust} < 3$) scatter long-wavelength light most efficiently and appear red; distributions dominated by small particles ($q_{dust} > 3$) appear blue. All curves are for $r = 0.01 - 10$ μm, $n = 1.27{+}0.001i$, and are normalized at 0.5 μm.

Table 4.4: Best fits to observations

Name	$q_{\rm ej}$	$m_{\rm largest}$	$t_{\rm drag}(1\ \mu{\rm m})$	$r_{\rm trans}(1\ \mu{\rm m})$	$m_{\rm rms}$(model) / $m_{\rm rms}$(Voyager)[a]
a. Selected evolutionary models					
Rocky ring 1	2.5	0.1 $m_{\rm impactor}$	500 yr	60	27
Rocky ring 2	2.5	0.1 $m_{\rm impactor}$	700 yr	20	27
Dusty ring 1	4.5	0.1 $m_{\rm impactor}$	500 yr	3	28
b. Nonevolutionary models					
		Size distribution			
Gaussian		$r_0 = 13\ \mu{\rm m}, \sigma = 0.5$		15	0.9
$\delta-$functionring		$r = \{8.2\ \mu{\rm m}, 21\ \mu{\rm m}, 100{\rm m}\}$		15	2.3
SC93		$q_{\rm dust} = 6$		-	0.0

[a] Considers only mass above detector threshold; see text.

these large particles is thus significant; because large Lambert scatterers are observed to be dark in the IR, the spectrum of this ring model is too IR-dark to match the observations. However, smaller Mie scatterers do reflect efficiently at this wavelength. Therefore, an IR-bright ring implies a cross section dominated by small particles, such as that from the "processed regolith" model, rather than large particles, such as that from the "unprocessed regolith" model.

A second solution for low $q_{\rm ej}$ ("Rocky ring 2") fits the Voyager phase curve well, but over-estimates the visible spectrum. The size distributions of the two "Rocky ring" models are similar; the primary difference is the value of $r_{\rm trans}$, taken to be 60 μm and 20 μm in the two models, respectively. In the latter model, the smaller transition size means that more small particles are treated as isotropic, rather than Mie, scatterers. The phase curve fits particularly well because the nearly isotropic phase curve from Voyager can be matched well by a population of intermediate-sized isotropic scatterers of $r \sim r_{\rm trans} \sim 20\ \mu$m from my three-component scattering model. In contrast, the scattering model of SC93 included only one type of isotropic scatterer: very small particles in the Rayleigh regime.

In the case of high $q_{\rm ej}$ (*e.g.*, $q_{\rm ej} = 4.5$, "Dusty ring" model), the strong blue scattering from small particles of $r_{\rm trans} < 3$ μm is partly cancelled by the intrinsic red color of the larger particles. This model fits the phase and $m_{\rm rms}$ observations well, but slightly underestimates the IR brightness. Models with $q_{\rm ej} \gtrsim 5$ are too blue to match the HST spectrum; this confirms the initial finding of Nicholson *et al.* (1996) that the size distribution of SC93 is inconsistent with that implied by the broadly red HST spectrum.

The $q_{\rm dust} = 6$ size distribution identified by SC93 fits the phase curve extremely well, but is too strongly blue to match the observed spectrum, even for $r_{\rm trans}$ as low as 0.5 μm. This steep size distribution also predicts no detectable PWS/PRA events. Therefore, I do not consider the SC93 distribution to be consistent with the bulk of the observational data. Although the three solutions shown use the "processed regolith" model, the "unprocessed regolith" model is consistent in some of the high-$q_{\rm ej}$ cases not shown. The difference between the two models is their upper size cutoff; for $q_{\rm ej} > 3$, the optical depth is dominated by small particles and the upper ejecta size cutoff is relatively unimportant.

In addition to size distributions that result from the CE97 evolutionary model, I have identified two "ad hoc" size distributions that fit the observational data (Table 4.4b). The first of these is the quasi-Gaussian of the form specified by Hansen & Travis (1974),

$$n(r) = Cr^{(1/\sigma^2 - 3)} e^{-(r/r_0\sigma^2)} \ , \tag{4.17}$$

with characteristic size $r_0 = 13$ μm and fractional dispersion $\sigma = 0.5$. For this size distribution the visible spectrum and forward scatter components are due primarily to small particles, and the IR and backscatter reflectance are primarily from medium-sized particles.

I also find a multi-component delta-function distribution, with particles at 8 μm

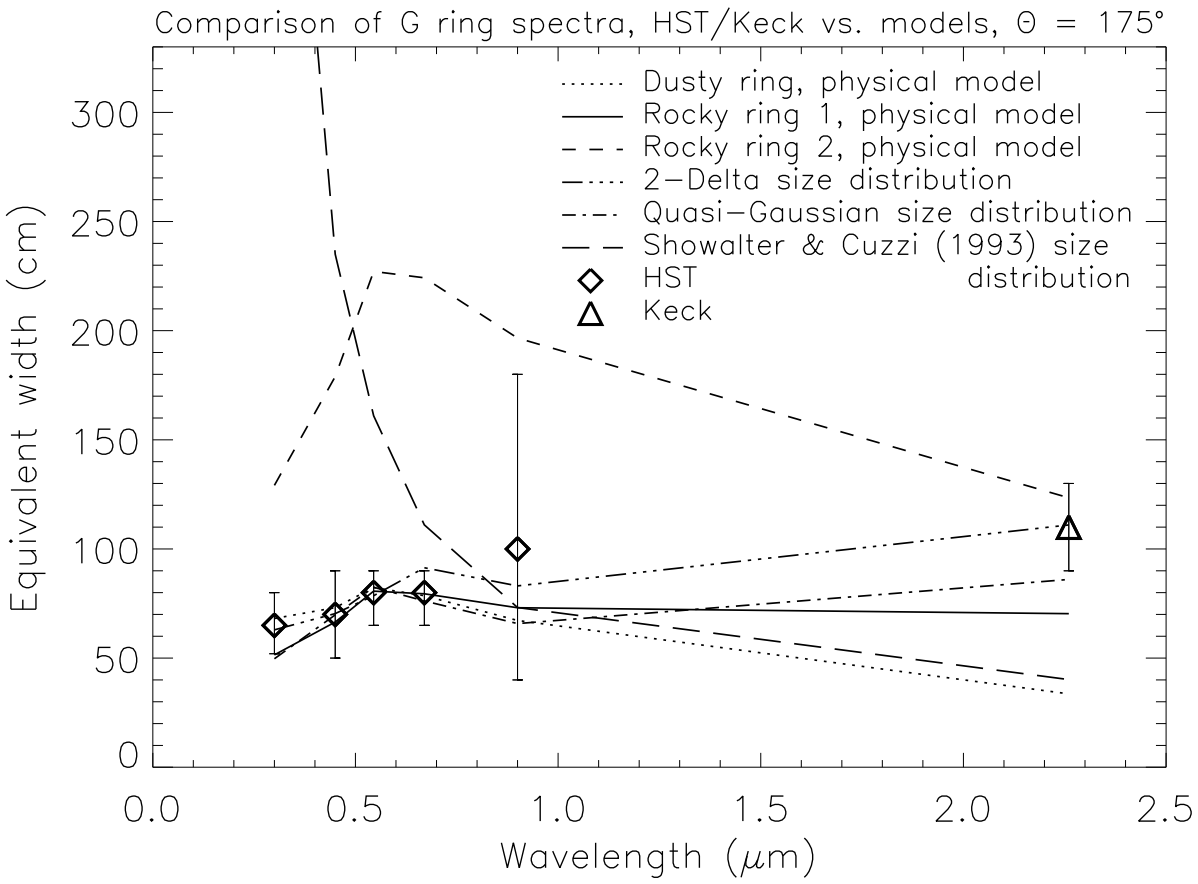

Figure 4.6: I identify several fits to the HST and Keck spectrum. The size distribution of Showalter & Cuzzi (1993) is too blue to fit the spectrum. Other models fit the visible spectrum well, although some underestimate IR brightness. HST data are by Nicholson *et al.* 1996; Keck observation is by de Pater *et al.* (1996).

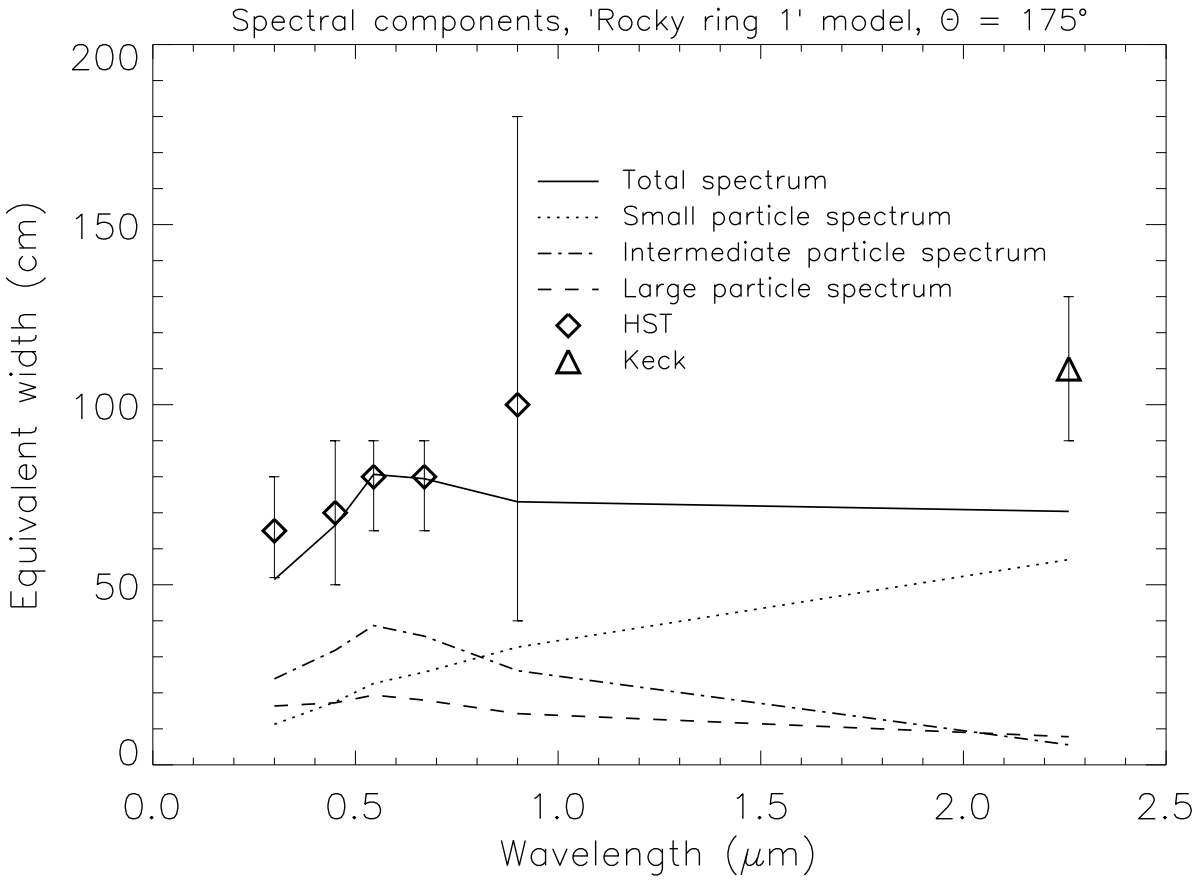

Figure 4.7: Each spectrum is the sum of components from small, intermediate, and large particles. Although the large-particle spectrum is dark in the IR, Mie scattering from small particles is still efficient at the wavelength. Therefore, an IR-bright ring implies the abundance of small particles.

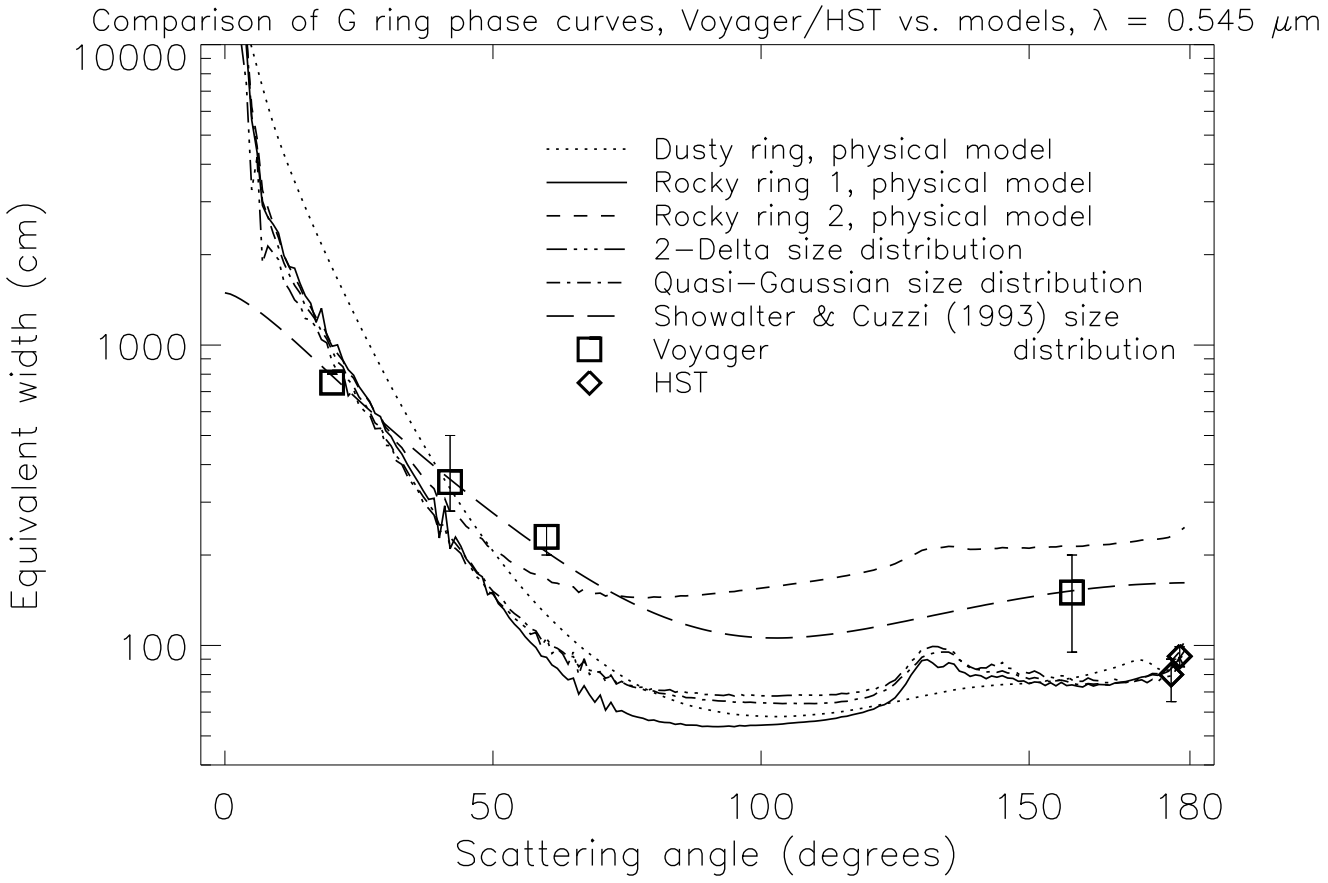

Figure 4.8: Corresponding fits to the Voyager and HST phase curve. The decrease near backscatter ($\theta = 175°$) is not reproduced by standard scattering methods and may be an observational effect or an indication of a change in the ring. Voyager data are by Showalter & Cuzzi (1993); HST data are by Nicholson *et al.* (1996) and French *et al.* (1997)

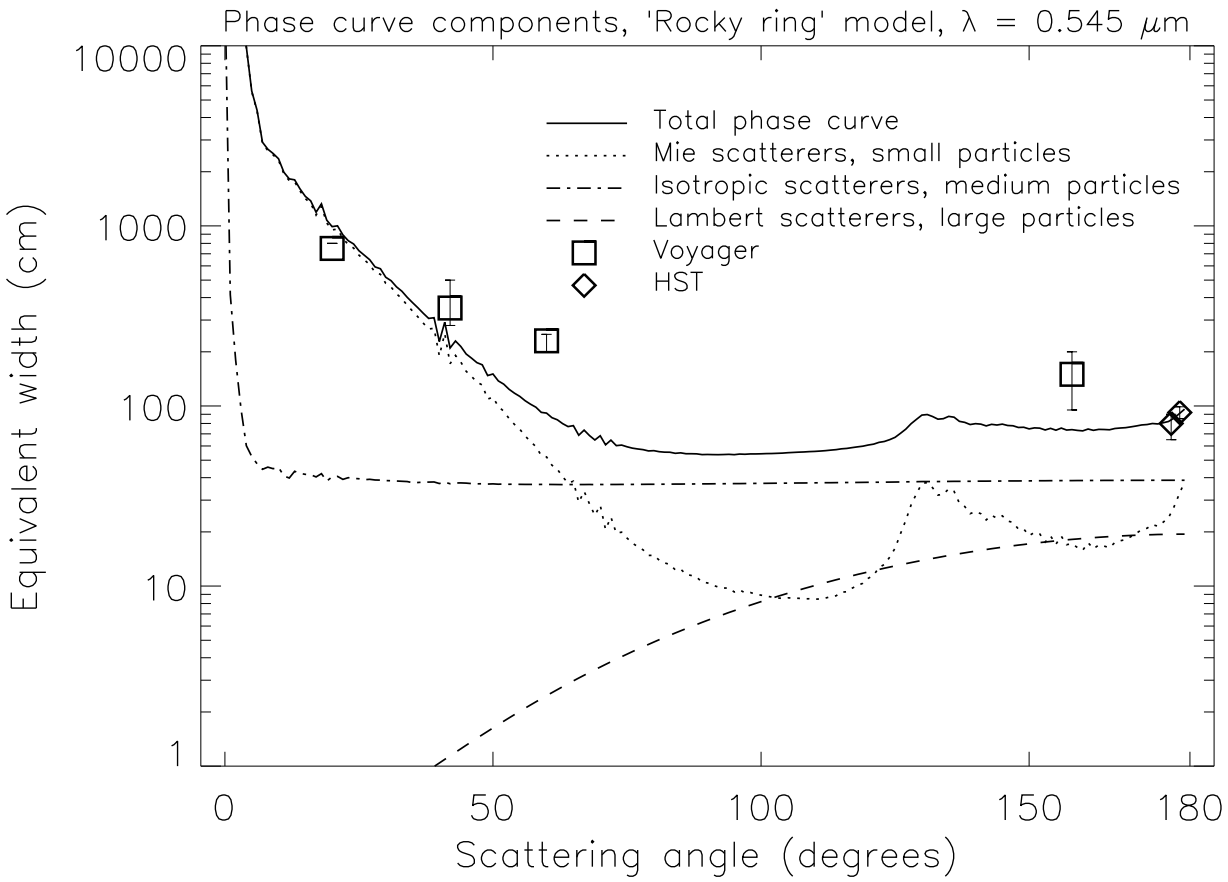

Figure 4.9: The total phase curve from a size distribution is the sum of components from the three scattering types. The phase curve for Mie (forward-scattering) and Lambert (back-scattering) particles are in opposite senses.

and 21 μm, and 100 m parent bodies. This distribution provides an excellent fit to spectral, phase, $m_{\rm rms}$, and proton absorption observations. However, it is not clear what physical processes could create or sustain such a ring. This distribution approximately straddles the quasi-Gaussian distribution above; other similar distributions centered near $r \sim 15$ μm also fit the observations.

These ad hoc distributions are examples of the non-uniqueness of the inversion process. Superpositions of different models are possible; for instance, the quasi-Gaussian distribution may be added to the 'dusty ring' model and fit the observations. Using a physical model significantly constrains the possible solution space; however, it is possible that fits to the observational data exist that I have not considered. I stress, however, that my power-law and ad hoc size distributions fit the observed data regardless of assumptions made in the physical model.

4.6 Discussion

I have found several models that fit the observations well. In this section, I describe the differences between my solutions and the data, and various uncertainties in my model.

Because the Keck data were taken only during the Earth RPX events, the ring appeared edge-on and it was necessary to assume a radial profile in order to calculate the radially-integrated EW. M. R. Showalter (personal communication, 1996) indicates that the G ring radial profile of SC93 was assumed in this analysis. Recent observations of the radial profile by French *et al.* (1997) have confirmed SC93's result, and thus this portion of the Keck data reduction. Some of the HST data were taken during the Sun RPX event when the ring plane did not appear edge-on, and thus do not depend on a radial profile model.

Variations in calibration and processing between the Keck and HST observations may cause additional uncertainties in comparing their absolute values. J. M. Bauer (per-

sonal communication, 1996) indicates that their August 1996 2.2 μm IRTF observations confirm the radially-integrated equivalent width of de Pater *et al.* (1996); Bauer *et al.* (1997) present IRTF results only in terms of vertically-integrated equivalent width.

The individual non-targeted images used for the phase curve presented in SC93 were subject to substantial background subtraction and frame co-addition; without processing, the G ring is only visible in two of the thirteen frames SC93 identify. Although statistical error bars are presented in SC93, care must be used interpreting these data given the extreme conditions under which they were obtained. The HST data were obtained, reduced, and calibrated under consistent and well-characterized conditions; for this reason, when necessary I have chosen to optimize fits to the spectrum rather than the phase curve.

The $m_{\rm rms}$ from many of the models is up to a factor of 30 higher than that computed by Tsintikidis *et al.* (1994) based on reanalysis of the Voyager PWS/PRA data. Several factors must be considered when comparing the two results. The error in measuring the mass of a single particle comes from at least two sources: *i*) uncertainty in the impact ionization yield, unknown to a factor of 10 (Tsintikidis *et al.* 1994), and *ii*) instrumental uncertainties such as antenna potential and spacecraft capacitance. Furthermore, sampling statistics also must be considered due to the low optical depth and number of particle-spacecraft collisions in a typical passage through the ring. Using a Monte Carlo method, I have simulated normal spacecraft trajectories through the ring using a detector with $m_{\rm min} = 5.4 \cdot 10^{-9}$ g threshold estimated for the PWS/PRA instruments, and found that the observed 1σ $m_{\rm rms}$ for individual runs varied by up to a factor ~ 10. Therefore, based on the uncertainties in comparing the Voyager and model results, I have computed average values for $m_{\rm rms}$ based on a large number of passages through the ring, but have not used $m_{\rm rms}$ as a strong constraint to my models. Furthermore, recent modeling of PWS/PRA data by Meyer-Vernet Meyer-Vernet *et al.* (1998) indicates that the *in situ* observations are caused by much smaller particles ($r \sim$

few μm) than indicated by Tsintikidis *et al.* (1994), and of comparable size to those that my photometric modeling indicates.

As discussed earlier, the effect of non-spherical particles may be detectable near backscatter, and may decrease the reflectance by up to a factor of 2 for wavelengths at which the reflectance is from small particles. In most of the solutions, the visible reflectance is due to medium-sized particles, and the IR reflectance due to small particles. Thus, I would expect non-spherical particles to make the ring darker by up to a factor of 2 in IR, and somewhat less changed in the visible. This effect is within the uncertainties of the observations and the particle size distributions.

As indicated by Hamilton & Burns (1994) Saturn's E ring may provide an additional source of particles for the G ring. They showed precession resonances can pump 1 μm particles in the E ring to high eccentricity, where they cross the F and G rings and are ultimately absorbed by the A ring at 2.2 R_S. These particles cross the G ring and I briefly consider their effect as an impactor source into G ring parent bodies.

The E ring number density is observed to fall off inward of its peak at 3.8 R_S as a^{15} (Showalter *et al.* 1991). Assuming the entire optical depth is due to 1 μm particles, calculating a relative impact velocity $v_{impE-G} = 5.5$ km s^{-1}, and using the mass yields for impacts into unbonded quartz sand of Greenberg *et al.* (1978), I find the total mass yield from E ring particles onto G ring parent bodies

$$\dot{M}_{Ering} = n_{imp}\ k_{ej}\ \frac{1}{2}\ m_{imp}\ v^2_{impE-G}\ \simeq\ 4 \text{ g s}^{-1}\ . \tag{4.18}$$

Using the Colwell & Esposito (1990) "high flux" meteoroid model used in CE97, I calculate the mass yield from meteoroid impacts onto parent bodies

$$\dot{M}_{meteoroid} \simeq 3 \text{ g s}^{-1}. \tag{4.19}$$

Thus, although the mass flux of E ring particles significantly exceeds that of

meteoroids, the E ring particles impact into parent bodies at a much lower velocity, and the total yields from each source are surprisingly comparable.

The effect of E ring particles is not incorporated into the CE97 model, and I have not consider this issue further. Better modeling of E ring physical processes, such as particle size distributions produced from the Enceladus surface, is necessary before the effects of its particles on the G can be considered; for instance, the model developed by Hamilton & Burns (1994) generates many more small particles than the photometry by Showalter *et al.* (1991) indicates. Transport between the rings may have interesting consequences: for instance, could the $r = 1$ μm flux from the E ring contribute to an $r = 15$ μm quasi-Gaussian distribution in the G ring?

The solutions presented here are tuned to produce and maintain the maximum ring optical depth; *i.e.*, most of my parameters are set to their extremes to maximize particle production and minimize particle loss. Indeed, it is a bit of a surprise that the ring *is* so bright. At least two explanations are possible. The first is that I have underestimated dust sources or overestimated dust loss. I have addressed this issue by increasing the particle lifetime against plasma drag to longer times than indicated by the Voyager plasma observations. A similar approach would be to increase the cross-section of parent bodies; doubling the cross-section has roughly the same effect as doubling the drag lifetime. Other factors may be important too; for instance, the effect of crossing E ring particles has not been included.

It is surprising that the drag times required by the model are so much longer (by two orders of magnitude) than those indicated by (4.7). This result does not yet have a satisfactory explanation. I note that the main loss process for micron-sized particles at the outer edge is particle sputtering, which is estimated by SC93 to be 10^4 years for $r = 1$ μm particles. The modeling is inconsistent with such a long sputtering time; rather, the nearly radially-symmetric ring profile suggests that the drag and sputtering lifetimes would be comparable.

A second explanation for the apparent difficulty in maintaining a bright ring is that the assumption of a near-steady-state ring may be incorrect. This may relate to an unusual feature of the composite Voyager and HST phase curve: the V-band HST observation may suggest a local *decrease* in brightness toward backscatter, while results from particle scattering models nearly always indicate a local *increase* toward backscatter. This result is somewhat unexpected and – if it is a real effect – could be indicative of a limitation of my optical model or an actual change in the ring between the Voyager and HST observations. In the latter case, it is possible that *i*) the ring is azimuthally non-uniform, and/or *ii*) the ring is time-variable. The first situation is inconsistent with imaging results, which have not suggested any asymmetry. The second case is possible, as variations in the ring's brightness would be expected after every impact event. In the CE97 models, mutual parent body collisions necessary to approximately double the optical depth occur with frequency

$$t_{collision} \sim \frac{1}{\Omega\ \tau_{parent}\ n_{parent}^2} \sim 10^{2-3} \text{ years}, \tag{4.20}$$

for parent body optical depth $\tau_{\rm parent} \sim 10^{-8}$, number of parent bodies $n_{parent} \sim 5 - 15$, and Keplerian orbital speed Ω.

The relaxation time after such a perturbation is model-dependent based on the dominant dust size and thus dominant loss process: for a ring dominated by micron-sized particles, plasma drag is the dominant loss process and

$$t_{relax}(1\ \mu\text{m}) \sim t_{drag}(1\ \mu\text{m}) \sim 10 \text{ yr} . \tag{4.21}$$

For a ring dominated by large particles where parent body sweep-up is the dominant loss process,

$$t_{relax}(1000\ \mu\text{m}) \sim \frac{1}{\Omega\ \tau_{parent}} \sim 10^4 \text{ yr} . \tag{4.22}$$

Thus, it is possible, if statistically unlikely, that the difference between Voyager and HST optical depths in backscatter could be explained by collisional release of small dust particles just prior to the Voyager encounters.

Although several of my parameters – for instance, the particular details of the scattering transition sizes and the ejection model – have high uncertainty, the specific results of my models are relatively insensitive to such details, in the sense that the effects of modifying one parameter can generally be compensated for by changing other parameters. Therefore, I have not attempted to unrealistically constrain unknown parameter values.

4.7 Conclusions

Using a physical, evolutionary model of planetary ring evolution, coupled with a detailed particle scattering model, I have determined a range of size distributions for the Saturn G ring which provide a good fit to the complete set of spacecraft and Earth-based observations. This range is characterized by a differential power law size distribution of exponent $q_{\rm dust} = 1.5$–3.5.

I find that the size distribution indicated by the SC93 analysis of Voyager photometry, $q_{\rm dust} = 6 \pm 1$ is not supported by the observations. My more detailed light scattering model is able to explain the nearly isotropic phase curve presented in SC93 using a size distribution of significantly larger particles; experimental work by McGuire & Hapke (1995) indicates that isotropic scattering is caused both by small Rayleigh scatterers and by much larger internally-scattering particles.

Several ad hoc size distributions also fit the observations; the most physically plausible is a quasi-Gaussian distribution of particles at $r \sim 13$ μm. The inversion process is non-unique and it is possible there are additional distributions have not been identified.

I have used data from an array of observations: HST and Keck visible and IR

spectra, Voyager photometry and phase curves, Voyager dust impact detections, and Pioneer particle absorption signatures. The CE97 physical model used tracks the size distribution of a debris swarm from its initial formation following a satellite disruption into a steady-state ring. My particle scattering model considers several optical phenomena that have not been considered in depth in previous studies of light scattering from planetary rings: namely, the behavior of backscatter peaks caused by realistic non-spherical particles, and the effects of internal and surface scattering on particle phase functions. The scattering model includes contributions from Mie scatterers, isotropic scatterers, and Lambert scatterers, as well as intermediate particles which are a combination of these three scattering types.

This study forms the first complete analysis of the G ring RPX data, and the first analysis of that ring's spectrum. I find that a physically realistic scattering model can be used to explain the observations.

4.7.1 Future work

Observations from the Cassini spacecraft will include IR–UV spectral and phase coverage of the G and other dusty rings. The wider wavelength range of the Cassini instruments may allow observation of scattering from larger particles (in IR) and smaller particles (in UV) than the current observations allow; however, water absorption bands cause the reflectivity of ring particles to drop significantly outside of the wavelength range considered in this paper. Phase coverage of the ring will be important; although my modeling indicates that phase functions are less strongly dependent on particle size distribution than are spectra, the combination of phase information and spectra together is significantly more useful than either one alone. Important measurements will also include *in situ* dust particle detection in the region surrounding the ring, constraint of the parent body cross-section and radial and vertical extent from its effect on the charged particle spatial distribution, and constraint on the meteoroid flux at Saturn.

I use only relatively simple regolith models in this work, while size selection effects and regolith processing history may cause more complex distributions to be more accurate. I note that the non-power-law nature of the meteoritic flux (Gruen *et al.* 1985), grain size effects (*e.g.*, Kendall 1978), and mutual particle grinding (*e.g.*, Austin *et al.* 1986) may all be important in determining the size regolith distribution. More detailed theoretical and laboratory modeling of the regolith evolution process is an open area for future work, in particular because the smallest particles in the rings are both the most visible, and thus the most indicative of ring composition, size distribution, and processing history.

Chapter 5

Conclusions

If you want to make an apple pie from scratch,
you must first create the universe.
C. Sagan, Cosmos

5.1 Will 'Proto' become 'Planetary'?

One recent review paper wrote,

> A demonstration of the growth of dust into large bodies is the one open issue that remains to demonstrate that circumstellar disks – hundreds of examples of which are routinely studied – do spawn planetary systems (Beckwith *et al.* 2000).

In chapters 2 and 3, I present three separate lines of evidence that strongly support the hypothesis that we are observing precisely this growth process in the Orion disks. Specifically,

- The visible disk edges are entirely achromatic, and 3D models for the disks are consistent with scattering by large particles;
- The lack of millimeter-wave thermal emission from the disks is difficult to explain without the existence of large particles; and
- Numerical modeling of disk evolution predicts models like those observed, and these models consistently and rapidly produce large particles.

Will these 'large' ($r \gtrsim 1$ mm) particles continue to grow and eventually form planets? It appears that the rapid photoevaporation of gas may make the formation of

Jupiter-like planets in the Orion region difficult, if these planets form by the standard core-formation and gas accretion model. Earth-like planets, formed closer in and of denser ingredients, are probably just as likely to occur in Orion as elsewhere.

Results of the PAPADUM evolutionary model are robust to the extent that the assumptions and inputs are valid. The least-well characterized process is probably the physics of grain coagulation into 'lint balls': basic parameters such as density, tensile strength, sticking force, and growth efficiency are poorly understood, because collisions of low-velocity, low-strength, low-temperature, low-density bodies in low gravity are simply not seen in everyday life, and difficult to simulate numerically or reproduce in the laboratory. Some micro-gravity experiments currently underway (*e.g.*, Colwell & Taylor (1999); Blum & Wurm (2000)) may soon yield significant insight into this problem, in particular at the small, sub-cm end of the size distribution. Additional uncertainties in the model relate to the initial distribution of material (*e.g.*, $\Sigma(R), T(R)$), although our knowledge should be expected to grow in the future as it has in the past.

5.2 Future Observations

Centimeter interferometry

In the same way that the Paα observations in Chapter 2 allow a longer 'lever arm' to probe large particles in silhouette observations, additional mm- and cm-wavelength measurements of disk opacities would be valuable in extending the observational particle size constraints. Longer wavelengths prove somewhat difficult because of a) lower spatial resolution, and b) increasingly complex thermal emission from the disk, central star, and nebula. It may be possible in some cases to use as a silhouette source not the HII region, but the central star itself. In such a scenario, one would expect a correlation between tilt angle and stellar intensity. Initial calculations suggest that such a detection could likely be made with the A-configuration VLA at $\lambda = 3.6$ cm. The non-detection of the

disks at 1.3 mm continuum makes cm observations extremely compelling.

Polarimetry

Near-IR polarimetric observations have been made with HST of the SW disk by McCaughrean *et al.* (1998), and these data have not yet been analyzed. Polarized emission from aligned grains could be due to grain alignment caused by at least three processes: a) a magnetic field either from external ionization or frozen in during collapse; b) grain entrainment in the outflow; or c) grains settling to the midplane. The HST data should be analyzed as soon as possible. Longer wavelength polarimetric observations are possible with the TNTCAM-2 10-20 μm camera Klebe *et al.* (1998) that has been used to image Orion several times at the 2.3 m WIRO observatory.

Infalling large bodies

Can we directly detect the presence of even larger bodies – km-sized or larger planets or planetesimals – around the Orion disks? It is possible that many of the apparently disk-free stars in Orion have been cleared of their disk and are currently surrounded by swarms of bodies too massive to detect. Direct imaging or radial velocity techniques seem unlikely. However, the existence of planetesimals around β Pic has been inferred from episodic variations in the CI/II lines, attributed to large 'comets' evaporating and falling onto the central star. It is entirely possible that the Orion disks may show similar spectroscopic variability.

Photosputtered atmospheres surrounding large bodies

Photoevaporation by definition ceases after a gas disk has been dispersed. However, solid ices remaining in a disk would be still subject to UV photosputtering and erosion. Are there spectral signatures that could be used to detect the results of photosputtering? OI and OH, for instance, are commonly detected in the atmospheres

of comets, subject to similar processes on our solar system, and it is worth studying whether they would be expected at levels high enough to detect around Orion. Identifying 'invisible' disks producing these species would be a major accomplishment.

Planetary rings

For planetary rings, Cassini will revolutionize (again) our understanding of the particles, processes, and physics of the Saturnian ring system. It is possible that imaging will directly detect the presence of one or more km-sized parent bodies in the rings, confirming the 'dusty ring' model that has been successfully applied to many rings and disks. A non-detection could of course be even more interesting. For determining particle sizes, spectra and phase curves are *both* necessary, because there are significant ambiguities in using either one alone. There remain some vexing issues with the dusty rings, however: a) What is the plasma density, and why do drag timescales calculated require much lower plasma densities than measured by Voyager? b) Does the G ring have significant, unexplained asymmetries between the ansae, as seen in the Galileo ring observations at Jupiter? c) What, if any, is the time-variability of the dusty rings, and can collisions between large parent bodies be directly observed, as has been proposed in the F ring (*e.g.*, Barbara 1999).

5.3 Predictions

I will end with a set of ten 'predictions,' some of which may have already happened and are waiting for detection, and some of which may be ungrounded and never happen at all. They should be interpreted not as results, but as loose hypotheses in the context of exploration and possible directions for future research.

- Earth-like planets form as easily in dark clouds as large OB associations.

- Life is more common on Earth-like planets formed in OB associations because of rapid UV formation of of organics.

- If Jovian-type planets form in the 'traditional' way, they should occur infrequently in OB associations and thus infrequently in the universe. (*i.e.*, Jupiters are made either quickly or rarely.)

- If Jupiter was formed by 'traditional' methods, its existence suggests that our solar system should continue with substantial KBO's and dust out to several hundred AU.

- The volatile content of terrestrial planets formed in OB associations is lower than that in our solar system.

- Our solar system has an anomalously large cometary reservoir and we should not expect an extra-solar cometary visit soon.

- Our own solar system is more likely to have formed in a dark cloud than among massive stars.

- Large, aggregate grains are common in the ISM as a result of failed planetary formation followed by disk photoevaporation.

- Many of the Orion disks have already formed km-sized or larger planetesimals, which can be detected spectrally after the gas disks are lost.

- Stars in OB associations have depleted metallicities because small grains are lost by photoevaporation before they can accrete onto the star: there is a positive correlation between metallicity of a star and the existence of planets around that star.

Bibliography

Aikawa, Y., T. Umebayashi, T. Nakano & S. M. Miyama, 1997. Evolution of molecular abundance in protoplanetary disks. Astrophys. J. **486**, L51–54.

Aubier, M. G., N. Meyer-Vernet & B. M. Pederson, 1983. Shot noise from grains and particle impacts in Saturn's ring plane. Geophys. Res. Let. **10**, 5–8.

Austin, L. G., C. A. Barahona, N. P. Weymont & K. Suryanarayanan, 1986. An improved simulation model for semi-autogenous grinding. Powder Technol. **47**, 265–268.

Bally, J., C. R. O'Dell, M. McCaughrean & R. Sutherland, 1999. Microjets, Wind Bubbles, and Proto-Planetary Disks in the Orion Nebula Cluster. Bull. Amer. Astron. Soc. **31**, 68.12+.

Bally, J., R. S. Sutherland, D. Devine & D. Johnstone, 1998a. Externally illuminated young stellar environments in the Orion nebula: Hubble Space Telescope planetary camera and UV observations. Astron. J. **116**, 293–321.

Bally, J., L. Testi, A. Sargent & J. Carlstrom, 1998b. Disk mass limits and lifetimes of externally illuminated young stellar objects embedded in the orion nebula. Astron. J. **116**, 854–859.

Barbara, J. M., 1999. Moonlet collisions in Saturn's F ring. BA Honors Thesis.

Barlow, M. J., 1978. The destruction and growth of dust grains in interstellar space. II. Destruction by grain surface reactions, grain-grain collisions and photodesorption. Month. Not. Royal Astron. Soc. **183**, 397–415.

Barth, C. A., C. W. Hord, A. I. F. Stewart, W. R. Pryor, K. E. Simmons, W. E. McClintock, J. M. Ajello, K. L. Naviaux & J. J. Aiello, 1997. Galileo ultraviolet spectrometer observations of atomic hydrogen in the atmosphere of Ganymede. Geophys. Res. Let. **24**, 2147–2150.

Bauer, J., J. J. Lissauer & M. Simon, 1997. Edge-on observations of Saturn's E and G rings in the near-IR. Icarus **125**, 440–445.

Beckwith, S. V. W., T. Henning & Y. Nakagawa, 2000. Dust properties and assembly of large particles in protoplanetary disks. In Protostars and Planets IV (eds. V. Mannings, A. P. Boss & S. S. Russell). U. Ariz. in press.

Beckwith, S. V. W. & A. I. Sargent, 1991. Particle emissivity in circumstellar disks. Astrophys. J. **381**, 250–258.

Beckwith, S. V. W., A. I. Sargent, R. S. Chini & R. Guesten, 1990. A survey for circumstellar disks around young stellar objects. Astron. J. **99**, 924–945.

Berland, B. S., D. E. Brown, M. A. Tolbert & S. M. George, 1995. Refractive index and density of vapor-deposited ice. Geophys. Res. Let. **22**, 3493–3496.

Blum, J. & G. Wurm, 2000. Experiments on sticking, restructuring, and fragmentation of preplanetary dust aggregates. Icarus **143**, 138–146.

Bohren, C. F. & D. R. Huffman, 1983. Absortion and Scattering of light by small particles. Wiley.

Boss, A. P., 1997. Giant planet formation by gravitational instability. Science **276**, 1836–1839.

Breger, M., R. D. Gehrz & J. A. Hackwell, 1981. Interstellar grain size. II. Infrared photometry and polarization in Orion. Astrophys. J. **248**, 963–976.

Bridge, H. S., F. Bagenal, J. W. Belcher, A. J. Lazarus, R. L. McNutt, J. D. Sullivan, P. R. Gazis, R. E. Hartle, K. W. Oglivie, J. D. Scidder, E. C. Sittler, A. Eviatar, G. L. Siscoe, C. K. Goertz & V. M. Vasyliunas, 1982. Plasma observations near saturn: Initial results from Voyager 2. Science **215**, 563–570.

Brown, W. L., L. J. Lanzerotti, J. M. Poate & W. M. Augustyniak, 1978. "Sputtering" of ice by MeV light ions. PRL **40**, 1027–1030.

Buratti, B. & J. Veverka, 1983. Voyager photometry of Europa. Icarus **55**, 93–110.

Burns, J. A., P. L. Lamy & S. Soter, 1979. Radiation forces on small particles in the solar system. Icarus **40**, 1–48.

Burns, J. A., M. R. Showalter & G. E. Morfill, 1984. The ethereal rings of Jupiter and Saturn. In Planetary Rings (ed. R. G. . A. Brahic), 200–272. U. Ariz.

Burrows, C. J., K. R. Stapelfeldt, A. M. Watson, J. E. Krist, G. E. Ballester, J. T. Clarke, D. Crisp, J. S. Gallagher, R. E. Griffiths, J. J. Hester, J. G. Hoessel, J. A. Holtzman, J. R. Mould, P. A. Scowen, J. T. Trauger & J. A. Westphal, 1996. Hubble Space Telescope observations of the disk and jet of HH30. Astrophys. J. **473**, 437–451.

Cardelli, J. A., G. C. Clayton & J. S. Mathis, 1989. The relationship between infrared, optical, and ultraviolet extinction. Astrophys. J. **345**, 245–256.

Chen, H., J. Bally, C. R. O'Dell, M. J. McCaughrean & R. L. Thompson, 1998. 2.12 micron molecular hydrogen emission from circumstellar disks embedded in the Orion nebula. Astrophys. J. **492**, L173–176.

Churchwell, E., M. Felli, D. O. S. Wood & M. Massi, 1987. Solar system-sized condensations in the Orion nebula. Astrophys. J. **321**, 516–529.

Clark, R. N., 1980. Ganymede, Europa, Callisto, & Saturn's rings: Compositional analysis from reflectance spectroscopy. Icarus **44**, 388–409.

Cohen, M., 1975. Infrared observations of young stars. IV. A 2- to 4- micron search for molecular features. Month. Not. Royal Astron. Soc. **173**, 279–293.

Cohen, M., 1983. HL Tauri and its circumstellar disk. Astrophys. J. **270**, L69–L71.

Colwell, J. E. & L. W. Esposito, 1990. A numerical model of the uranian dust rings. Icarus **86**, 467–501.

Colwell, J. E. & M. Taylor, 1999. Low-velocity microgravity impact experiments into simulated regolith. Icarus **138**, 241–248.

Cuzzi, J. N., A. R. Dobrovolskis & J. M. Champney, 1993. Particle-gas dynamics in the midplane of a protoplanetary nebula. Icarus **106**, 102–134.

de Pater, I., M. R. Showalter, J. J. Lissauter & J. R. Graham, 1996. Keck infrared observations of Saturn's E and G rings during Earth's 1995 ring plane crossings. Icarus **121**, 195–198.

Draine, B. T., 1988. The discrete-dipole approximation and its application to interstellar graphite grains. Astrophys. J. **333**, 848–872.

Dubrulle, B., G. Morfill & M. Sterzik, 1995. The dust subdisk in the protoplanetary nebula. Icarus **114**, 237–246.

Elmegreen, B. G., 1985. Molecular clouds and star formation: An overview. In Protostars and Planets II (ed. Black, D. C. and M. S. Matthews), 33–58. U. Ariz.

Esposito, L. W. & J. Colwell, 1989. Creation of the uranus rings and dust bands. Nature **339**, 605–607.

Esposito, L. W., J. N. Cuzzi, J. B. Holberg, E. A. Marouf, G. L. Tyer & C. C. Porco, 1984. Saturn's rings – Structure, dynamics, and particle properties. In Planetary Rings (ed. A. B. R. Greenberg), 463–545. U. Ariz.

Estrada, P. R. & J. N. Cuzzi, 1996. Voyager observations of the color of Saturn's rings. Icarus **122**, 251–272.

Farinella, P., D. R. Davis & S. A. Stern, 2000. Formation and collisional evolution of the Edgeworth-Kuiper belt. In Protostars and Planets IV (eds. V. Mannings, A. P. Boss & S. S. Russell). U. Ariz. in press.

French, R. G., J. Cuzzi, L. Dones & J. Lissauer, 1997. High-resolution imaging of Saturn's G ring from the Hubble Space Telescope. Bull. Amer. Astron. Soc. **29**, 1097+.

Galilei, G., 1610. Siderus Nuncius. Padova.

Goody, R. M. & Y. L. Yung, 1989. Atmospheric radiation: Theoretical basis. Oxford, 2nd edition.

Grady, C., D. Devine, B. Woodgate, R. Kimble, F. C. Bruhweiler, A. Boggess, J. J. Linsky, P. Plait, M. Clampin & P. Kalas, 2000. The circumstellar disk of HD 163296: A young planetary system. Bull. Amer. Astron. Soc. **31**, 2.08+.

Greenberg, R., J. F. Wacker, W. K. Hartmann & C. R. Chapman, 1978. Planetesimals to planets: Numerical sumulations of collisional evolution. Icarus **35**, 1–26.

Gruen, E., G. R. Morfill & D. A. Mendis, 1984. Dust-magnetosphere interactions. In Planetary Rings (ed. R. G. . A. Brahic), 275–332. U. Ariz.

Gruen, E., H. A. Zook, H. Fechtig & R. H. Giese, 1985. Collisional balance of the meteoritic complex. Icarus **62**, 244–272.

Gurnett, D. A., E. Gruen, D. Gallagher, W. S. Kurth & F. L. Scarf, 1983. Micron-sized particles detected near Saturn by the Voyager plasma wave instrument. Icarus **53**, 236–254.

Hamilton, D. & J. A. Burns, 1994. Origins of Saturn's E ring: Self-sustained, naturally. Science **264**, 550–553.

Hansen, J. E. & L. D. Travis, 1974. Light scattering in planetary atmospheres. Spac. Sci. Rev **16**, 527–610.

Hawley, J. F., S. A. Balbus & W. F. Winters, 1999. Local hydrodynamic stability of accretion disks. Astrophys. J. **518**, 394–404.

Hayward, T. L. & M. J. McCaughrean, 1997. A search for thermal infrared emission from three silhouette disks in Orion. Astron. J. **113**, 346–353.

Holland, A. C. & G. Gagne, 1970. The scattering of polarized light by polydisperse systems of irregular particles. Appl. Optics **9**, 1113–1121.

Hollenbach, D., D. Johnstone, S. Lizano & F. Shu, 1994. Photoevaporation of disks around massive stars and application to ultracompact HII regions. Astrophys. J. **428**, 654+.

Hood, L. L., 1989. Investigation of the Saturn dust environment from the analysis of energetic charged particle measurements. In Cassini AO, volume 13.

Johnson, R. E., L. A. Barton, J. W. Boring, W. A. Jesser, W. L. Brown & L. J. Lanzerotti, 1985. Charged particle modification of ices in the Saturnian and Jovian systems. In Ices in the Solar System, 301–315. D. Reidel Pub.

Johnstone, D., D. Hollenbach & J. Bally, 1998. Photoevaporation of disks and clumps by nearby massive stars: application to disk destruction in the Orion nebula. Astrophys. J. **499**, 758–776.

Kalas, P. & D. Jewitt, 1995. Asymmetries in the Beta Pictoris Dust Disk. Astron. J. **110**, 794–804.

Kendall, J., 1978. The impossibility of comminuting small particles by compression. Nature **272**, 710–711.

Khare, V. & H. M. Nussenzveig, 1977. Theory of the glory. Phys. Rev. Lett. **38**, 1279–1282.

Klebe, D. I., R. E. Stencel & D. S. Theil, 1998. TNTCAM MARK II: A new mid-IR array imager/polarimeter. Soc. Pro. Inst. Eng. **3354**, 1–21.

Krivov, A. V. & D. P. Hamilton, 1997. Martian dust belts: Waiting for discovery? Icarus **128**, 335–353.

Lada, E. A., 1998. Observations of star formation: the role of embedded clusters. In Origins (eds. C. E. Woodward, J. M. Shull & H. A. Thronson), volume 148, 198–220.

Lecavelier des Etangs, A., A. Vidal-Madjar & R. Ferlet, 1996. Dust distribution in disks supplied by small bodies: is the β Pictoris disk a gigantic multi-cometary tail? Astron. & Astrophys. **307**, 542–550.

Levison, H., L. Dones, M. Duncan & P. Weissman, 1999. The formation of the Oort cloud. Bull. Amer. Astron. Soc. **31**, 6.05+.

Lin, D. N. C. & P. Bodenheimer, 1982. On the evolution of convective accretion disk models of the primordial solar nebula. Astrophys. J. **262**, 768–779.

Lin, D. N. C. & J. Papaloizou, 1980. On the structure and evolution of the primordial solar nebula. Month. Not. Royal Astron. Soc. **191**, 37–48.

Liou, K. N., Q. Cai, J. B. Pollack & J. N. Cuzzi, 1983. Light scattering by randomly oriented cubes and parallelepipeds. Appl. Optics **22**, 3001–3008.

Lissauer, J. J., 1987. Timescales for planetary accretion and the structure of the protoplanetary disc. Icarus **69**, 249–265.

Lissauter, J. J. & V. E. Safronov, 1991. The random component of planetary rotation. Icarus **93**, 288–297.

Mathews, W. G., 1967. Dynamic effects of radiation pressure in HII regions. Astrophys. J. **147**, 965–978.

Mayer, E. & R. Pletzer, 1986. Astrophysical implications of amorphous ice – a microporous solid. Nature **319**, 298–301.

McCaughrean, M. J., H. Chen, J. Bally, E. Erickson, R. Thompson & M. Rieke, 1998. High-resolution near-IR imaging of the Orion 114-426 silhouette disk. Astrophys. J. **492**, L157–L161.

McCaughrean, M. J. & C. R. O'Dell, 1996. Direct imaging of circumstellar disks in the Orion nebula. Astron. J. **111**, 1977–1986.

McGuire, A. F. & B. W. Hapke, 1995. An experimental study of light scattering by large, irregular particles. Icarus **113**, 134–155.

Mekler, Y. & M. Podolak, 1994. Formation of amorphous ice in the protoplanetary nebula. Plan. Spac. Sci. **42**, 865–870.

Meyer-Vernet, N., A. Lecacheux & B. M. Pederson, 1998. Constraints on Saturn's G ring from the Voyager 2 radio astronomy instrument. Icarus **132**, 311–320.

Mishchenko, M. I. & J. M. Dlugach, 1992. Can weak localization of photons explain the opposition effect of Saturn's rings? Month. Not. Royal Astron. Soc. **254**, 15–18.

Mishchenko, M. I. & A. Macke, 1997. Asymmetry parameters of the phase function for isolated and denseley packed spherical particles with multiple internal inclusions in the geometric optics limit. JQSRT **57**, 767–794.

Mishchenko, M. I., L. D. Travis & D. W. Mackowski, 1996. T-matrix computations of light scattering by non-spherical particles: a review. JQSRT **55**, 535–575.

Mizuno, H., W. J. Markiewicz & H. J. Voelk, 1988. Grain growth in turbulent protoplanetary accretion disks. Astron. & Astrophys. **195**, 183+.

Morfill, G. E., E. Gruen & T. V. Johnson, 1983. Saturn's E, G, & F rings: modulated by the plasma sheet? J. Geophys. Res. **88**, 5573–5579.

Muinonen, K., 1994. Coherent backscattering by solar system dust particles. IAU Symp. Asteroids, Comets, Meteors **160**, 271–296.

Muinonen, K., K. Lumme, P. Peltoneimei & W. Irvine, 1989. Light scattering by randomly oriented crystals. Appl. Optics **28**, 3051–3060.

Navascues, D. B., J. R. Stauffer, I. Song & J.-P. Caillault, 1999. The age of β Pictoris. Astrophys. J. **520**, L123–L126.

Nicholson, P. D., M. R. Showalter, L. Dones, R. G. French, S. M. Larson, J. J. Lissauer, C. A. McGhee, P. Seitzer, B. Sicardy & G. E. Danielson, 1996. Observations of Saturn's ring-plane crossings in August and November 1995. Science **272**, 509–515.

Northrop, T. G. & T. J. Birmingham, 1990. Plasma drag on a dist grain due to coulomb collisions. Plan. Spac. Sci. **38**, 319–326.

O'Dell, C. R., Z. Wen & X. Hu, 1993. Discovery of new objects in the Orion nebula on HST images: shocks, compact sources, and protoplanetary disks. Astrophys. J. **410**, 696–700.

O'Dell, C. R. & S. K. Wong, 1996. Hubble Space Telescope mapping of the Orion nebula. I. A survey of stars and compact objects. Astron. J. **111**, 846–855.

Philipp, H. R., 1985. Silicon Dioxide (SiO_2) (Glass). In Handbook of Optical Constants of Solids II, 749–763. Academic Pr.

Pollack, J. B. & J. N. Cuzzi, 1980. Scattering by nonspherical particles of size comparable to a wavelength: A new semi-emprical theory and its application to tropospheric aerosols. J. Atmo. Sci. **37**, 868–881.

Pollack, J. B., D. Hollenbach, S. Beckwith, D. P. Simonelli, T. Roush & W. Fong, 1994. Composition and radiative properties of grains in molecular clouds and accretion disks. Astrophys. J. **421**, 615–639.

Pollack, J. B., O. Hubickyj, P. Bodenheimer, J. J. Lissauer, M. Podolak & Y. Greenzweig, 1996. Formation of the Giant Planets by Concurrent Accretion of Solids and Gas. Icarus **124**, 62–85.

Press, S. H., S. A. Teukolsky, W. T. Vetterling & B. P. Flannery, 1992. Numerical Recipes in C. Cambridge, 2nd edition.

Richardson, J. D., 1995. An extended plasma model for Saturn. Geophys. Res. Let. **22**, 1177–1180.

Ruden, S. P. & J. B. Pollack, 1991. The dynamical evolution of the protosolar nebula. Astrophys. J. **375**, 740–760.

Savage, B. D. & J. S. Mathis, 1979. Observed properties of interstellar dust. Ann. Rev. Astron. Astrophys. **17**, 73–113.

Schmitt, B., S. Espinasse, R. J. A. Grin, J. M. Greenberg & J. Klinger, 1989. Laboratory studies of cometary ice analogues. ESA SP **302**, 65–69.

Schmitt, B., J. Ocampo & J. Klinger, 1987. Structure and evolution of different ice surfaces at low temperature adsorption studies. J. Phys. Suppl. 3 **48**, 519–525.

Showalter, M. R., J. A. Burns, J. N. Cuzzi & J. B. Pollack, 1987. Jupiter's ring system: New results on structure and particle properties. Icarus **69**, 458–498.

Showalter, M. R., J. N. Cuzzi & S. M. Larson, 1991. Structure and particle properties of Saturn's E ring. Icarus **94**, 451–473.

Showalter, M. R., J. B. Pollack, M. E. Ockert, L. R. Doyle & J. B. Dalton, 1992. A photometric study of Saturn's F ring. Icarus **100**, 394–411.

Showstack, R., 1999. Scientists discover solar system 44 AU from Earth. EOS **80**, 193+.

Shu, F., D. Johnstone & D. Hollenbach, 1993. Photoevaporation of the solar nebula and the formation of the giant planets. Icarus **106**, 92+.

Shuping, R. Y., 2000. Carbon monoxide absorption in the interstellar medium. Ph.D. thesis, University of Colorado.

Stapelfeldt, K. R., C. J. Burrows, J. E. Krist, J. T. Trauger, J. J. Hester, J. A. Holtzman, G. E. Ballester, S. Casertano, J. T. Clarke, D. Crisp, R. W. Evans, J. S. Gallagher, R. E. Griffiths, J. H. Hoessel, J. R. Mould, P. A. Scowen, A. M. Watson & J. A. Westphal, 1995. WFPC2 imaging of the circumstellar nebulosity of HL Tauri. Astrophys. J. **449**, 888–893.

Stepinski, T. F. & P. Valageas, 1996. Global evolution of solid matter in turbulent protoplanetary disks. I. Aerodynamics of solid particles. Astron. & Astrophys. **309**, 301–312.

Stepinski, T. F. & P. Valageas, 1997. Global evolution of solid matter in turbulent protoplanetary disks. II. Development of icy planetesimals. Astron. & Astrophys. **319**, 1007–1019.

Stern, S. A. & J. Colwell, 1997. Collisional erosion in the primordial Edgeworth-Kuiper belt and the generation of the 30-50 AU Kuiper belt. Astrophys. J. **492**, 879–882.

Stoerzer, H. & D. Hollenbach, 1998a. Nonequilibrium photodissociation regions with advancing ionization fronts. Astrophys. J. **495**, 853–870.

Stoerzer, H. & D. Hollenbach, 1998b. On the [OI] 6300 line emission from the photoevaporating circumstellar disks in the Orion nebula. Astrophys. J. **502**, L71–74.

Stoerzer, H. & D. Hollenbach, 1999. Photodissociation region models of photoevaporating circumstellar disks and application to the proplyds in Orion. Astrophys. J. **515**, 669–684.

Strazzulla, G., L. Torrisi & G. Foti, 1988. Light scattering from ion-irradiated frozen gases. Europhys. Lett. **7**, 431–434.

Tegler, S. & R. Romanishin, 1999. Kuiper Belt Objects. Bull. Amer. Astron. Soc. **31**, 23.01+.

Throop, H. B. & L. W. Esposito, 1998. G ring particle sizes derived from ring plane crossing observations. Icarus **131**, 152–166.

Tsintikidis, D., D. Gurnett, L. J. Granroth, S. C. Allendorf & W. S. Kurth, 1994. A revised analysis of micron-sized particles detected near Saturn by the Voyager 2 plasma wave instrument. J. Geophys. Res. **99**, 2261–2270.

Turner, N. E., D. N. Baker, T. I. Pulkkinen & R. L. McPherron, 2000. Evaluation of the Tail Current Contribution to Dst. J. Geophys. Res. **105**, 5431–5439.

van de Hulst, H. C., 1980. Multiple Scattering by Small Particles. Dover.

Voelk, H. J., F. C. Jones, G. E. Morfill & S. Roeser, 1980. Collisions between grains in a turbulent gas. Astron. & Astrophys. **85**, 316–325.

Wallis, M. K., 1986. Random fluctuations versus Poynting-Robertson drag on interplanetary dust grains. Nature **320**, 146–148.

Ward, W. R., 1997. Protoplanet migration by nebula tides. Icarus **126**, 261–281.

Warren, S. G., 1984. Optical constants of ice from the ultraviolet to the microwave. Appl. Optics **23**, 1206–1225.

Warren, W. H. & J. E. Hesser, 1977. A photometric study of the Orion OB 1 association. I - Observational data. II - Photometric analysis. ApJS **34**, 115–231.

Waterman, P. C., 1971. Symmetry, unitarity, and geometry in electromagnetic scattering. Phys. Rev. D **3**, 825–839.

Weidenschilling, S. J., 1977. Aerodynamics of solid bodies in the solar nebula. Month. Not. Royal Astron. Soc. **180**, 57–70.

Weidenschilling, S. J., 1980. Dust to planetesimals: settling and coagulation in the solar nebula. Icarus **44**, 172–189.

Weidenschilling, S. J., 1997. The origin of comets in the solar nebula: a unified model. Icarus **127**, 290–306.

Weidenschilling, S. J. & J. N. Cuzzi, 1993. Formation of planetesimals in the solar nebula. In Protostars and Planets III (eds. E. H. Levy & J. I. Lunine), 1031–1060. U. Ariz.

Wen, Z. & C. R. O'Dell, 1995. A three-dimensional model of the Orion nebula. Astrophys. J. **438**, 784–793.

Westley, M. S., R. A. Baragiola, R. E. Johnson & G. A. Baratta, 1995. Photodesorption from low-temperature water ice in interstellar and circumsolar grains. Nature **373**, 405–407.

Yorke, H. W., P. Bodenheimer & G. Laughlin, 1993. The formation of protostellar disks. I. 1 $M_{\odot}$. Astrophys. J. **411**, 274–284.

Zerull, R. H. & R. H. Geise, 1974. Microwave analogue studies. In Planets, Stars, and Nebulae: Studied with Photopolarimetry (ed. T. Gehrels), 901–914. U. Ariz.

Zweibel, T. H., 1998. New solar system discovered four feet from Earth. The Onion **43**, 1–3.